12-2015

STUDY OF SECONDARY PARTICLES PRODUCED FROM HEAVY-ION INTERACTIONS

Pi-En Tsai
University of Tennessee - Knoxville, ptsai4@vols.utk.edu

To the Graduate Council:

I am submitting herewith a dissertation written by Pi-En Tsai entitled "STUDY OF SECONDARY PARTICLES PRODUCED FROM HEAVY-ION INTERACTIONS." I have examined the final electronic copy of this dissertation for form and content and recommend that it be accepted in partial fulfillment of the requirements for the degree of Doctor of Philosophy, with a major in Nuclear Engineering.

Lawrence H. Heilbronn, Major Professor

We have read this dissertation and recommend its acceptance:

Lawrence Townsend, Jason Hayward, Yanwen Zhang

Accepted for the Council:
Carolyn R. Hodges

Vice Provost and Dean of the Graduate School

(Original signatures are on file with official student records.)

STUDY OF SECONDARY PARTICLES PRODUCED FROM HEAVY-ION INTERACTIONS

A Dissertation Presented for the
Doctor of Philosophy
Degree
The University of Tennessee, Knoxville

Pi-En Tsai
December 2015

ACKNOWLEDGEMENTS

I would like to express my sincere gratitude to Dr. Lawrence Heilbronn for being my PhD dissertation advisor. I could not finish the dissertation without his dedication, patience, and hands-on advising on the new measurement techniques as well as the nuclear physics theories. I also appreciate the freedom he gave me to study and develop new research projects that I am interested in. To me, Dr. Heilbronn is not only a dissertation advisor, but more like a mentor in my research career.

In addition to my advisor, I would like to thank my graduate committee members, Dr. Lawrence Townsend, Dr. Jason Hayward, and Dr. Yanwen Zhang, and their insightful and constructive comments on my dissertation and defense. I want to thank Dr. Townsend particularly as he gave me great supports at a fork in my career path.

I also appreciate our collaborators from the National Tsing Hua University, Dr. Rong-Jiun Sheu, Bo-Lun Lai, and Yung-Cheng Hsu. They contributed all the FLUKA and MCNP's model calculations in the dissertation. I met a lot of great people and received their help during my graduate program, and I would like to thank them here: Dr. Lembit Sihver from the Vienna University of Technology, Dr. Tatsuhiko Sato from the Japan Atomic Energy Agency, the staff of HIMAC for their assistance with the setup and running of the experiment, Prof. Shiang-Huei Jiang from the National Tsing Hua University for enlightening me the first glance of research.

Last but not least, I would like to thank my parents, my sisters and brother-in-laws for their unconditional support and encouragement. I also thank my good partner - Yu-Che Hsiao, and my friends - Ting-Ni Lu, Chien-Hung Chen, Yu-Chuan Lin, Ching-Hsuan Wu, Kang-Ju Lee, Shih-Jui Hsu, Jamie Porter, and Dan Zhang.

ABSTRACT

The study of secondary particles produced from heavy-ion interactions is important in heavy ion radiotherapy, space radiation protection, and shielding at accelerator facilities. This dissertation focuses on the study of secondary neutron production as they are of special concern among all secondary particles.

The first part of this dissertation is the measurement of secondary neutrons created from ^{4}He [helium] stopped in various target materials together with the model calculations accomplished by PHITS, FLUKA, and MCNP transport codes. The comparison results show that the physics models need improvements particularly in the predictions of 1) neutrons created from the ^{4}He interactions at the high-energy end of the spectra at each angle for FLUKA's and PHITS's models, 2) the high-energy peaks at 0 degree for all systems and all models, and 3) the low-energy neutrons at small angles for 230-MeV/nucleon [megaelectron volt per nucleon] ^{4}He stopping in the light targets. However, the model calculations agree with the experiment data well at intermediate and large angles in intermediate and low energy regions.

The second part is the benchmark of the neutron production cross section data with model calculations fulfilled by PHITS, FLUKA, and MCNP. The studied cases cover wide ranges of projectile species, beam energy and target nuclei mass. Some significant differences do appear not only among model calculations but also between measured data and calculations. In particular, LAQGSM03.03 implemented in MCNP6 significantly overestimates the high-energy peak in the forward direction in the light and very light system at 400 MeV/nucleon. RQMD implemented in FLUKA 2011.2c overestimates the neutron cross sections at intermediate energies in nearly all systems expect the lightest targets in our studies cases. The greatest inter-model difference appear on low-energy neutrons at forward angles in the system of 400-MeV/nucleon ^{132}Xe (xenon) and copper target,

and it is inferred that GEM implemented in PHITS 2.73 over-predicts neutrons produced from evaporation.

The results of both experimental study and model calculations provide critical information for validation and verification of the current radiation transport codes used for simulating heavy-ion interactions and help lead to improvements in the physics models.

TABLE OF CONTENTS

LIST OF TABLES

LIST OF FIGURES

CHAPTER I
INTRODUCTION

Knowledge of high-energy heavy-ion induced nuclear reactions is critical in diverse fields including heavy ion radiotherapy, space exploration, and shielding at accelerator facilities. In each application involving heavy ions, not only the primary ions but also the secondary particles must be considered. Among all secondary particles, secondary neutrons are of special concern, since neutrons are highly-penetrating neutral particles with large dose conversion factors and large equivalent dose factors. Hence, this study is focused on the production of secondary neutrons created in heavy-ion induced nuclear reactions.

In CHAPTER I, general information regarding the importance of this secondary neutron study in heavy ion therapy and in space radiation protection followed by the original contribution of this dissertation is briefly described. CHAPTER II focuses on the measurement of secondary neutrons produced by ^{4}He ions stopping in various target materials, including the experiment target design, experimental setup, measurement results including the double-differential thick target neutron yields, angular distributions, and total neutron yields, and the comparison between the experimental results and the model calculations by PHITS, FLUKA and MCNP. In CHAPTER III, the inter-comparison of three Monte Carlo simulation codes – PHITS, FLUKA and MCNP with the existing secondary neutron production cross section data are presented. The simulation cases cover the projectiles from ^{12}C ions to ^{132}Xe ions over the energy range from 135 MeV/nucleon to 600 MeV/nucleon, and the target materials include ^{nat}Li, ^{nat}C, ^{nat}Al, ^{nat}Cu, and ^{nat}Pb. The last chapter, CHPATER IV, concludes the dissertation.

I.1 Application in heavy ion radiotherapy

Radiotherapy using ion beams has gained momentum in radiation oncology. While the number of proton therapy facilities under construction or in operation in the United States and worldwide is rapidly growing, clinical facilities using heavy-ion (whose atomic number Z is greater than one) beams for treatment are concentrated in Asia and Europe, especially in Japan and Germany. Though Lawrence Berkeley National Laboratory was the pioneer in heavy ion therapy conducting the first helium ion treatment in 1957 [1], the United States has lost its leadership position in heavy ion radiotherapy. However, the interests in heavy ion radiotherapy has been revitalized in the United States, as reflected in a recent grant award supported by the National Institute of Health (NIH) to establish a heavy ion research centers [2].

Protons and heavy ions are all capable of delivering narrow Bragg peaks and exhibit a small lateral and range scattering in tissue, yet the detailed physical dose distribution is different for different ions. With the increasing atomic mass, both lateral scattering and range straggling decrease such that therapeutic dose can be more precisely delivered. At the same time, however, the probability and number of nuclear reaction channels increase, producing energetic secondary fragments with certain ranges that lead to unwanted doses to health tissue. As a result, an optimum in overall dose distribution lies between helium and oxygen [3]. In addition, it was concluded that desirable future ion beam therapy facilities in the U.S. should be individually capable of delivering treatments with multiple ion species spanning from protons through carbon or oxygen for optimistic treatment, based on the discussions at the “Workshop on Ion Beam Therapy” co-hosted by the U. S. Department of Energy and the National Cancer Institute in 2013. [4]

Helium ions, compared to protons and carbon ions which are more commonly used in clinical studies, have better peak-to-entrance dose ratios than

protons and yet contribute less doses from secondary neutrons and charged fragments than carbon ions [5 - 8]. Considering the risk of late sequelae and radiation-induced tumors, reduction of the dose in healthy tissues contributed by secondary particles produced from nuclear interaction of primary ion beams with human tissue is important for children and adolescents. Therefore, the U.S. hadron therapy community has also expressed interest in using helium ions for radiation treatment. To use helium ions for radiotherapy in the future, it is of critical interest to well characterize the secondary particles produced by primary ion interactions with beam-delivery devices and human tissue.

I.2 Application in space radiation

Helium ions also play an important role in the space environment. The ionizing radiation in space radiation consists of galactic cosmic ray (GCR) and solar energetic particle (SEP). SEP includes about 80-90% protons, 10-20% helium and about 1% heavy ions. About 98% of the GCR comprises protons and heavy ions, with electrons making up the remaining 2%. Among the hadronic GCR, the ion species include 87% protons, 12% helium, and 1% heavy ions with energies ranges from tens of MeV/nucleon to several TeV/nucleon. These GCR ions have a broad fluence peak between 200 to 600 MeV/nucleon, as shown in Figure 1 [9].

Neutrons, as one of the major concerns for space radiation shielding, are created by GCR and SEP interacting with shielding materials or astronauts' bodies in space. Even though helium ions make up only 12% of the hadronic GCR fluence, they can contribute approximately 30% of the secondary neutron fluence, depending on the shielding material and thickness [10]. Hence, the secondary neutrons created by helium ions have to be taken into consideration, especially for future long-term and deep-space missions.

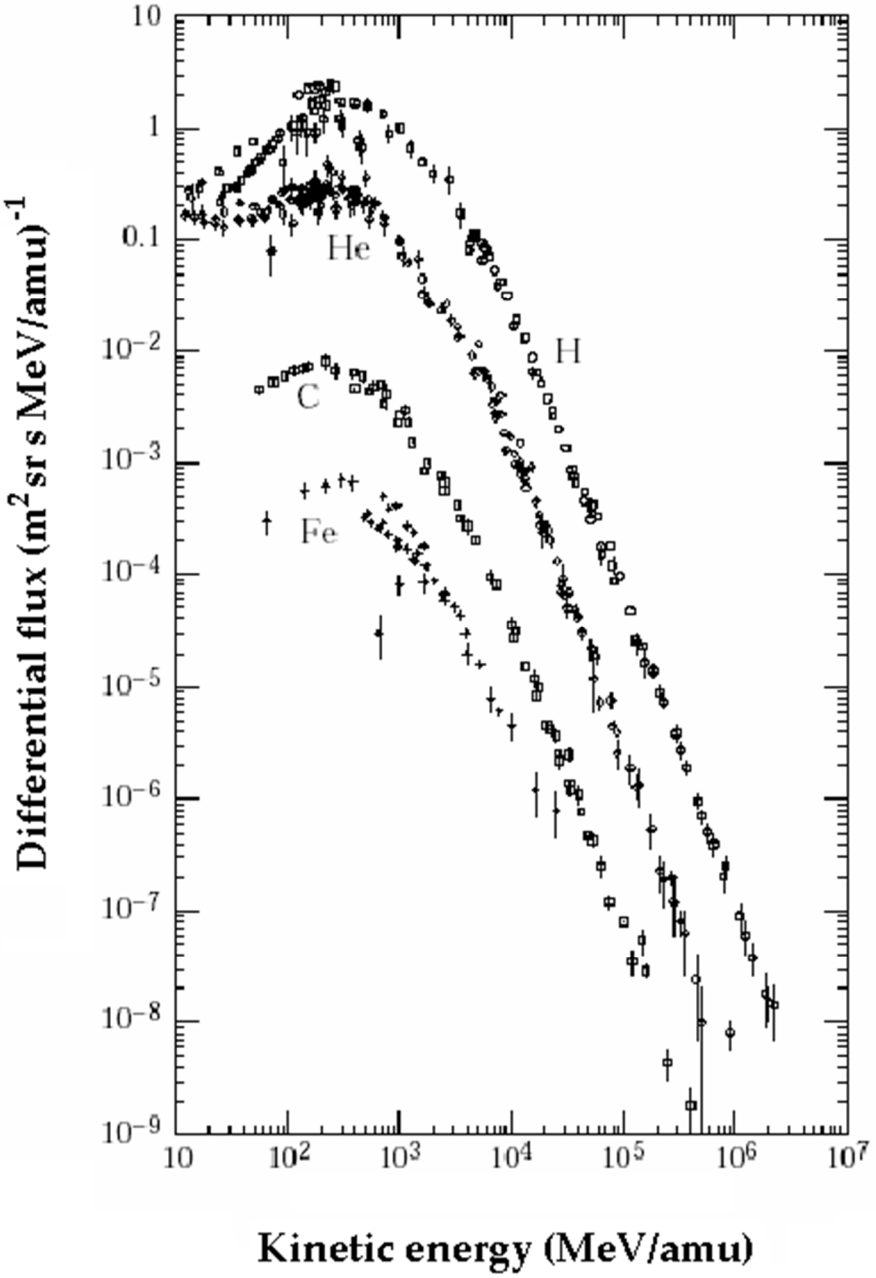

Figure 1. The energy spectra of hadronic galactic cosmic rays [9].

I.3 Validation and verification of radiation transport codes

As shown above, characterizing the secondary neutron field created by helium ions is relevant for medical and space applications. Existing Monte Carlo transport codes such as PHITS [11], FLUKA [12], MCNP [13] and GEANT4 [14] are capable of calculating secondary neutron and charged particle yields. These transport codes rely on accurate cross section and thick target data to build reliable physics models, and experimental data are also necessary for validating the physics models; however, the relevant benchmark measurements of helium ions are still limited. The thick target measurements and cross section measurement with respect to helium ions that have been previously done are listed, respectively, in Table 1and Table 2 [9].

Table 1. Existing measurements of ^{4}He-induced secondary neutron thick target yields (stopping or thick targets).

^{4}He energy (MeV/nucleon)	Target materials	Angles of measurement (degrees)
100	C, Al, Cu, Pb	0, 7.5, 15, 30, 60, 90
155	Al	10, 30, 45, 90, 120, 150
160	Pb	0, 45, 90, 120, 150
177.5	C, water, Steel, Pb	0, 6, 15, 30, 45, 60, 90, 120, 135, 150
180	C, Al, Cu, Pb	0, 7.5, 15, 30, 60, 90

Table 2. Existing measurements of ^{4}He-induced secondary neutron production cross section (thin targets).

^{4}He energy (MeV/nucleon)	Target materials	Angles of measurement
135	C, Al, Cu, Pb	0, 15, 30, 50, 80, 110
230	Al, Cu	5, 10, 20, 30, 40, 60, 80

To address the need for more experimental data, the measurement of double differential spectra of secondary neutrons created by 100- and 230 MeV/nucleon helium ions bombarding various thick targets were proposed to be run at the Heavy Ion Medical Accelerator in Chiba (HIMAC) of the National Institute of Radiological Sciences (NIRS) in Japan. The projectile energies were selected within the available beam energies that HIMAC can deliver (< 230 MeV/nucleon). These two energies aimed to not only cover the therapeutic demand in heavy ion therapy but also represent the low-energy end of the fluence peak of the GCR helium. The stopping targets were chosen to be water, polymethyl methacrylate (PMMA), and iron for the following three reasons. 1) Water is the major and essential compound in the human body and is used as a surrogate for a tissue-equivalent material. 2) PMMA is a surrogate tissue material and is commonly used in radiotherapy QC/QA. It is also used sometimes for beam line components, such as ridge filters. 3) Iron is chosen to represent certain beam line and spacecraft components; iron is one of the elemental components of the Martian soil, and the albedo dose created by GCR and SEP has to be taken into consideration for exploration activities on Mars.

To help lead to improvements in the default physics models implemented in PHITS, FLUKA and MCNP, the model calculations done by these codes were compared with the experiment results. An inter-comparison of the model calculations done by these codes with the existing neutron production cross section data was also conducted.

I.4 Original contribution

The stopping target measurement of secondary neutrons created by 100- and 230-MeV/nucleon ^{4}He ions in this study has not been previously performed with these combinations of beam energies and target materials. The experiments

performed here will provide new data for validation of physics models describing ^{4}He-induced nuclear reactions. In addition, the experimental data at backward angles are critical for validation of heavy-ion-induced reaction models due to their extreme kinematics. Most of the previous heavy-ion experiments only measured the neutron spectra at emission angles up to 90°, whereas the neutron spectra at a backward angle (121.2°) were measured in this experiment.

In addition to providing new experimental data, the benchmark calculations of neutron production cross sections also provide critical information for model developers to improve their physics models. Previous benchmark studies compared only a few sets of experimental data with one or two model calculations. However, a wide range of target nuclei mass with various combination of beam species in an energy range of 135 – 600 MeV/nucleon is covered in this benchmark study. Moreover, every set of experimental data is compared with the model calculations fulfilled by three of the wide-spread Monte Carlo radiation transport codes. Such sizable and systematic benchmark study for heavy-ion induced nuclear reactions at hundreds of MeV/nucleon has not been conducted with the latest version of PHITS, FLUKA, and MCNP codes at the same time. Since these Monte Carlo transport codes are implemented with different physics models, the benchmark results can help examining the physics assumptions of each model and lead to more accurate prediction of secondary neutrons produced from heavy-ion interactions.

CHAPTER II
SECONDARY NEUTRONS PRODUCED BY HELIUM IONS BOMBARDING STOPPING TARGETS

This chapter covers the experiment target design by using PHITS calculations, the experimental setup, data analysis, and the measurement results along with the PHITS, FLUKA and MCNP simulations in each section.

II.1 Experiment target design

During the literature survey of stopping target measurements either for helium ions incident on various targets [16 - 19] or carbon ions at therapeutic energies bombarding tissue surrogate targets [20, 21], it was found that the ratio of the ion beam range (R) to the target depth (d) (the length along the beam direction) varies from 0.50 to 0.98. Since the results of thick target measurements are the overall results of production of secondary particles for nuclear reactions followed by the attenuation and transport within the thick target, the difference in the values of ratio R/d makes the comparison of experimental data complex and requires accurate adjustments applied to those data sets. Hence, in order to determine the target size for our experiment as well as to seek a general trend resulting from the change of target geometries, the quantitative influence on secondary particle angular distribution by changing the stopping target dimensions was investigated by a Monte Carlo radiation transport code, PHITS. There were two variables of a cuboid target that were studied; one is the target depth (d) and the other one is the target cross sectional area (A_{cs}). All of the beam-target simulation combinations can be found in Table 3.

Table 3. The various beam-target simulation cases.

^{4}He energy (MeV/nucleon)	**Target**	**Target cross sectional area (A_{cs})** (cm x cm)	**Target depth (d)** (cm)	**Ratio of range/depth***
100	water	5 x 5	8, 9, 11, 13	0.97, 0.86, 0.71, 0.60
	water	10 x 10 20 x 20	9	0.86
	iron	2 x 2	1.5, 1.6, 2.0, 2.4	0.97, 0.91, 0.73, 0.61
	iron	3 x 3	1.6, 2.0	0.91, 0.73
	iron	10 x 10	1.6	0.91
230	water	5 x 5	34, 37, 45, 55	0.97, 0.90, 0.74, 0.60
	water	10 x 10 20 x 20	37	0.90
	iron	2 x 2	6.2, 6.6, 10.0	0.98, 0.92, 0.61
	iron	3 x 3 10 x 10	6.6	0.92

* The reference systems that are highlighted in yellow are used for comparison of angular distributions in the same beam-target material combination.

II.1.a PHITS simulations

The experiment target design was performed by the Monte Carlo code PHITS version 2.64 (Particle and Heavy Ion Transport code System) [11]. The physical processes in PHITS include collisions with nuclei and transport between collisions. With continuous-slowing-down approximation, stopping powers were calculated by SPAR [22] for nuclei, protons, pions, and muons, and by NMTC forthe others. For collisions with nuclei, the nuclear data library (JENDL-4.0) was used for neutron energies up to 20 MeV, and intra-nuclear cascade model INCL4.6 [23] was used as the default model to simulate triton-, ^{3}He-, ^{4}He-, and nucleon-induced nuclear reactions. The transport cut-off energy was set to 1 keV/nucleon for charged particles and 0.01 eV for neutrons. Gamma emission was also included.

The simulation geometry is illustrated in Figure 2. A uniform ^{4}He beam with 1.0 cm diameter started at 10 cm upstream of the target and was incident perpendicularly to the front face of the target. Seven scoring regions were set up respectively at 0°, 10°, 20°, 30°, 60° and 120°, referenced to the target center. In order to improve statistics and shorten computational time, the scoring regions were designed as ring-shaped cylinders with 10 cm width (the outer radius minus the inner radius) and 10 cm thick. Thus the angular ranges of each scoring region are 0°-1.15°, 9.09°-10.20°, 19.80°-20.81°, 29.90°-30.96°, 59.53°-60.26°, 89.14°-90.86°, and 119.74°-120.96°.

Experimentally, secondary particles are measured by a ΔE-E telescope at each angle. The ΔE-E telescope consists of a thin NE102 plastic scintillator and a thick EJ301 liquid scintillation detector. However, since the aim of this study is to investigate the influence of target depth and cross sectional area upon the angular distributions of the fragments, the scoring region was assumed to be void instead of realistic detector materials to avoid any interactions and attenuation within the detectors, and the rest of the space was assumed to be air, except for the target.

II.1.b Simulation results for varying target depth

The influence of target depth upon the angular distributions of secondary particles is a point of interest. To quantify that influence, the relative fluence at each scoring angle was obtained by normalizing the fluence in the systems with various target depths to the fluence at the corresponding angle in the reference system, whose target R/d value equals to 0.97 or 0.98, as yellow-highlighted in Table 3. For example, the 230-MeV/nucleon ^{4}He induced neutron fluences at 10° from water targets with different depths were all divided by the neutron fluence at 10° from 34-cm deep water target. Such relative neutron and proton fluences are shown in Figure 3 and Figure 4.

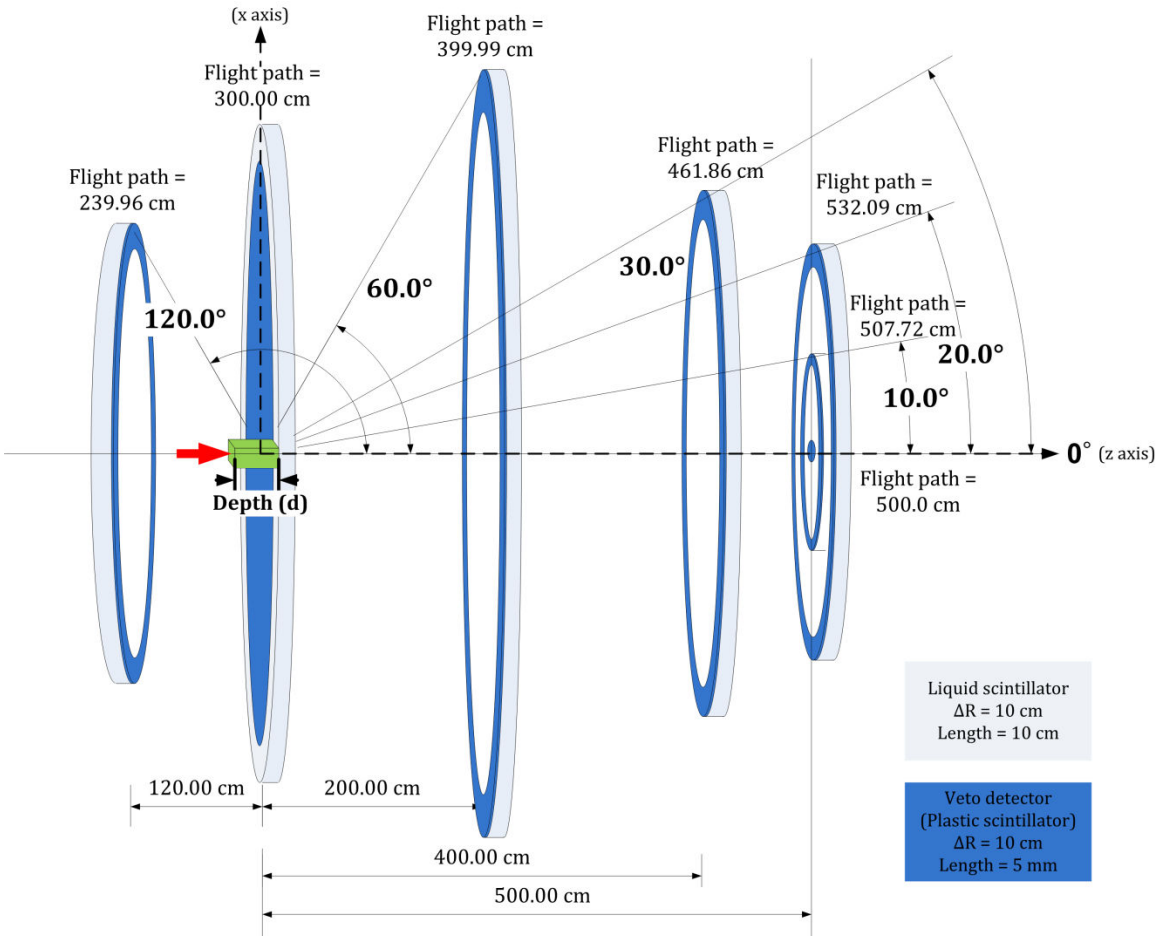

Figure 2. Schematic diagram of the simulation geometry.

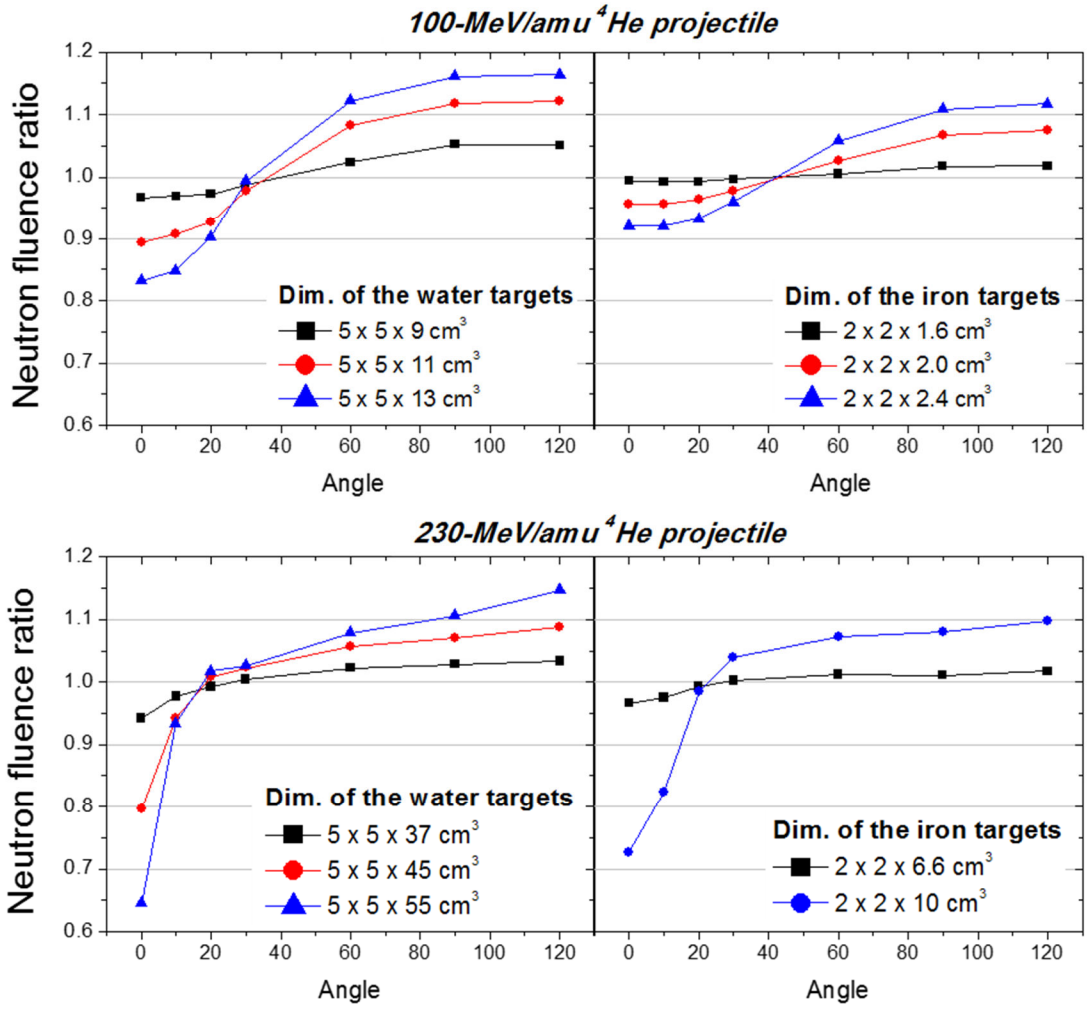

Figure 3. Normalized neutron angular distributions of different beam-target combinations with target depth as a variable.

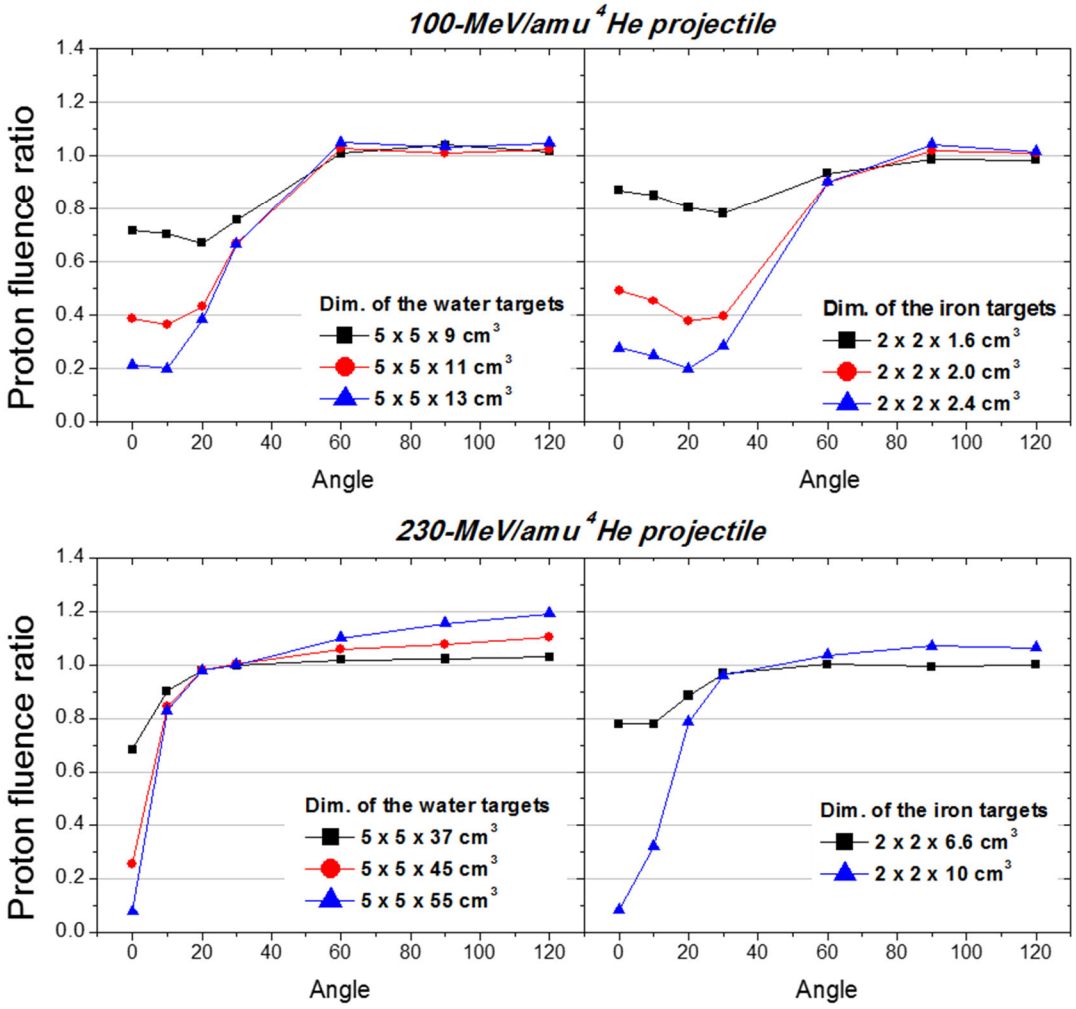

Figure 4. Normalized proton angular distributions of different beam-target combinations with target depth as a variable.

Most of the neutrons in the high-energy and forward regions are dominated by the breakup of the projectile and direct knock-on process due to the high velocity of incident projectiles. As the target depth increases, these high-energy and forward-focused neutrons have to go through more material, such that the neutron fluences are attenuated at forward angles, as shown in Figure 3. With the decreasing R/d ratio, the attenuation is more significant for lighter target mass and for higher-energy projectiles. The 230-MeV/nucleon ^{4}He-induced neutron intensity at 0° decreases to 64.5% of the 34-cm water target fluence when the depth is increased from 34 cm to 55 cm (R/d from 0.97 to 0.60), whereas the neutron intensity retains 92.1% of the 1.5-cm fluence when the iron target is bombarded by 100-MeV/nucleon ^{4}He ions and the depth is also increased from R/d = 0.97 to 0.61 (d = 1.5 cm to 2.4 cm).

At energies below 20 MeV, the spectra are dominated by target breakup that emits neutrons nearly isotropically, and as a result these target-like neutrons can be seen at all angles. Since deeper targets have more materials behind the primary ion range, more nuclear interactions may occur between the secondary particles and the target nuclei. As a result, the angular distribution outside the stopping targets becomes less forward peaked, and the secondary neutron fluences produced from thicker targets exceed the neutron fluences produced from the thinnest target at angles greater than 30°-40°, which can be seen in Figure 3. This neutron buildup effect is more evident for lighter target mass and for lower-energy projectiles. The 100- MeV/nucleon ^{4}He- induced neutron fluence at 120° with a 13-cm deep water target (R/d=0.60) is 116.4% of the value with the reference water target, while the fluence for an iron target with R/d=0.60 (d = 10 cm) bombarded by 230 MeV/nucleon ^{4}He is 109.8% of the reference value.

Regarding the secondary charged particles, most of the heavier charged fragments whose atomic number is only slightly less than the target element are easily attenuated and trapped within the target. Light secondary charged particles,

such as protons, deuteron, tritons, ^{3}He and etc., are attenuated to a higher degree than neutral particles but have a higher probability to escape from the target compared to high-Z fragments since the range of particles at the same velocity is proportional to A/Z^2. Even so, a slight increase in target thickness can decrease the proton intensity at forward angles by an appreciable amount. Looking at secondary protons, for example (as shown in Figure 4), the relative proton fluence at 0° decreases by 13.0% when the depth of iron target increases by 0.1 cm (R/d=0.97 to 0.91) with 100-MeV/nucleon ^{4}He bombardment. At backward angles, such as 120°, the relative proton fluence in the 230- MeV/nucleon projectile system can increase by 19.1% if the water depth increases from 34 cm to 55 cm (R/d=0.97 to R/d=60).

II.1.c Simulation results for varying target cross sectional area

The changes in angular distributions caused by varying the target cross sectional area (A_{cs}) are shown in Figure 5 for secondary neutrons and Figure 6 for secondary protons. While considering the various target A_{cs}, it is necessary to consider the average distances for secondary particles from locations being created within the stopping targets to the scoring regions at each angle. In addition, it is reminded that the minimum target depth required to stop the primary ions are dependent on not only the beam species and beam energy but also the target material. Figure 7 shows two detailed pictures of the thick iron targets for 100-MeV/nucleon ^{4}He projectiles and the thick water targets for 230-MeV/nucleon ^{4}He projectiles, which have the thinnest and the thickest targets among our four studied systems. Assuming a nuclear reaction occurs at the target center, from Figure 7, it is very clear that the traveling distances for secondary particles are almost identical for emitting angles smaller than 51° and 8° respectively for the thinnest iron targets and the thickest water targets if A_{cs} is increased.

As a result, it is both seen in Figure 5 and Figure 6 that with the increasing A_{cs}, the angular distributions of neutrons and protons remain alike or slightly higher

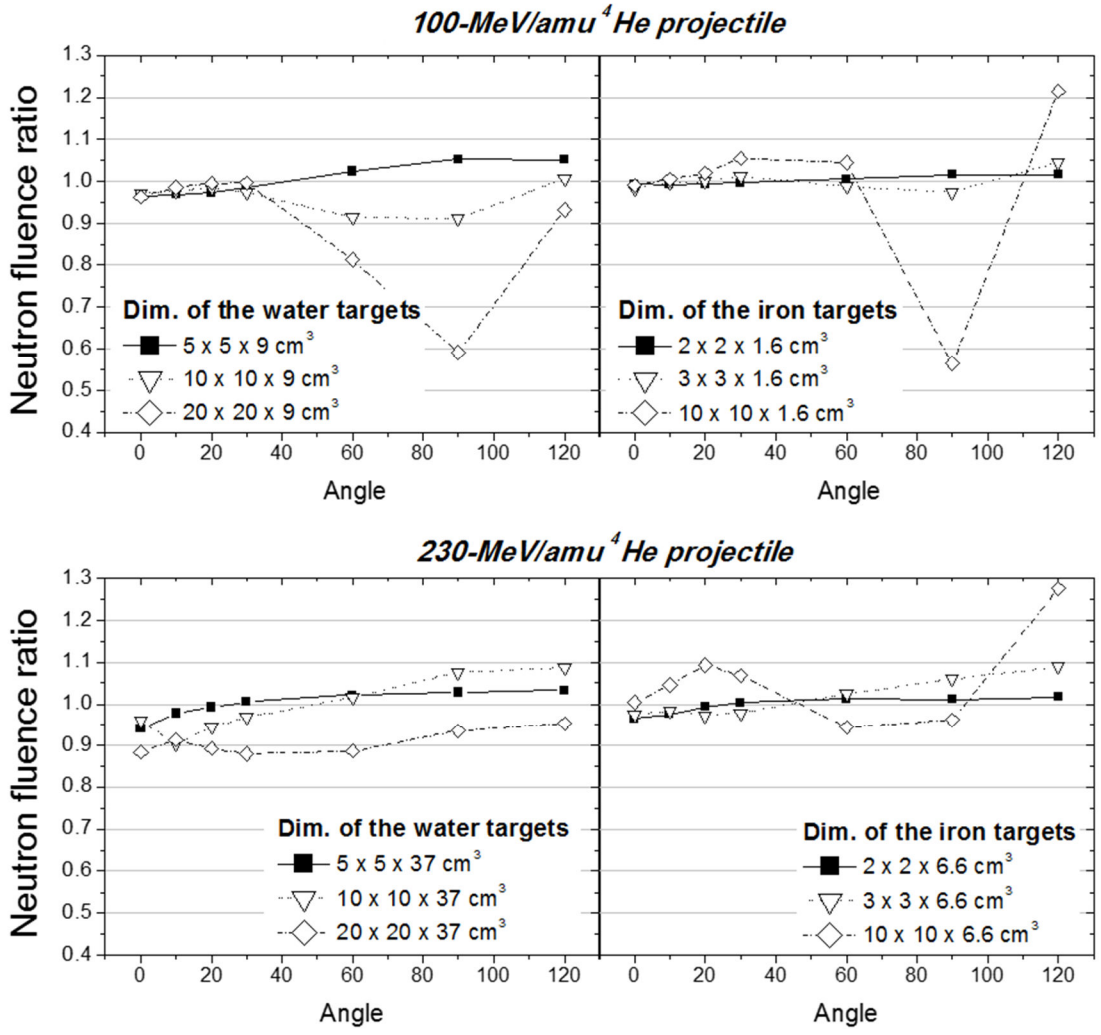

Figure 5. Normalized neutron angular distributions of different beam-target combinations with target cross sectional area (A_{cs}) as a variable.

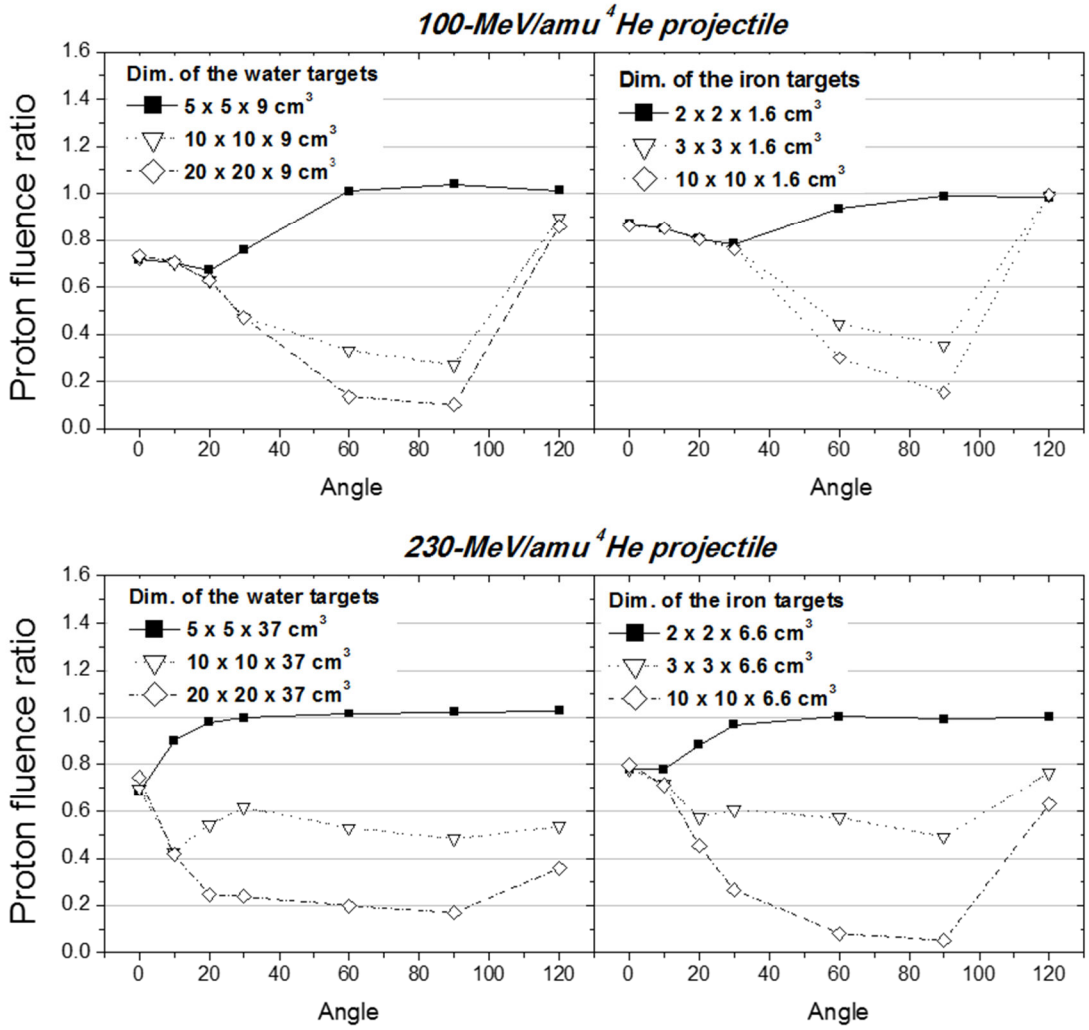

Figure 6. Normalized proton angular distributions of different beam-target combinations with target cross sectional area (A_{cs}) as a variable.

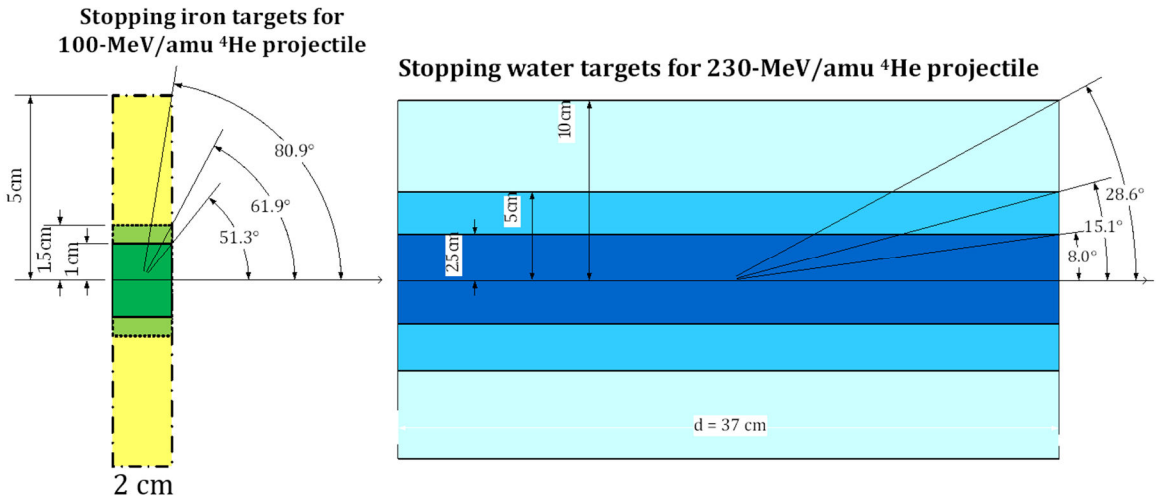

Figure 7. Geometries of the iron targets for 100-MeV/nucleon ^{4}He projectiles (left) and the water targets for 230-MeV/nucleon ^{4}He projectiles (right).

at angles < 30° in the 100-MeV/nucleon ^{4}He projectile systems. This is as expected since the path length of the secondary particles going through is identical, with a slight contribution from the target side. As the angle increases, the attenuation of the secondary particles becomes more severe until angles > 90° where the contribution of the target breakup from the larger target becomes significant.

However, the influence of the target cross sectional area in the 230-MeV/nucleon ^{4}He projectile systems is unique for each case and no general trend is found, which is not only because the attenuation capability and the secondary fragments production cross section are dependent on target material, but is also due to the requirement that the thick target geometry is dependent on various factors including the beam species, beam energy, and target materials. Hence, while comparing measured data form two systems with different A_{cs}, adjustments are necessary to take both the loss and production of particles in the thick targets into consideration.

II.1.d Summary of target geometry study

The influence of the depth and the cross sectional area of stopping water and iron targets on the fluences and angular distributions of secondary particles induced by 100- and 230-MeV/nucleon ^{4}He ions was studied using the Monte Carlo simulation code PHITS. The secondary charged particles and secondary neutrons which come from the breakup of projectiles are highly forward-focused, whereas the secondary particles produced by target breakup are nearly isotropic. As the energy of ^{4}He ions increases from 100 MeV/nucleon to 230 MeV/nucleon, the normalized intensities of charged particles decrease less rapidly with increasing angles. When the target depth increases, the impact on the attenuation of secondary particles is more significant for lighter target mass and higher-energy projectiles at forward angles. Also, with deeper targets, more interactions occur between the secondary particles and the target elements, which results in a buildup of the fluence from more target-like fragments at large and backward angles.

With respect to the cross sectional area of the stopping targets, the forward angular distributions are similar regardless of cross sectional area. The fluences of secondary charged particles are highly reduced at large angles; however, no general rule was found for secondary neutrons at large and backward angles. If one wants to compare the angular distributions from the systems with identical projectiles and target materials but with different target geometry, there is no simply analytical solution to correct the angular differences caused by different target geometries. It is therefore strongly suggested to utilize a radiation transport code to incorporate the influence from the target geometry in stopping target measurements.

II.2 Experimental setup

The experiment of measuring angular distributions of secondary neutrons produced by 100- and 230-MeV/nucleon ^{4}He ions bombarding stopping water, PMMA and iron targets was conducted in June 2014 at the Heavy Ion Medical Accelerator in Chiba (HIMAC) of the National Institute of Radiological Sciences (NIRS) in Japan. A sketch of the experimental setup is shown in Figure 8, and Figure 9 is a picture showing the actual setup at HIMAC.

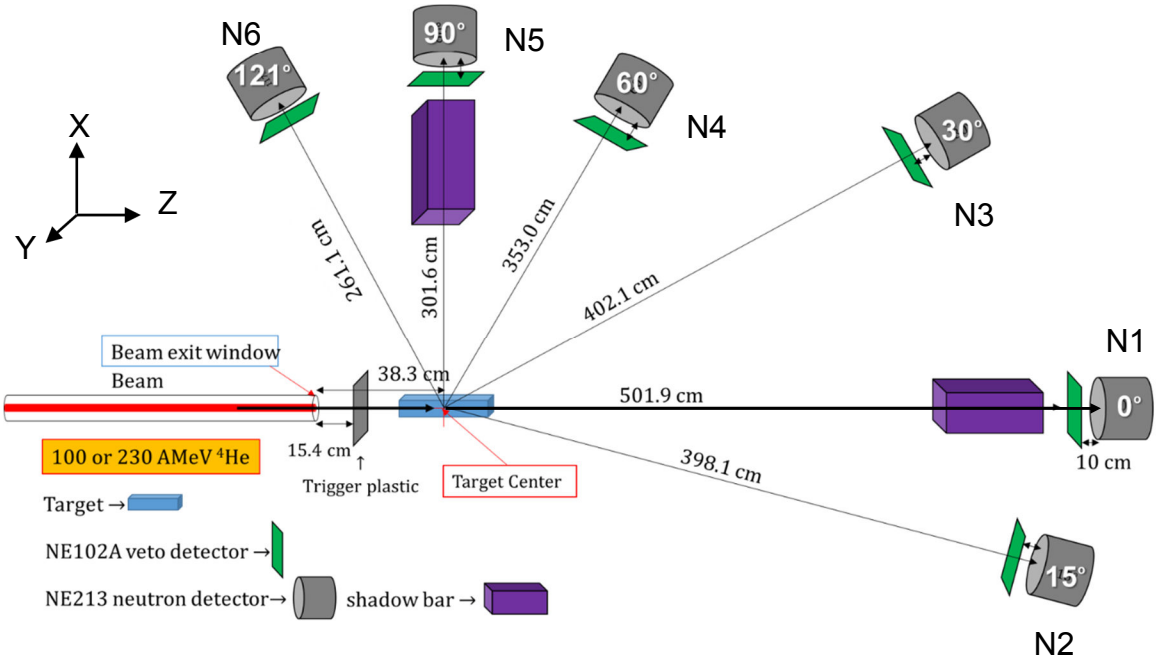

Figure 8. The experimental setup of the HIMAC measurement.

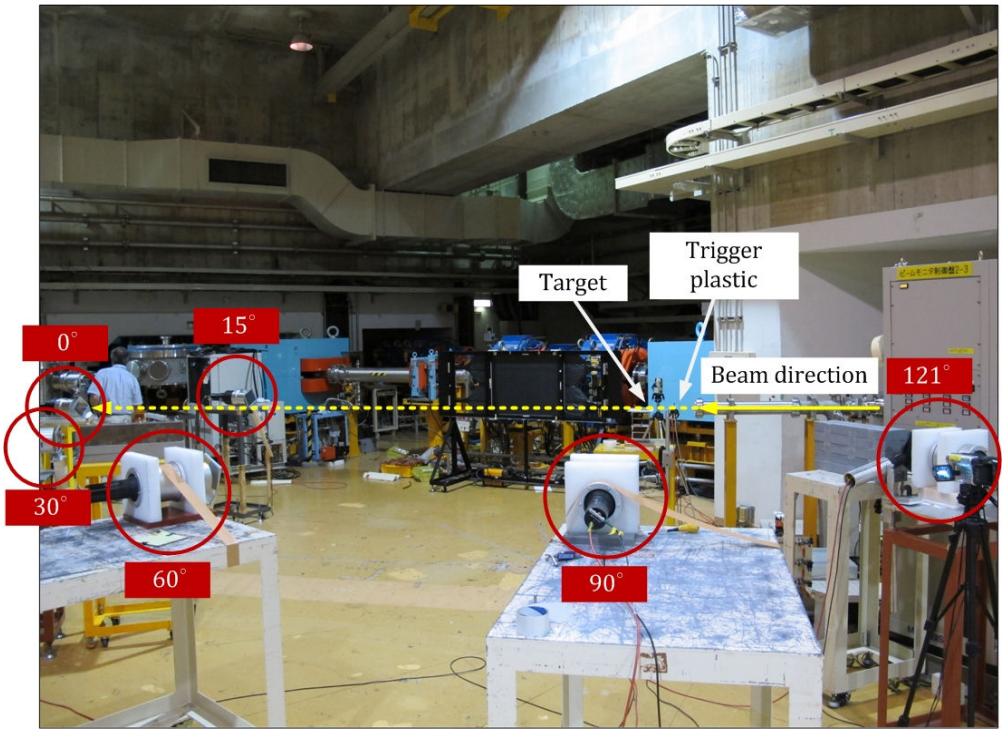

Figure 9. A picture of the experimental setup at HIMAC.

II.2.a Beam and target characteristics

Helium ion beams were delivered along the PH2 beam line at HIMAC. Along the beam line, gas wire chambers followed by a beam checking phosphor were placed just upstream of the target position. The beam profiles were measured by gas wire chambers and were approximately Gaussian distributions horizontally and vertically with the standard deviations 2.08 to 2.52 mm. Both of the gas wire chambers and the beam checking phosphor were removed during data runs. The beam was delivered to the target about 18 spills per minute, and the duration of each spill lasted between 0.5 and 1 second depending on the beam type. The beam intensities varied roughly from $8x10^4$ to $2x10^5$ particles per spill.

Figure 10 shows the setup for the trigger plastic and the targets. After exiting the aluminized Mylar window with a 10 mils thickness, the ^{4}He ions were detected

by a trigger plastic scintillator (TP), which is made of NE102 and is 0.5 mm thick with an area of 5 cm by 5 cm. The TP was used in the trigger, which will be described in detail in section II.2.c Electronics and data acquisition. The counts in the TP provided the number of incoming beam particles and were used for normalizing different runs.

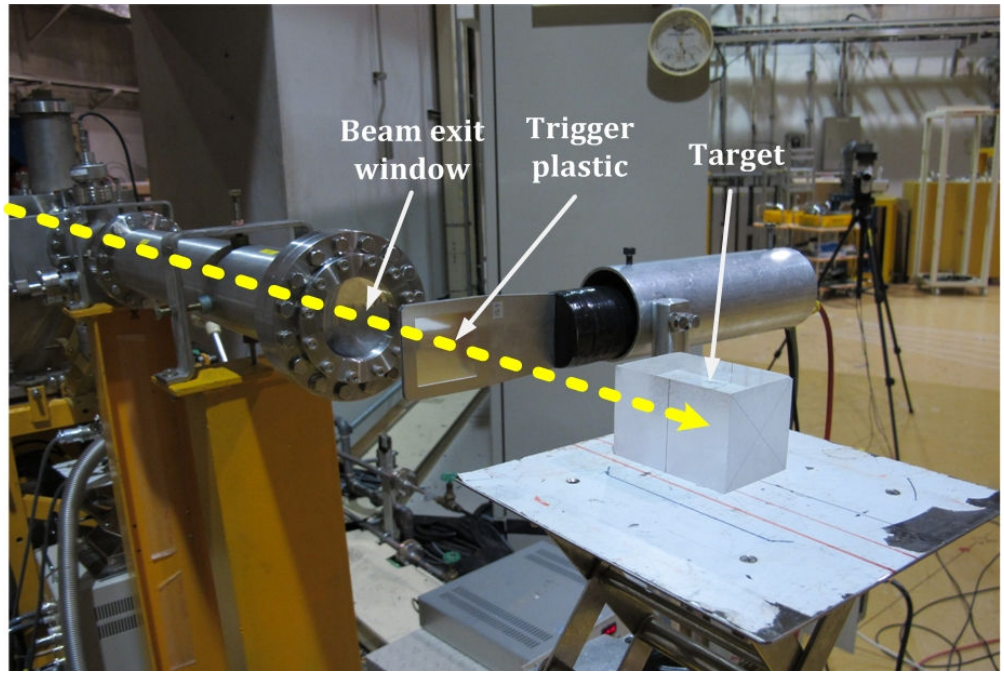

Figure 10. A closer look of the trigger plastic and the target setup.

All of the targets were thick enough to fully stop the primary ions. The ranges of ^{4}He ions in target medium were calculated by SRIM 2013 [24] (for water targets) and retrieved from the range table for helium ions provided by NIST [25] (for PMMA and iron). The information for ion ranges, target dimensions, and the ratio of ion range to target thickness is listed in Table 4. The water containers are made with 3.175-mm thick PMMA walls at each side (the outer dimensions are listed in Table

4), and the containers were filled with pure water. Polymethyl methacralate (PMMA) is also called acrylic, lucite, or plexiglass. Its molecular formula is $(C_5O_2H_8)_n$, and its density is 1.19 g/cm^3.

Table 4. Details of the stopping targets.

Target	Range for ^{4}He (R)	Target dimensions (width x height x thickness)	R/t ratio
100-MeV/nucleon ^{4}He beam			
Water container - Wall - Water	7.590 cm	Wall thickness: 3.175 mm Outer dimensions: 5.035 cm x 5.385 cm x 8.900 cm	
PMMA	6.697 cm	5.08 cm x 5.08 cm x 7.62 cm	0.879
Iron with 99.5% purity	1.452 cm	2.10 cm x 2.10 cm x 1.71 cm	0.849
230-MeV/nucleon ^{4}He beam			
Water container - Wall - Water	32.600 cm	Wall thickness: 3.175 mm Outer dimensions: 4.690 cm x 5.260 cm x 37.200 cm	
PMMA	28.580 cm	5.08 cm x 5.08 cm x 31.75 cm	0.900
Iron with 99.5% purity	6.053 cm	2.10 cm x 2.10 cm x 6.60 cm	0.917

The target center was defined as the origin of the beam-target Cartesian coordinate system: the +Z axis was along the beam incident direction, as illustrated in Figure 8. The center of the beam exit window was at Z = -38.3 cm, and the front surface of the trigger plastic scintillator was at Z = -22.9 cm. The height from the floor to the target center was 125 cm.

II.2.b Measurement methods

The secondary particles created inside the stopping targets include both neutral particles (neutrons and photons) and light charged ions, such as protons, deuterons, tritons, ^{3}He, etc., which might have enough energy to travel through the target medium and air and be detected. These secondary particles were detected by six sets of ΔE-E telescopes at 0°, 15°, 60°, and 90° for the 100-MeV/nucleon ^{4}He beam configuration, and at 0°, 15°, 30°, 60°, 90°, and 121.2° for the 230-MeV/nucleon ^{4}He beam, with respect to the beam direction (on the Y-Z plane). Each ΔE-E telescope used in this study consisted of a thin NE102A organic plastic scintillation detector (ΔE detector) and an NE213 organic liquid scintillation detector (E detector).

The NE102A, BC400, and EJ212 scintillators are three commercial equivalent plastic scintillators[1], with the same density of 1.023 g/cm^3 and the same composition ($C_{10}H_{11}$). Two NE102A detectors and four BC400 plastic scintillation detectors were used in the experiment. Their area size is the same, 12.7 cm by 12.7 cm, but the NE102A detectors have a thickness of 6.35 mm (0.25 in) and the BC400 detectors have a thickness of 5 mm. NE213, EJ301, and BC501A liquid scintillators are the commercial equivalents[1] to each other. Three NE213 and three EJ301 detectors were used in this experiment. The NE213 scintillator has great pulse shape discrimination (PSD) properties and is widely used for fast neutron spectroscopy in a gamma-neutron mixed field [26]. The composition of NE213 includes xylene, activators, the organic compound POPOP (as a wavelength shifter), and naphthalene (added to improve light emission). Its chemical formula is $C_6H_4(CH_3)_2$, and its density is 0.874 g/cm^3. All of the NE213 and EJ301 liquid scintillators used in this study are filled in a 12.7-cm diameter and 12.7-cm high

[1] Nuclear Enterprise Ltd, Edinburgh, UK (NE) was the first on the market, and then St. Gobain Crystals/Bicron Radiation Measurement Products, Newbury, OH, USA (BC) followed by Eljen Technology, Sweetwater, TX, USA (EJ).

cylindrical chamber with an aluminum housing. The thickness of front aluminum face is 1.524 mm (0.06 in) and 1.5 mm respectively for the EJ301 and the NE213 detectors.

Since the solid plastic scintillator is very thin and consists of only hydrogen and carbon atoms, photons and neutrons have a very small probability of interacting within the detector while passing through it, while charged particles will lose energy in the plastic scintillator with practically 100% efficiency, and then deposit the rest of their energy in the liquid scintillator. By combining the coincidence signals from the NE102A (ΔE) detector and the NE213 (E) detector, the species of charged particles can be identified from two-dimensional ΔE-E plots because the specific energy loss is unique to ions with different atomic number (Z) and mass number (A) at a certain energy. The plastic scintillators in ΔE-E telescopes are also called veto detectors as they are used to discriminate neutral particles from charged particles. After applying the charged particle discrimination by veto detectors, neutrons and photons can be separated by using the PSD of NE213 detectors.

The kinetic energy of the secondary particles, including neutrons and charged particles, was determined by their time of flight. The flight paths as shown in Figure 8 were defined from the target center at (0, 0, 0) to the front surfaces of each liquid scintillation detector; they were 501.9 cm, 398.1 cm, 402.1 cm, 353.0 cm, 301.6 cm, and 101.3 cm (in the 100-MeV/nucleon ^{4}He system) or 261.1 cm (in the 230-MeV/nucleon ^{4}He system), respectively for 0^{0}, 15^{0}, 30^{0}, 60^{0}, 90^{0}, and the backward angle (117.5^{0} for 100-MeV/nucleon ^{4}He beam configuration and 121.2^{0} for 230-MeV/nucleon ^{4}He beam configuration). The start and stop signals were obtained from the EJ301 detector and the trigger plastic scintillator (TP), respectively. Once the flight time is determined, and the flight path is a known parameter, the particle energy can be acquired by using the relativistic relations:

$$T = (\gamma - 1) m_0 c^2 \text{ , and} \tag{1}$$

$$\boldsymbol{\beta = \frac{v}{c} = \left(\frac{L}{t}\right)\frac{1}{c} = \sqrt{1 - \frac{1}{\gamma^2}}.} \tag{2}$$

Then the kinetic energy as a function of the time of flight (tof) is given by

$$T = \left(\frac{1}{\sqrt{1 - \left(\frac{L}{tc}\right)^2}} - 1 \right) m_0 c^2 \text{ ,} \tag{3}$$

where T is the particle kinetic energy, L is the flight path, defined from the target center to the front surface center of the EJ301 liquid scintillator, t is the time of flight (ToF), $m_o c^2$ is the particle's rest mass.

If the uncertainty of the flight path is neglected, the relative energy resolution (dT/T) is dependent on the time resolution (dt) of the tof spectra, given by the Gaussian error propagation of Eq. (3). The relationship can be expressed by the following equation.

$$\frac{dT}{T} = -\gamma(\gamma + 1)\frac{dt}{t} \text{ ,} \tag{4}$$

where the time resolution dt is usually taken from the observed FWHM of the prompt gamma ray peak in the tof spectra, or 2.354 times of the standard error (σ) of the photon peak if the peak is fitted by a Gaussian distribution.

Normally, the time of flight measured by the TDC (denoted to t_{TDC}) starts at the trigger plastic signal and stops at the liquid scintillator signal. In other words, if we presume that the cable lengths going from the TP and from the liquid scintillator and thus the signal transit times are identical, then t_{TDC} is the sum of the time for

a primary ion passing through the trigger plastic to the target location where a nuclear interaction occurs (t_p) and the time of the measured particle from the reaction point to the liquid scintillator (t) ($t_{TDC} = t_p + t$).

For the time-to-energy conversion the simplifying assumption was made that the nuclear fragmentation reaction take places at the target center and the detector signal is created at the detector's front surface, i.e.

$$t_{TDC} = t_{TP \rightarrow 1/_2 target} + t_{1/_2 target \rightarrow liquid\ scintillator}, \text{ and} \quad \textbf{(5)}$$

$$t = t_{1/_2 target \rightarrow liquid\ scintillator}. \quad \textbf{(6)}$$

However, our previous presumptions in terms of the transit may not be always true. Therefore we have to use the prompt gamma ray peak to "set the clock" in the TDC spectra. An example of how the tof is calculated in the data analysis is presented in section II.3.b Spectra analysis.

To obtain an accurate measurement of the neutron production, background is also an important factor that has to be taken into consideration. The primary source of background neutrons comes from room scattered neutron that eventually strike the detector. Thus for each beam-target configuration, measurements were carried out with and without an iron shadow bar in front of the ΔE-E detector set. We ran four configurations for each beam/target combination, which were the following:

1) without shadow bars,
2) two shadow bars respectively in front of the 0° and the 90° detector sets,
3) two shadow bars respectively in front of the 15° and the 60° detector sets,
4) two shadow bars respectively in front of the 30° and the 121.2° detector sets.

The iron shadow bars were 60 cm long with area slightly larger than the detector's front face, and were placed periodically between the target and the

detectors in order to block secondary nuclear fragments coming directly from the target, allowing only room scattered background particles to enter the detector. Figure 11 shows two pictures of the measurement with shadow bars.

II.2.c Electronics and data acquisition

The electronic logic diagram of the experimental setup is plotted in Figure 12. The anode signals of each liquid scintillation detector were split twice. Two of the split signals were applied with different delay time and fed into a charge-to-digital converter (QDC, LeCroy 2249W, CAMAC), where the signals were integrated over a 400-ns gate for PSD; the other split signal was fed into a constant-fraction discriminator (Quad CFD, CANBERRA 454, NIM), and then was jointed with five logic signals from the other five liquid scintillation detectors into an “OR” logic coincidence module.

The TP signal was split once; one signal was fed into a QDC to obtain the pulse height spectrum of primary ^{4}He ions, and the other one was fed into a CFD to generate logic signals. Two outputs of this CFD were used, one of which was delayed and served as the STOP signal of a time-to-digital converter (TDC, LeCroy 2228A, CAMAC) for the time-of-flight measurement, and another one of which was fed into a gate and delay generator to generate 400-ns long logic signals and then into an “AND” coincidence module with the “OR” signal of six liquid scintillator detectors. As such, if any one of the liquid scintillators’ signals arrived in coincidence with the signal from the TP, an event was triggered. For investigation of which detectors fired the trigger, the logic signals from the six liquid scintillators were also delayed 200 ns and fed into a TDC for self timing.

The output of the “AND” coincidence counted the total number of coincidence events; these events were further put into another “AND” coincidence with “COMPUTER NOT BUSY” signal to obtain the live events (“live” here means an event which was processed by the data acquisition system). The output from

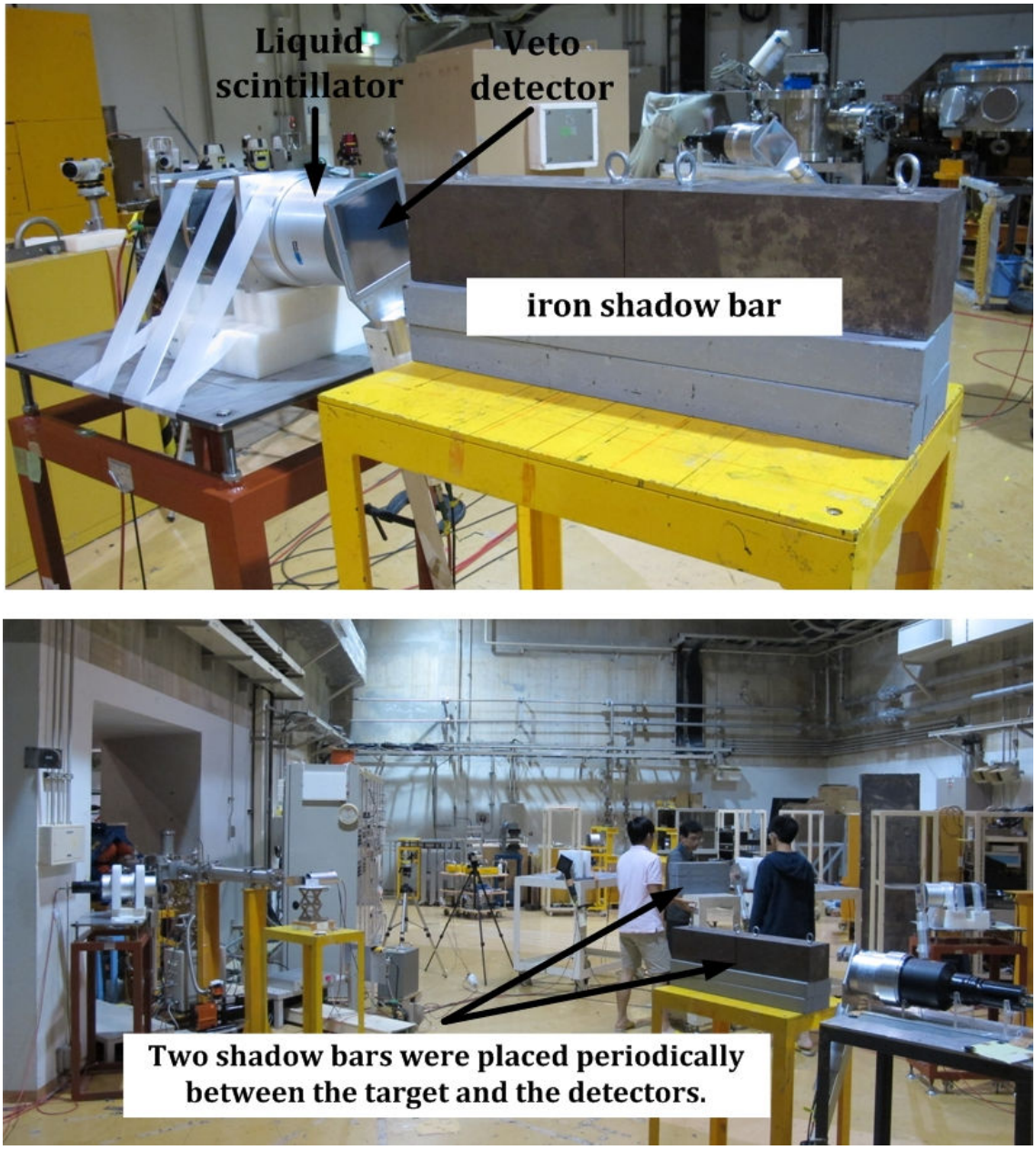

Figure 11. Two pictures showing the measurement with shadow bars.

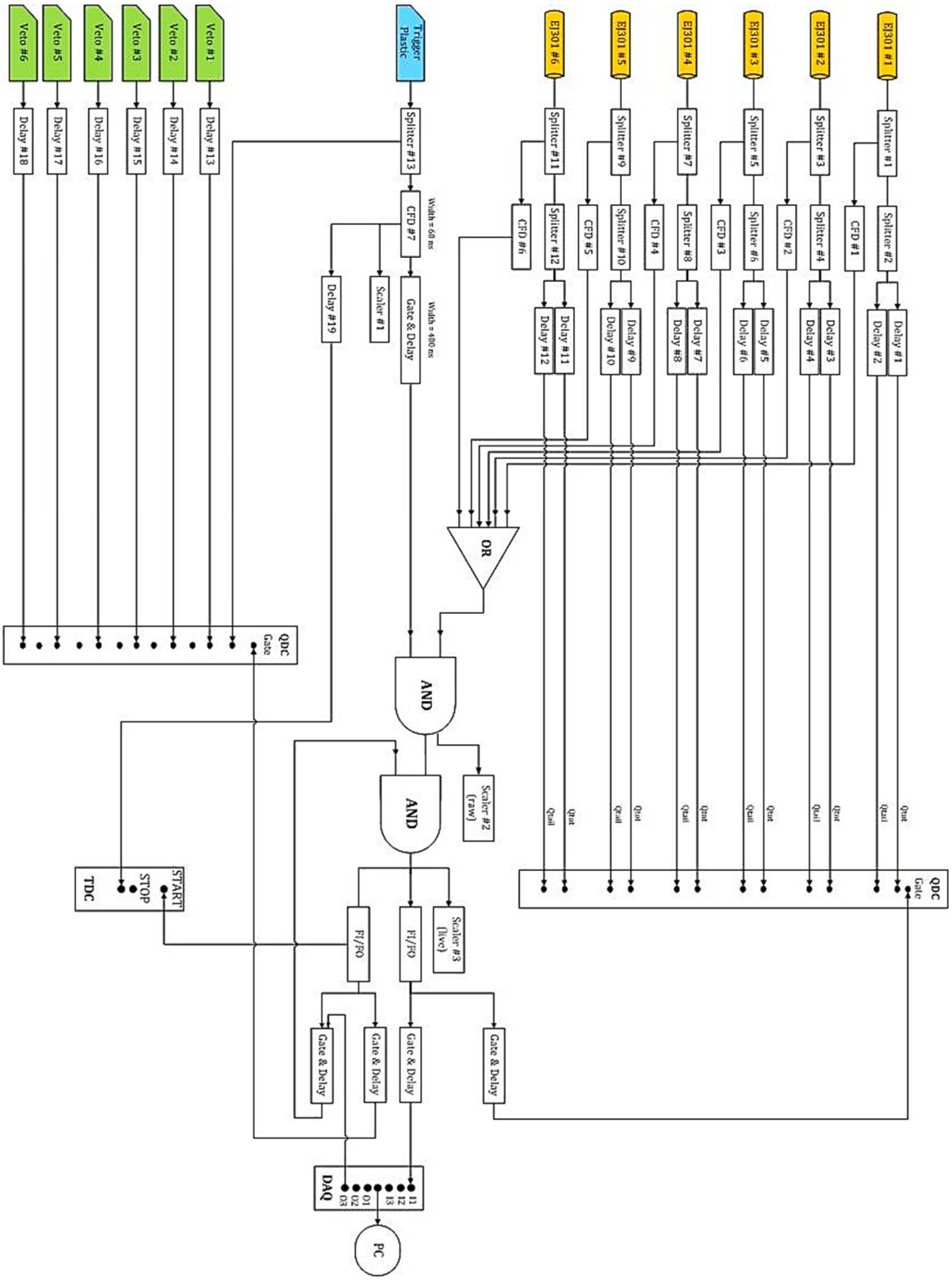

Figure 12. The block diagram of electronic logic.

the second “AND” coincidence also served as the START signal of the TDC for time-of-flight measurement.

It is noted that, normally the clock of time-of-flight starts at the TP signal and then stops at the coincident neutron detector signal. However, in order to ensure that for every start signal had a corresponding stop signal and thus to reduce the counting dead time, in our experimental setup, the clock was inverted and started with the arrival of the neutron detector signal in the coincidence circuit, and stopped by the delayed TP signal.

The veto detectors were delayed for a certain amount of time such that any coincident signals were within the charge integration gate for the EJ301 signals, and then fed into a QDC to obtain the distribution of the total amount of charge in a pulse. The veto detectors were not set in coincidence with the liquid scintillation detectors. The charged particle discrimination mentioned above was achieved offline using analysis software afterwards. All the data were recorded event-by-event by using a CAMAC data acquisition system.

II.3 Data analysis

The experimental data were recorded in an event-by-event mode with binary data format. To obtain the final experiment results, i.e. the double-differential spectra of secondary particles, the raw data had to be converted into a readable data format for analysis software, and the wanted events had to be filtered out to perform the analysis tasks. Two analysis programs were used in this study. One is SpecTcl, which is developed by the National Superconducting Cyclotron Laboratory at the Michigan State University; the other data analysis tool is ROOT, which is developed by CERN and is commonly used in particle physics experiments.

For reasons stated earlier, this work focusses on neutron production in the thick target measurements. The analysis tasks included 1) pulse height calibration of neutron detectors and time calibration of TDCs, 2) neutron, gamma, and charged particle discrimination, 3) time-of-flight spectra analysis, 4) double differential spectral determination, and 5) the application of corrections for detector efficiencies, acquisition dead time, and other experimental effects. Each of the analysis tasks are briefly described below.

II.3.a Energy calibration and time calibration

The measurement of neutron energy with organic scintillators requires a precise calibration of the pulse height response to recoil proton energy. Because standard neutron sources or proton sources are less accessible than gamma-ray sources, experimentally the calibration is done most often by using gamma-ray sources to identify certain locations in the pulse height spectrum corresponding to particular Compton electron energies, and then converting the electron equivalent energy (units in keVee or MeVee) to the recoil proton energy (units in keV or MeV) based on their pulse shape characteristics.

Generally the peak or the half-height of the Compton edge in the Compton spectra is selected, and the energy corresponding to those locations is obtained by multiplying the maximum Compton electron energy by a fixed constant. However, that constant can vary for detectors with different scintillators, geometries, as well as photomultiplier tube and electronics. The relationship of certain locations in the pulse height spectrum versus the corresponding electron equivalent energy has been studied for organic scintillation detectors smaller than 3” in length or in diameter according to the literature, but the study for 5” detector used in our measurement was not found. Therefore we have developed a two-dimensional broad-mapping technique to perform the energy calibration by gamma-ray sources. The energy was calibrated from 0.1 MeVee to 1.1 MeVee. For a monoenergetic gamma ray source, the energy at the half-height of the

Compton edge was determined to be 1.085 times the maximum energy of the Compton electrons.

The energy calibrations of electron equivalent energies were carried out at HIMAC during the runs by using a ^{60}Co source respectively for the six liquid scintillation neutron detectors used in the experiments. Then the conversion of MeVee to MeV was conducted using the SCINFUL-QMD code [27], which employs the light output functions for proton, deuteron, triton, ^{3}He and alpha particles from Ref. [28].

As for the TDCs used for the tof measurement, the time calibration can be done by using a time calibrator generating periodic signals. The time calibration results are shown in Table 5 respectively for six TDC channels.

Table 5. Time calibration results for six TDC channels.

Detector number (angle)	TDC calibration (ns/channel)
N1 at 0°	0.2502
N2 at 15°	0.2502
N3 at 30°	0.2490
N4 at 60°	0.2504
N5 at 90°	0.2490
N6 at 121.2°	0.2490

II.3.b Spectra analysis

Trigger plastic

The total counts from the trigger plastic in a single run represents the number of primary ions incident on the target and can be used for normalizing the total number of primary ions among different runs. There is a certain probability that more than one beam particle will hit the trigger plastic within a tiny time window or the resolving time and then cause a pile-up event. If such a signal is fed into a CFD to create a logic signal, the CFD will be fired only once. Because it is not able to distinguish which ions results in the later coincidence event, these pile-up events have to be removed from the data analysis. Only the “good beam” events were selected for the later data analysis. A pulse height spectrum of the trigger plastic for a data run is shown in Figure 13 for illustration.

Sorting the self-time for each neutron detector

In the logic setting for this measurement, as long as any one of the six neutron detectors is in coincidence with the trigger plastic, the coincidence module fires a trigger. Sorting out which neutron detector fire the event trigger relies on the self-time of each detector. The self-time concept can be illustrated by Figure 14. The TDC spectrum on the top of Figure 14 shows the total coincident events registered in the TDC for a data run (In this case it was 230-MeV/nucleon ^{4}He ions incident on the iron target). In such a spectrum, there is no way to figure out which detector contributed the signals that are in coincidence with the TP’s delayed signal. However, by creating the gates of each detector’s self-time and filtering the total spectrum with the self-time gates of each detector (middle of Figure 14), individual spectra for each detector at different angles can be obtained (bottom of Figure 14).

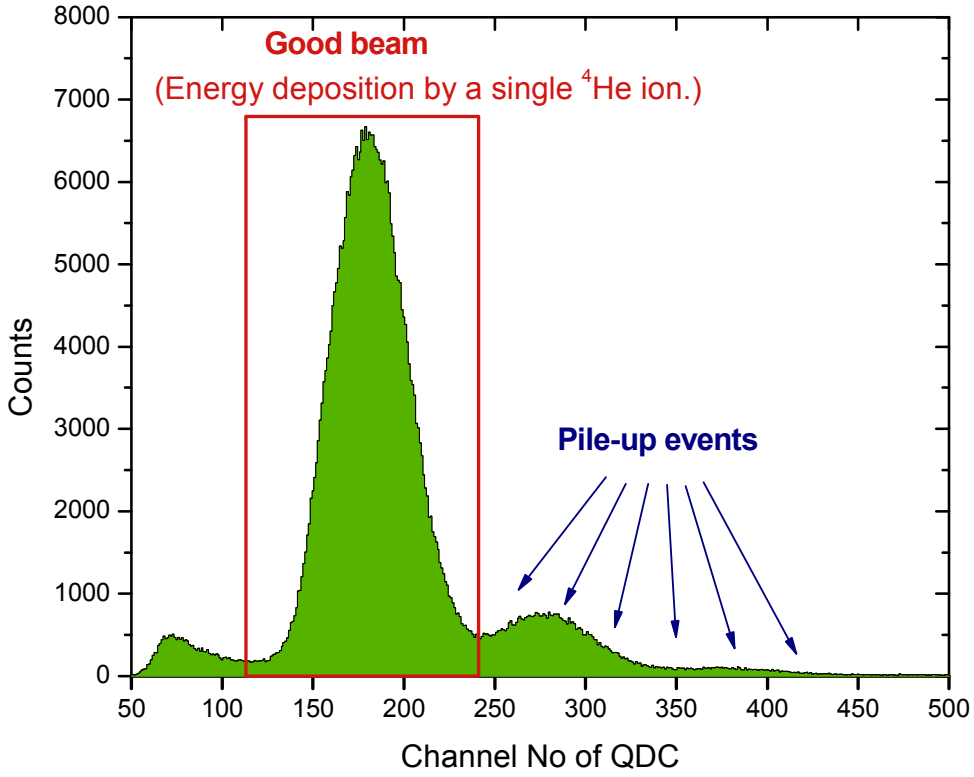

Figure 13. A pulse height spectrum of the trigger plastic for a data run.

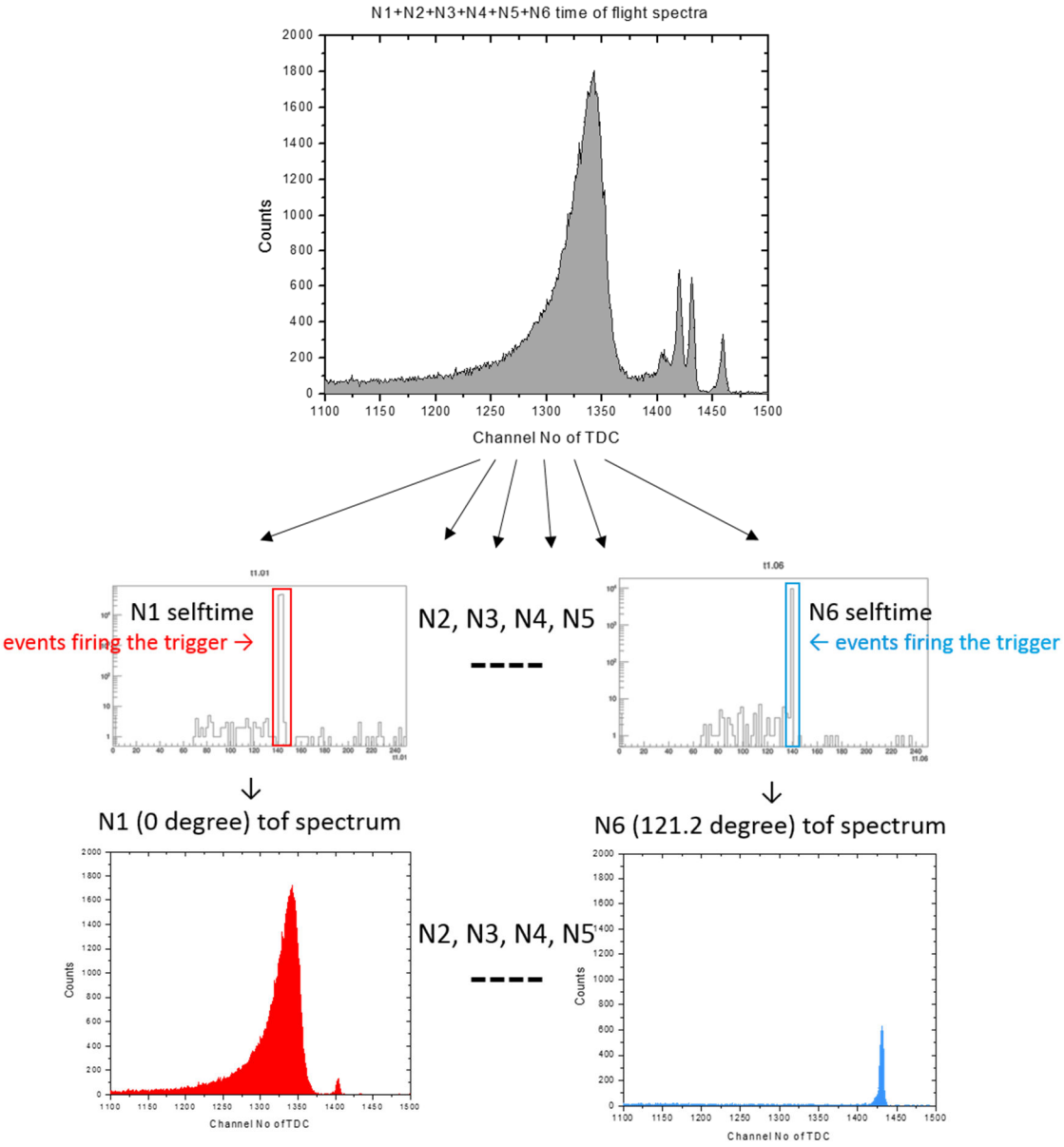

Figure 14. Illustration of the self-time.

E vs. ΔE and ToF vs. E

After sorting out which liquid scintillation detector is in coincidence with the trigger plastic, the next step is to distinguish what species of the secondary particle fired the trigger. In order to do this, two types of plots are utilized. One is the energy deposition in the liquid scintillation detector (E) versus the energy deposition in the veto detector (ΔE), and the other is the energy deposition in the liquid scintillation detector (E) versus the time of flight of each particle (ToF). Figure 15 shows an example of the E vs. ΔE plot. In such plots, neutral particles including neutrons and photons deposit no energy when they pass through the thin veto detector, As a result these particles lie on the very low end of the plot, as indicated by the arrow (these events have non-zero values in the veto detector because they register their "pedestal" values that correspond to the ambient electronic noise that is processed during the event). Regarding the charged particles, since the stopping power is specific to the ion species at certain velocity, different species of charged particles can be separated by combining the information of linear energy transfer to the veto detector and the remaining energy deposited in the liquid scintillator.

Figure 16 is an example of the ToF versus E plot from 100-MeV/nucleon ^{4}He ions stopping in the PMMA target. Prompt gamma rays are produced during nuclear interactions occurring between primary ions and target nuclei; thus the signals created by prompt gamma rays in those events can be used as a time reference showing the ToF for light to travel such a flight path. Considering the rest of the events in the ToF versus E plot, even if different types of particles carry the same kinetic energy, they have different velocity, and thus different flight time to arrive the liquid scintillator, due to their different masses. The resulting separation seen in the ToF versus E plots is how these particles are distinguished. It should be noted that the reversed time-of-flight measurement technique was used in the experiment, i.e. the clock started with the particle generating a signal in the liquid scintillator and stopped with a delayed trigger plastic's signal.

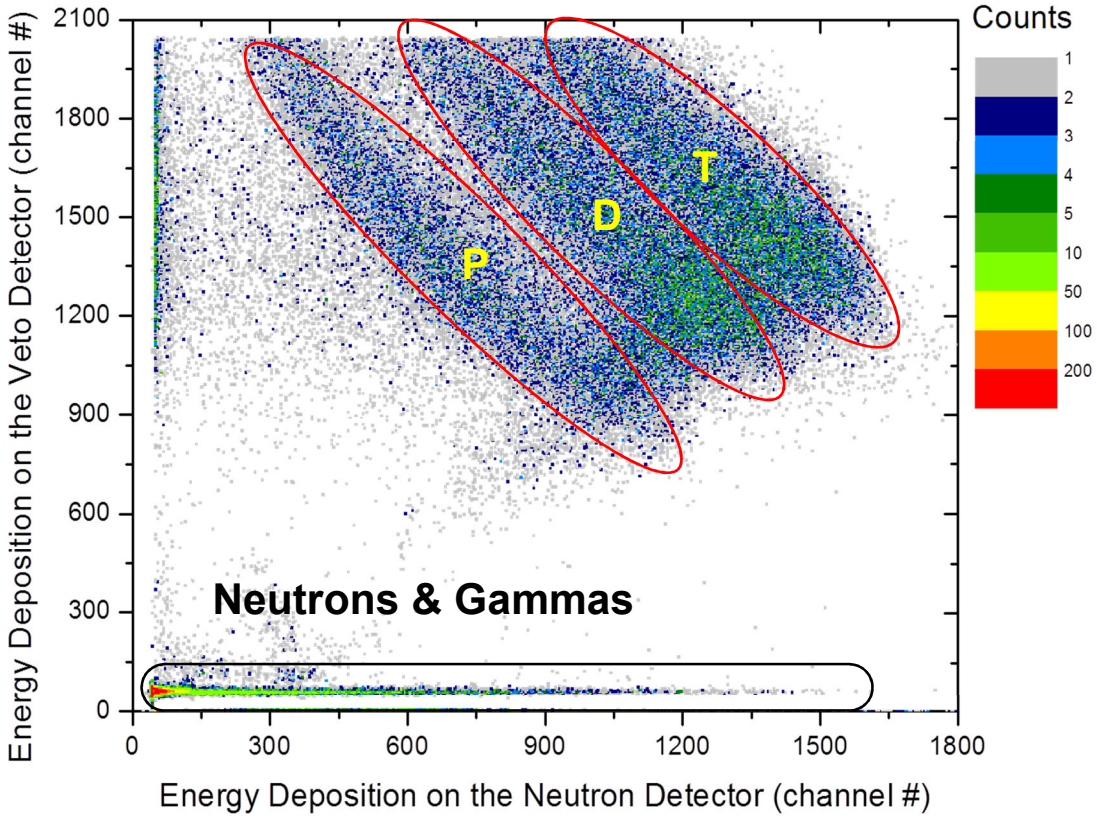

Figure 15. An E vs. ΔE plot measured at 0^0 when 100-MeV/nucleon He stopped in the PMMA target.

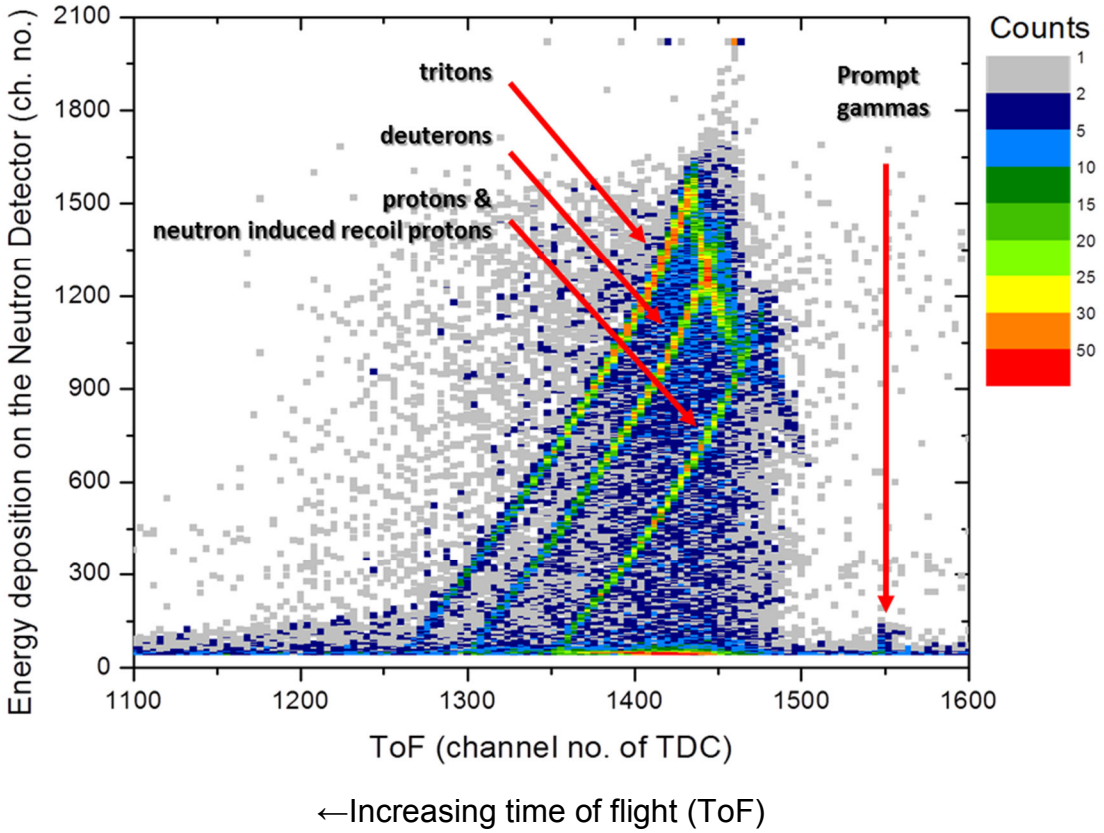

Figure 16. A ToF vs. E plot measured at 0^0 in the system with 100-MeV/nucleon He incident on the PMMA target.

Neutron/gamma discrimination

After separating neutral particles from charged particles, neutrons and gamma rays must be discriminated from each other. The NE213/EJ301 detector used in this experiment is well-known for its capability of neutron/gamma discrimination based on their different pulse shapes. The fraction of the scintillation light that appears in the slow component depends on the species of the exciting particles. Scintillation light created by neutrons (recoil protons) or other heavier charged particles have a larger fraction in the slow component than light created by gamma rays (Compton electrons). Hence, by plotting the Qtot (the pulse charge is totally integrated) versus Qtail (only the slow component of the pulse charge is integrated), neutrons and gamma rays can be separated by pulse shape discrimination, as shown in Figure 17.

Time-of-flight and energy spectra

The time-of flight spectra are composed of various particles, as two examples from the experiment data shown in Figure 18 (a) and (b) that have been filtered by the self-time of each detector. The particle species can be determined by the techniques described above. Once the particle species is selected, the total ToF spectrum can be filtered to a corresponding spectrum for each individual particle species.

The detail of how the ToF is determined is explained by an example shown in Figure 19. This figure shows a part of the TDC spectrum, which contains only neutral particles and was measured at 15° with 230-MeV/nucleon ^{4}He ions stopping in the PMMA target. In this example, the prompt gamma ray peak was centered at Ch. No. 1469.7 with FWHM of 6.06 channels. The time of flight of the prompt gamma rays can be calculated from Equation 6, and it is obtained that Ch. No. 1469.7 corresponds to 13.27 ns. To calculate the time of flight at Ch. x, we can multiply ΔCh (how many channels that Ch. x is away from Ch. 1469.7) by the

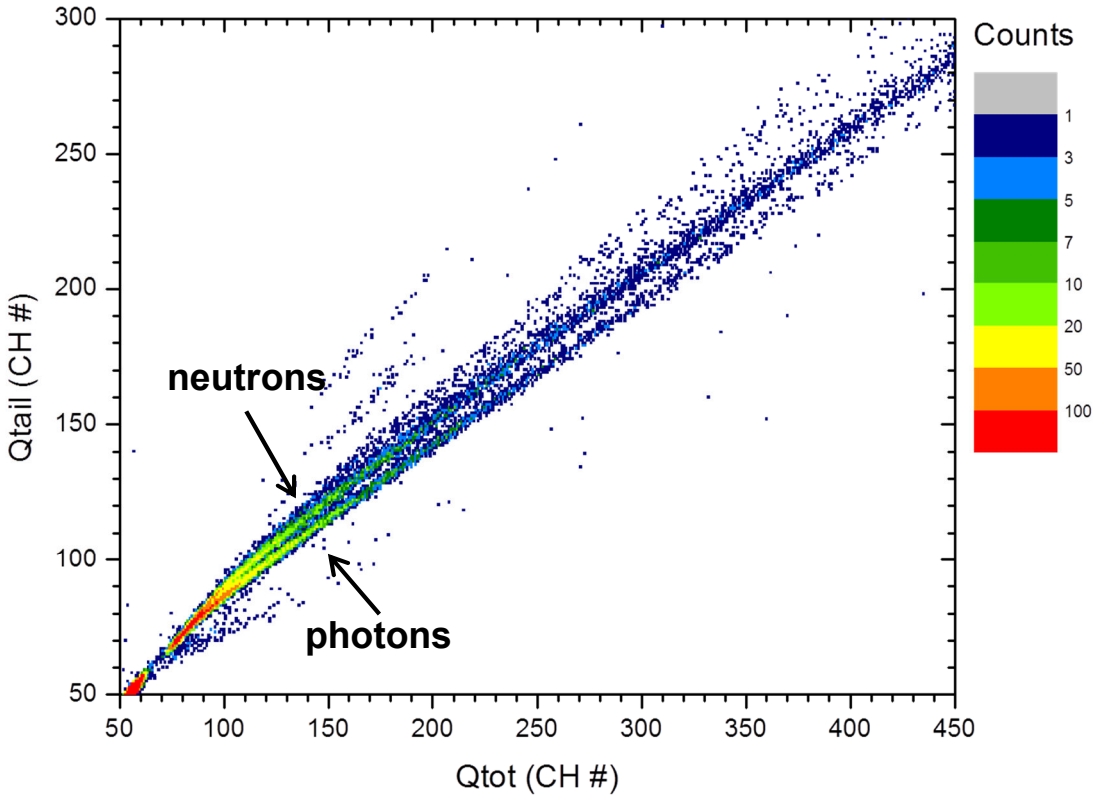

Figure 17. The pulse shape discrimination plot for the 0^0- neutron detector in the 100-MeV/nucleon He projectiles + thick PMMA system.

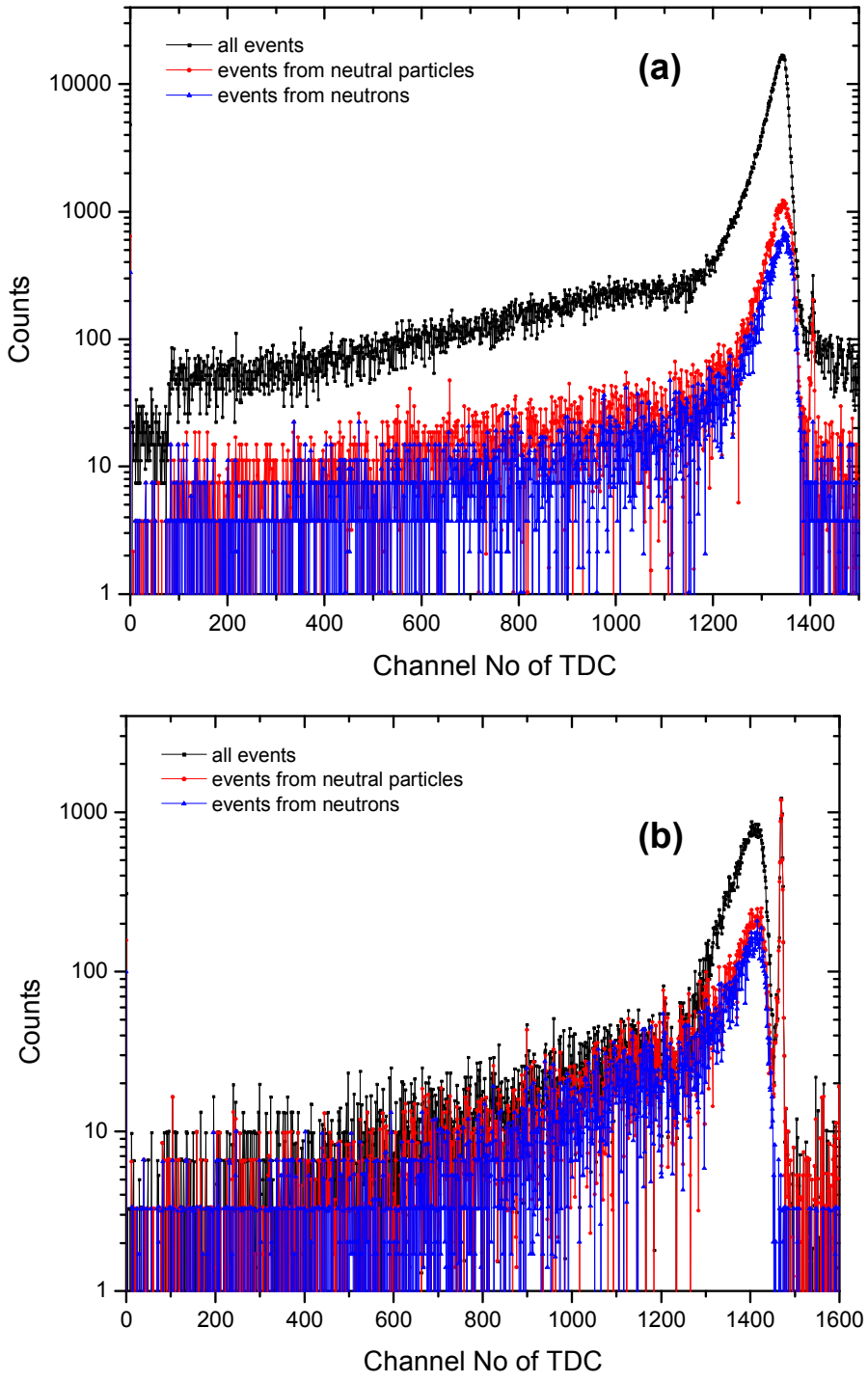

Figure 18. Time-of-flight spectra measured at (a) 0^0 with 230-MeV/nucleon ^{4}He incident on water, and (b) 15^0 with 230-MeV/nucleon ^{4}He incident on iron.

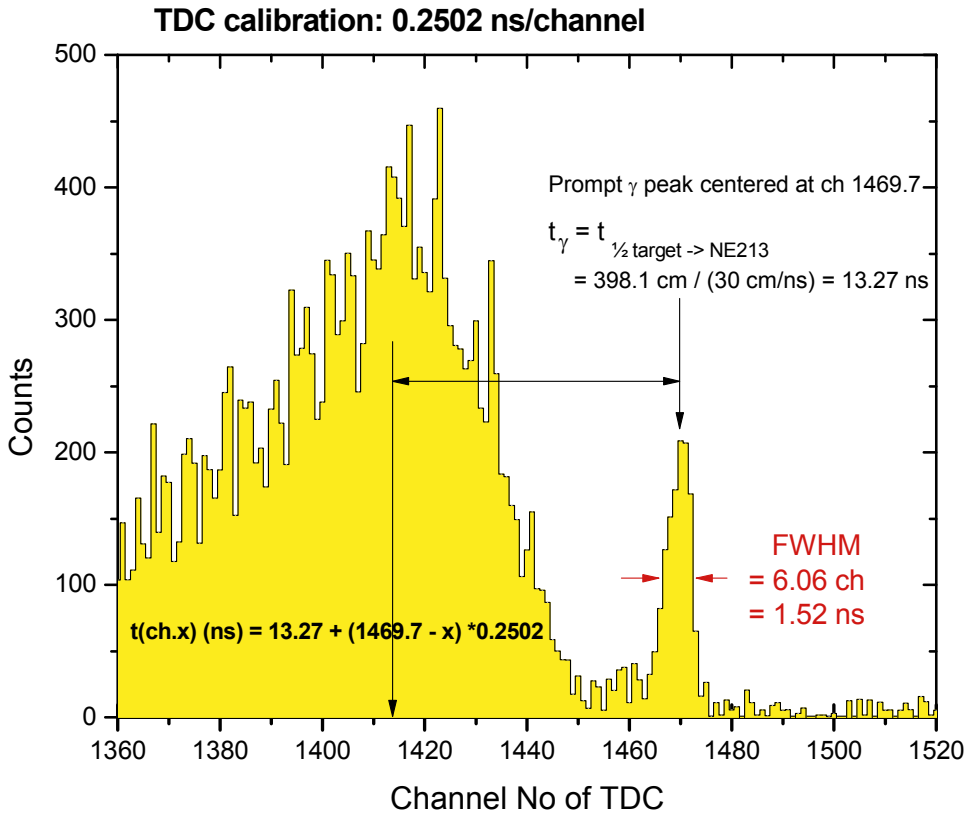

Figure 19. An example of the TDC spectrum containing only neutral particles and measured at 15˚ with 230-MeV/nucleon ^{4}He ions stopping in the PMMA target.

TDC calibration result (0.2502 ns/channel) and then add 13.27 ns. Once the time of flight is converted from the TDC channel number, the neutron energy can be obtained using Equations 1-4 listed in section II.2.b Measurement methods.

II.3.c Background subtraction and Application of Corrections

For each beam-target configuration, measurements were carried out with and without an iron shadow bar in front of the ΔE-E detector set. The measurements with shadow bars were to measure room scattered background particles for the background subtraction, which is especially important for secondary neutrons since neutrons have higher probability than charged particles to scatter a great distance and eventually to strike the detector. After the background subtraction, the statistic error can be obtained by the error propagation from measurement with and without shadow bar.

Other corrections applied to the measured data include the detector efficiency of the neutron detectors and the particle attenuation in the air. The detector efficiency is necessary information for normalization of all spectra including the angular distributions of the secondary neutrons. The neutron detection efficiency of a neutron detector can be calculated by SCINFUL-QMD code [27], a Monte Carlo based computer code that can calculate the response function and detection efficiency of a liquid organic scintillator for neutron energies from 0.1 MeV up to 3 GeV. This code simulates the scintillator response not only for neutron induced recoil protons and carbon ions but also for nuclear fragments created by incident neutrons within the detector volume.

For benchmark comparison of double-differential spectra of secondary particles, there are two common methods described in the literature. One is to compare the raw measurement results, and the other is to compare the corrected measurement results. In the former scenario, the experimental setup, including the environment, detector geometry, the room scattered background etc., is

considered in a Monte Carlo simulation, and the Monte Carlo code simply simulate the measurement. Thus there is no need to determine the detector efficiency and to correct the attenuation in air for the measurement results. Though this type of comparison can avoid some errors introduced from the application of these correction to the measured data, the experimental data are not universal if the experiment is performed at a different facility or when using a different experimental setup. In contrast, in the later scenario, the corrected data for a beam-target configuration is compared; such data will not and should not be changed even if the facilities and the measurement methods are different, but the disadvantage is the additional uncertainty associated with the corrections. Here, the corrected measured data were selected to be compared with the Monte Carlo simulations.

II.4 Benchmark calculations

The comparison of the experiment data with the model calculations was done as described in the section II.3.c Background subtraction and Application of Corrections. Three Monte Carlo simulation codes PHITS, FLUKA, and MCNP with their default physics models were selected for benchmarking. The physics models employed in each code as well as the geometry setup are described below.

II.4.a Monte Carlo codes and its physics models

PHITS

The PHITS code version 2.73, which was the latest version at the time when calculations performed, was utilized for model calculations. The cut-off energies of particle transport were 0.01 MeV for protons, 0.1 MeV for neutrons, electrons, positrons and photons, and 0.1 MeV/nucleon for nuclei equal or heavier than deuterons.

The default physics models implemented in PHITS can be referred to Figure 20 [29]. The neutron transport is based on the nuclear data library JENDL-4.0 for energies below 20 MeV and switched to physics models for energies above 20 MeV. The INCL 4.6 (Intra-Nuclear Cascade of Liège) model [23] is used for simulating the dynamic stage of nucleons (proton and neutron), pions, and light ions (^{2}H, ^{3}H, ^{3}He and alpha) induced reactions in the intermediate energy region. This model is recommended as the default because it can deal with light-hadron induced reactions much faster than JQMD and it also includes a coalesce model. The evaporation and fission model GEM is adopted for simulating the static stage for both hadron- and nucleus-induced reactions.

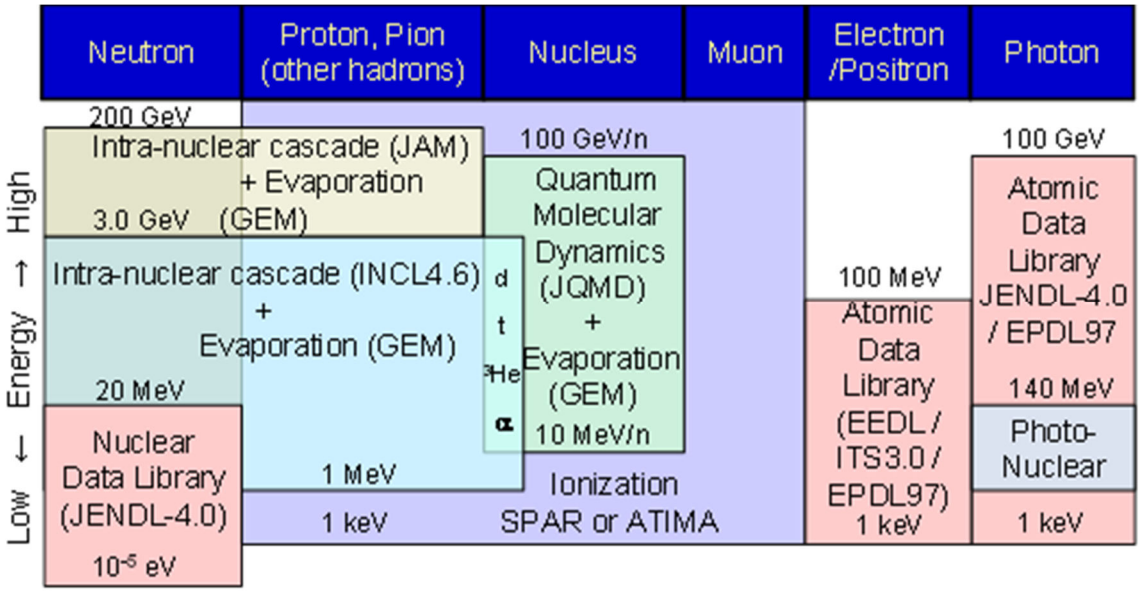

Figure 20. The default physics models employed in PHITS [29].

Most of the physics models or settings employed for this benchmark calculation are defaults. However, few setting were revised and listed below. i) The energy loss of charged particles, except electrons, was calculated by codes SPAR for nucleus and NMTC for the other particles with the continuous slowing down approximation. ii) The energy straggling for charged particles and nucleus was considered. iii) Gamma decay for residual nuclei was included in the simulation.

FLUKA

FLUKA code [12] is a general purpose Monte Carlo code for calculating the transport and interaction of hadrons, heavy ions, and electromagnetic particles in various materials, covering the energy range from few keV (or thermal energies for neutrons) to Cosmic Ray energies (several TeV/nucleon). The code is jointly developed and maintained by the European Laboratory for Particle Physics (CERN) and the Italian National Institute for Nuclear Physics (INFN). It is widely used for proton and electron accelerator shielding to target design, calorimetry, activation, dosimetry, detector design, Accelerator Driven Systems, cosmic rays, neutrino physics, and radiotherapy. The latest version 2011.2c was used for this benchmark calculation.

The PRECISIOn defaults declarations were chosen. For neutrons with energies lower than 20 MeV, FLUKA uses its neutron cross section library with 260 energy groups. Hadron-nucleon inelastic collisions in FLUKA are modeled based on resonance production and decay below a few GeV.

Regarding the hadron-nucleus (h-A) interactions modelled in FLUKA, they can be schematically divided to a sequence of the following steps:

- High energy collisions and intranuclear cascade
- Pre-equilibrium emission
- Evaporation/fragmentation/fission and gamma de-excitation

At momenta below 3-5 GeV/c, the Generalized IntraNuclear Cascade (GINC) model implemented in the PEANUT (PreEquilibrium-Approach-to-NuclearThermalization) package is used for hadron-nucleus interactions. This IntraNuclear Cascade mechanism describes h-A reactions as a cascade of two-body interactions, concerning the projectile and the reaction products. Also in the PEANUT, the GINC is transited to a pre-equilibrium stage and then equilibrium processes: evaporation, fission, Fermi break-up, gamma de-excitation.

Nuclear interactions generated by heavy ions (nucleus-nucleus interactions) are treated through an event generator coupling the modified Relativistic Quantum Molecular Dynamics (RQMD) model for energies between 125 to 5000 MeV/nucleon, and the Boltzmann Master Equation (BME) theory for energies below 125 MeV/nucleon. After the cascade stage of the interaction, the excited pre-fragments are passed to the evaporation/fragmentation models of FLUKA, which emit low energy nucleons and fragments in the pre-fragment center-of-mass. For light nuclei (A<16), the evaporation/fission stage is replaced by Fermi break-up. At the end of the reaction stage, gamma de-excitation is performed when particle emission is no longer energetically possible

MCNP

MCNP [13] is a general-purpose Monte Carlo N-Particle code that is capable of tracking 34 particle types (nucleons and light ions) and over 2000 heavy ions over a broad energy range. It is developed by the Los Alamos National Laboratory (LANL). The version of MCNP used for this benchmark calculation is MCNP6 version 1.0.

For transport of neutrons and protons with energies below 150 MeV, tabulated cross section data are used. For the calculation of the first rapid phase of nuclear reaction, MCNP6 uses the latest version of the cascade-exciton model (CEM) as incorporated in its event generator CEM03.03 [30] to simulate

fragmentation reactions induced by nucleons, pions, and photons at incident energies up to 940 MeV/nucleon, and nuclear reactions induced by deuterons, tritons, ^{3}He, ^{4}He, and antinucleons are handled by ISABEL INC model at energies up to 940 MeV/nucleon. Both of CEM03.03 and ISABEL INC assume that the reactions occur schematically in three stages: IntraNuclear Cascade (INC), followed by pre-equilibrium emission of particles during the equilibration of the excited residual nuclei formed after the INC (the preequilibrium reactions are optional), followed by the equilibrium evaporation/fission of the compound nuclei, as shown in Figure 21 [32]. More details of CEM03.03 can be found in Ref. [32].

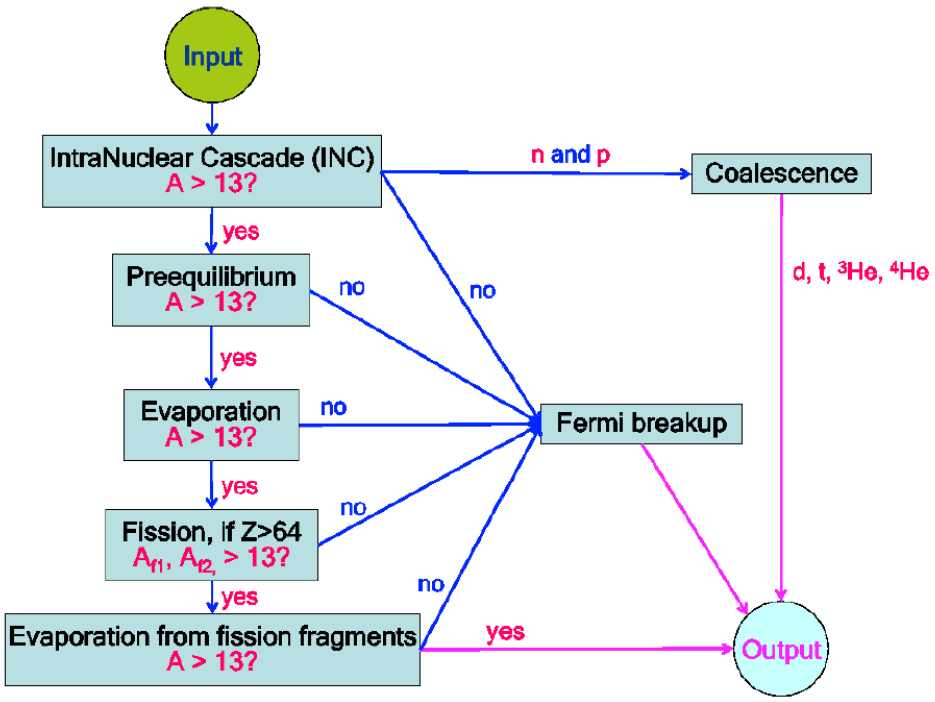

Figure 21. The Flow chart of nuclear reactions calculated by the CEM03.03 and LAQGSM03.03 [32].

For the calculation of the second slow phase of nuclear reaction, Dresner and GEM2 models were used in this study in MCNP6. Dresner evaporation model with Rutherford Appleton Laboratory (RAL) fission is invoked with ISABEL by default, and the evaporation and fission followed by the INC in CEM03.03 is handled by a modification of the Generalized Evaporation/Fission Model, GEM2, by default.

Also, the number of types of particles to be considered at the evaporation stage can be user-defined in MCNP6. The default value for this number used in CEM03.03 and LAQGSM03.03 is 66; however it was declared to be 6 considering fragments lighter than ^{4}He (n, p, d, t, ^{3}He, and ^{4}He) to save computing time in this benchmark calculation.

II.4.b Geometry setup

The simulation geometry is illustrated by Figure 22. A monoenergetic and monodirectional ^{4}He ion beam with 1 cm diameter impinged on the stopping target located at the center of the sphere. Six ring-type detectors on a spherical surface, which have equivalent angles with the experimental setup (0^{0}, 15^{0}, 30^{0}, 60^{0}, 90^{0}, and 117.5^{0} (for the 100-MeV/nucleon ^{4}He system) or 121.2^{0} (for the 230-MeV/nucleon ^{4}He system)), were setup to score secondary neutrons. The volume of the cavity delimited by the sphere was assumed to be void since the attenuation of neutron fluence in air has been corrected for the measured data.

The particle fluence was scored by means of inverse cosine-weighted boundary crossing estimators (i.e. fluence across a surface) at the boundaries of the ring-type detectors. The radius of the sphere setup in the FLUKA and MCNP simulations was 50 cm, and the radii of the spheres in the PHITS geometry were the same as the flight paths for each detectors in the experiment (501.9 cm, 398.1 cm, 402.1 cm, 353.0 cm, 301.6 cm, and 261.1 cm respectively for 0°, 15°, 30°, 60°, 90°, and 121.2°.

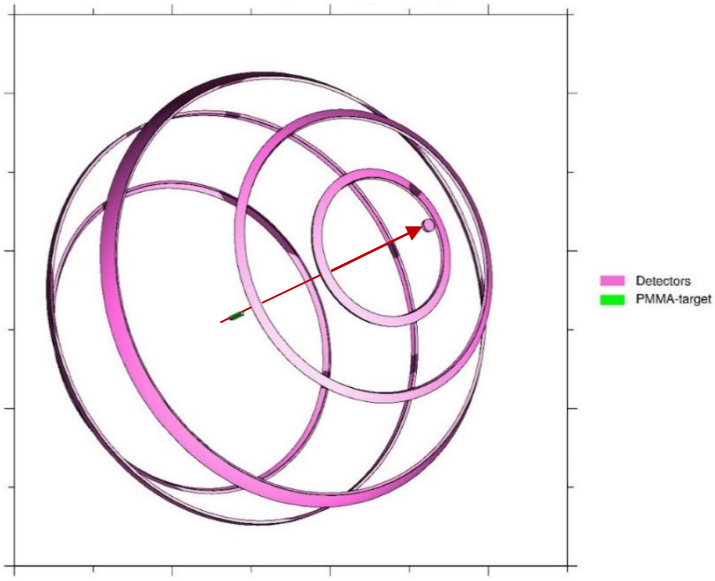

Figure 22. The geometry setup used in PHITS for 230-MeV/nucleon ^{4}He ions stopped in the thick PMMA target.

II.5 Measurement and simulation results

The double-differential thick-target neutron yields (TTY) from the 100- and 230-MeV/nucleon ^{4}He bombarding three stopping targets are shown in Figure 23 through Figure 28 along with the simulation results. In order to display and compare spectra at all measured angles in a common plot for a beam/target combination, the energy spectra were multiplied by different offset factors for each angle. The measurement data are shown in points, and the FLUKA, MCNP, and PHITS simulation results are respectively drawn in solid, dash, and dot lines.

II.5.a Uncertainties of the data and correction applied to the data

The uncertainties of the measured data were comprised of statistical errors and systematic uncertainties. The statistical errors in the TTY spectra were less than 10% for each energy bin for energies below the high-energy peak or the

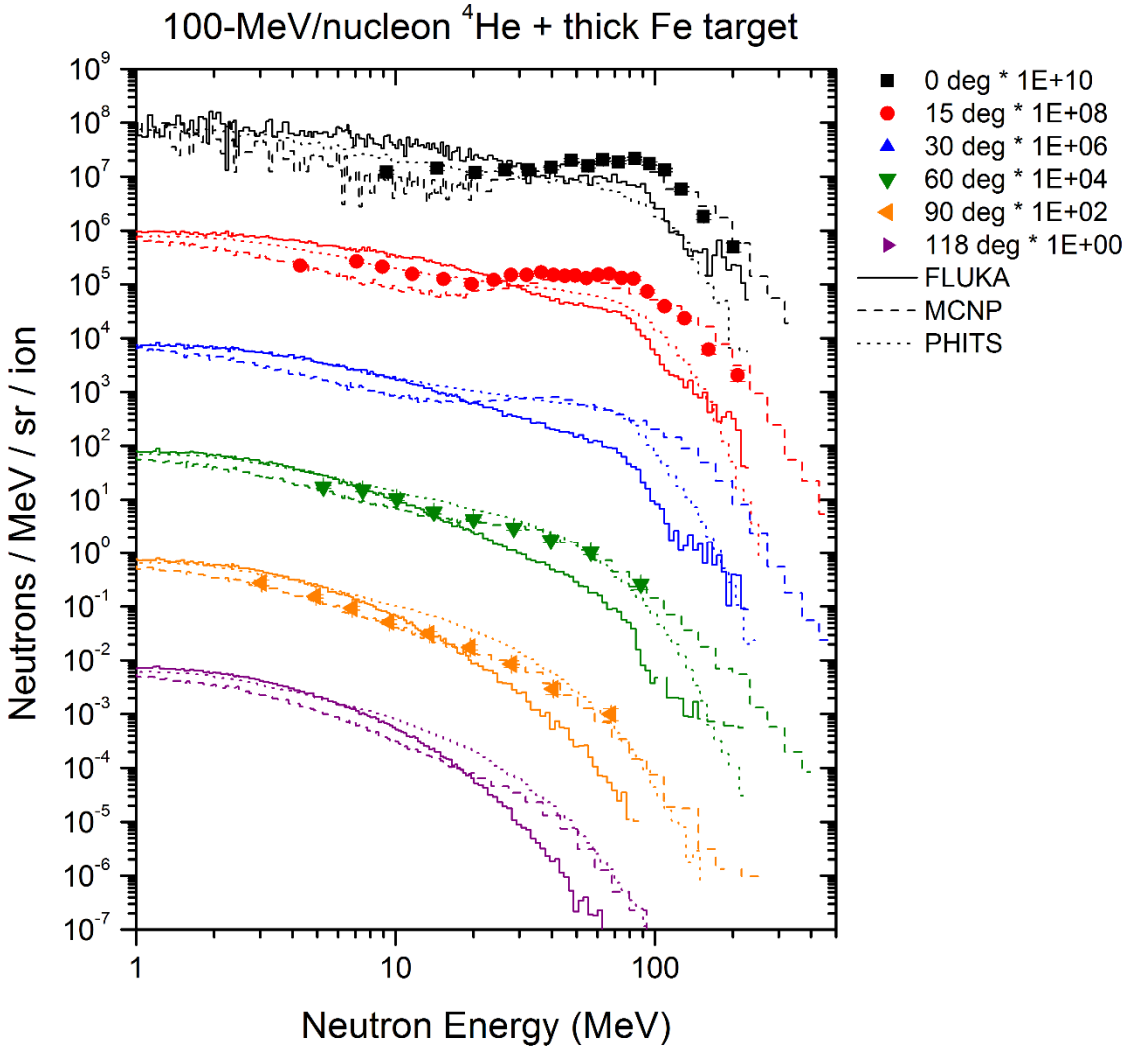

Figure 23. The double-differential thick-target neutron yields from 100 MeV/nucleon ^{4}He stopping in the iron target.

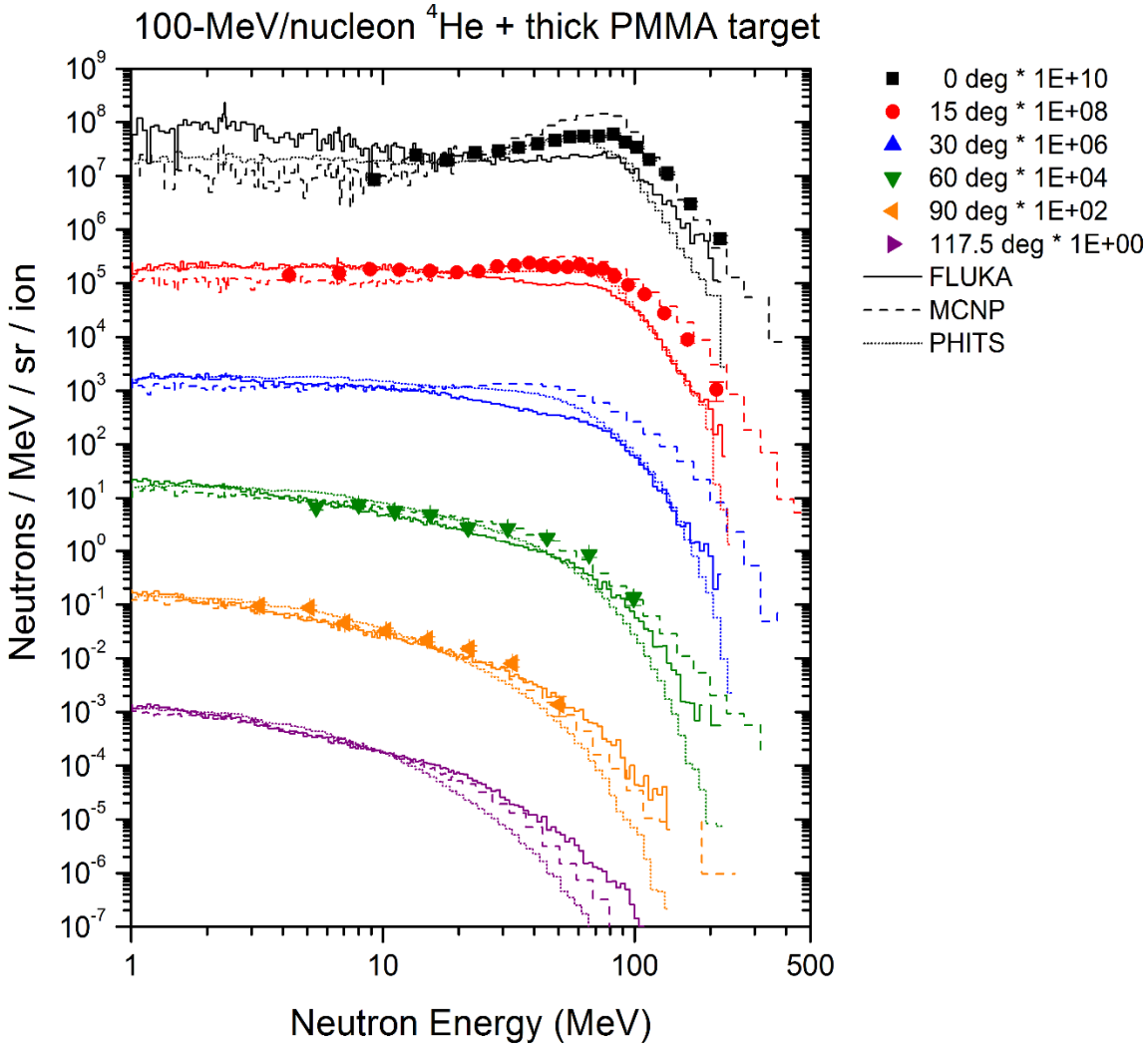

Figure 24. The double-differential thick-target neutron yields from 100 MeV/nucleon ^{4}He stopping in the PMMA target.

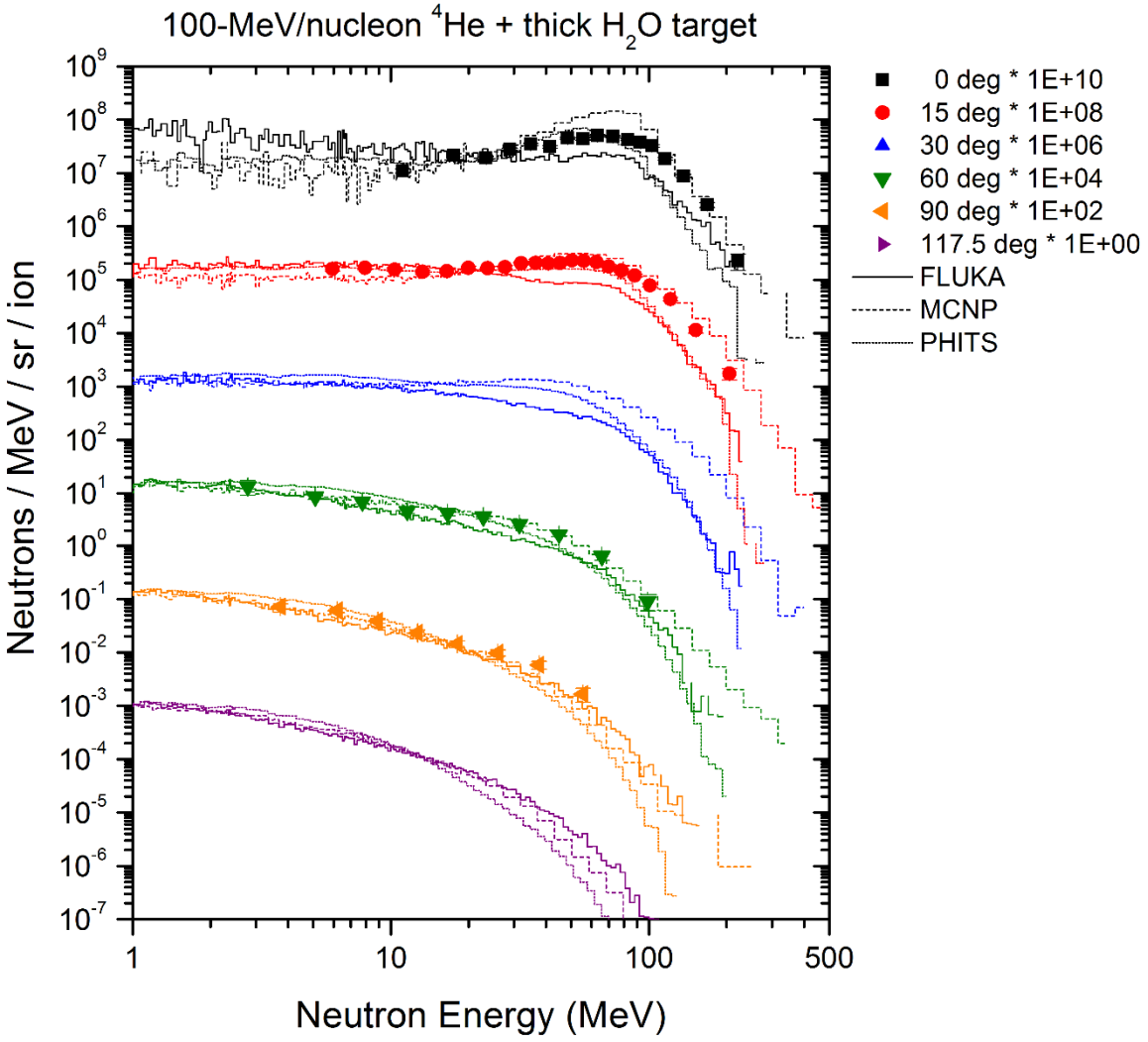

Figure 25. The double-differential thick-target neutron yields from 100 MeV/nucleon ^{4}He stopping in the water target.

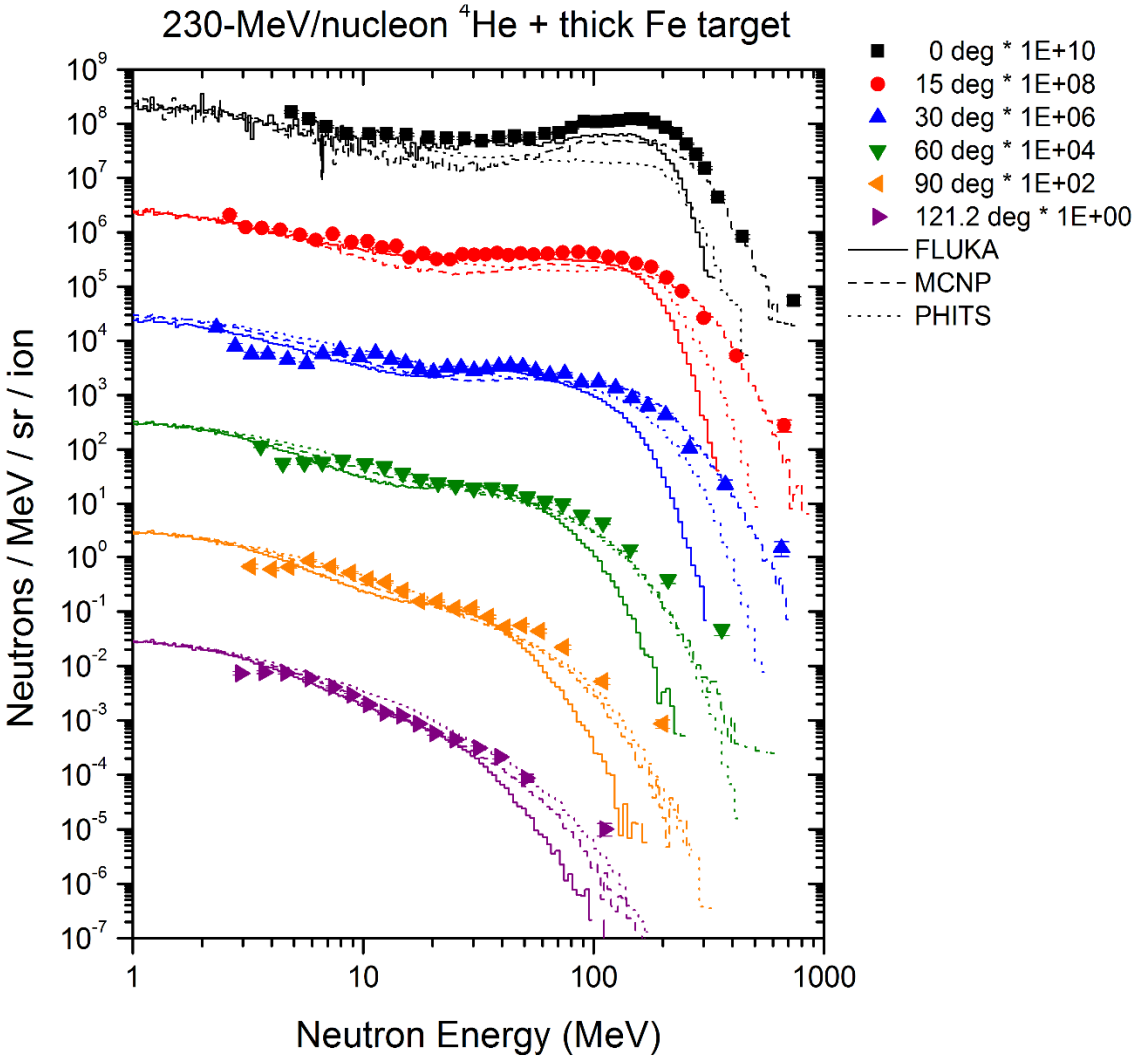

Figure 26. The double-differential thick-target neutron yields from 230 MeV/nucleon ^{4}He stopping in the iron target.

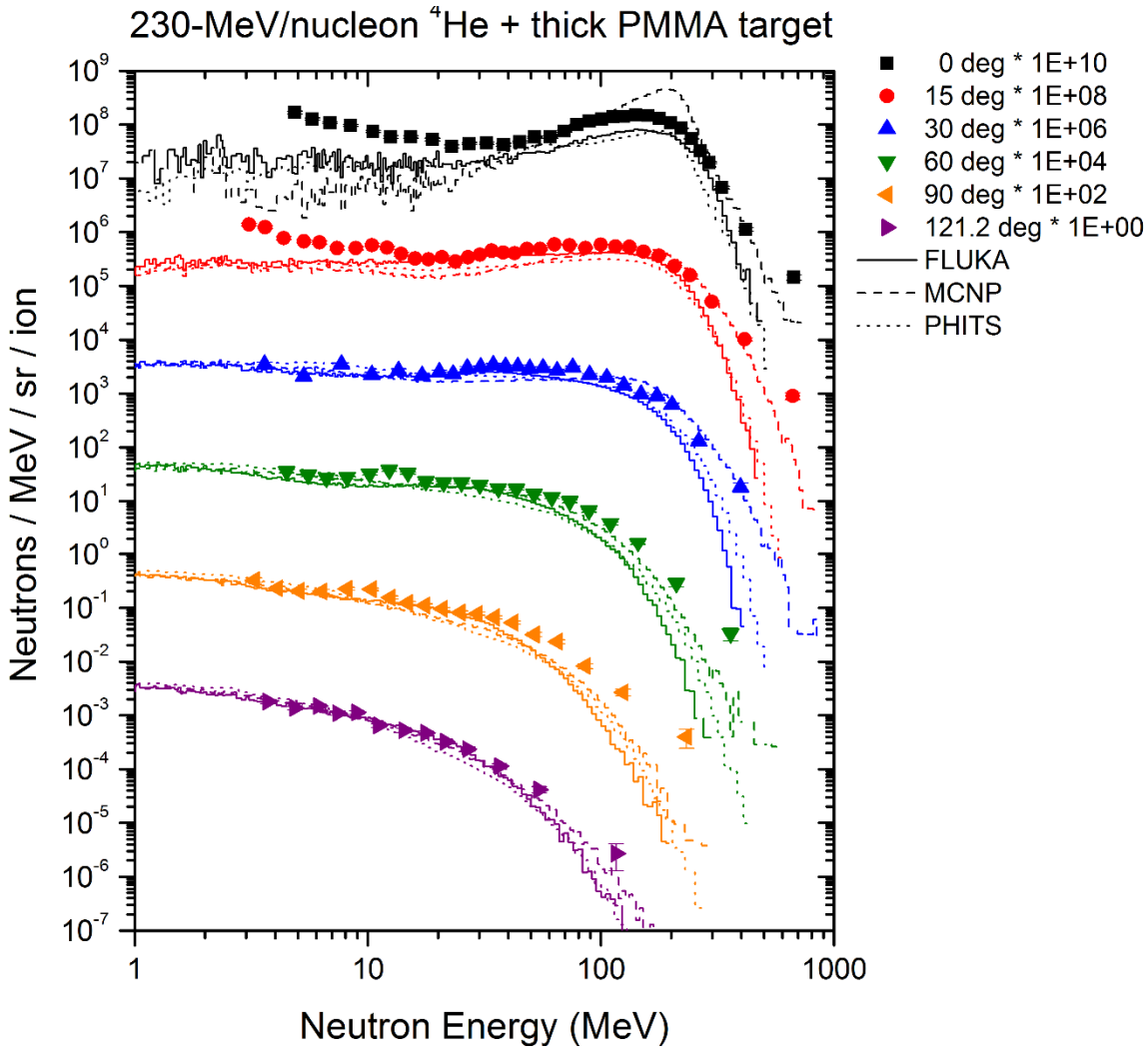

Figure 27. The double-differential thick-target neutron yields from 230 MeV/nucleon ^{4}He stopping in the PMMA target.

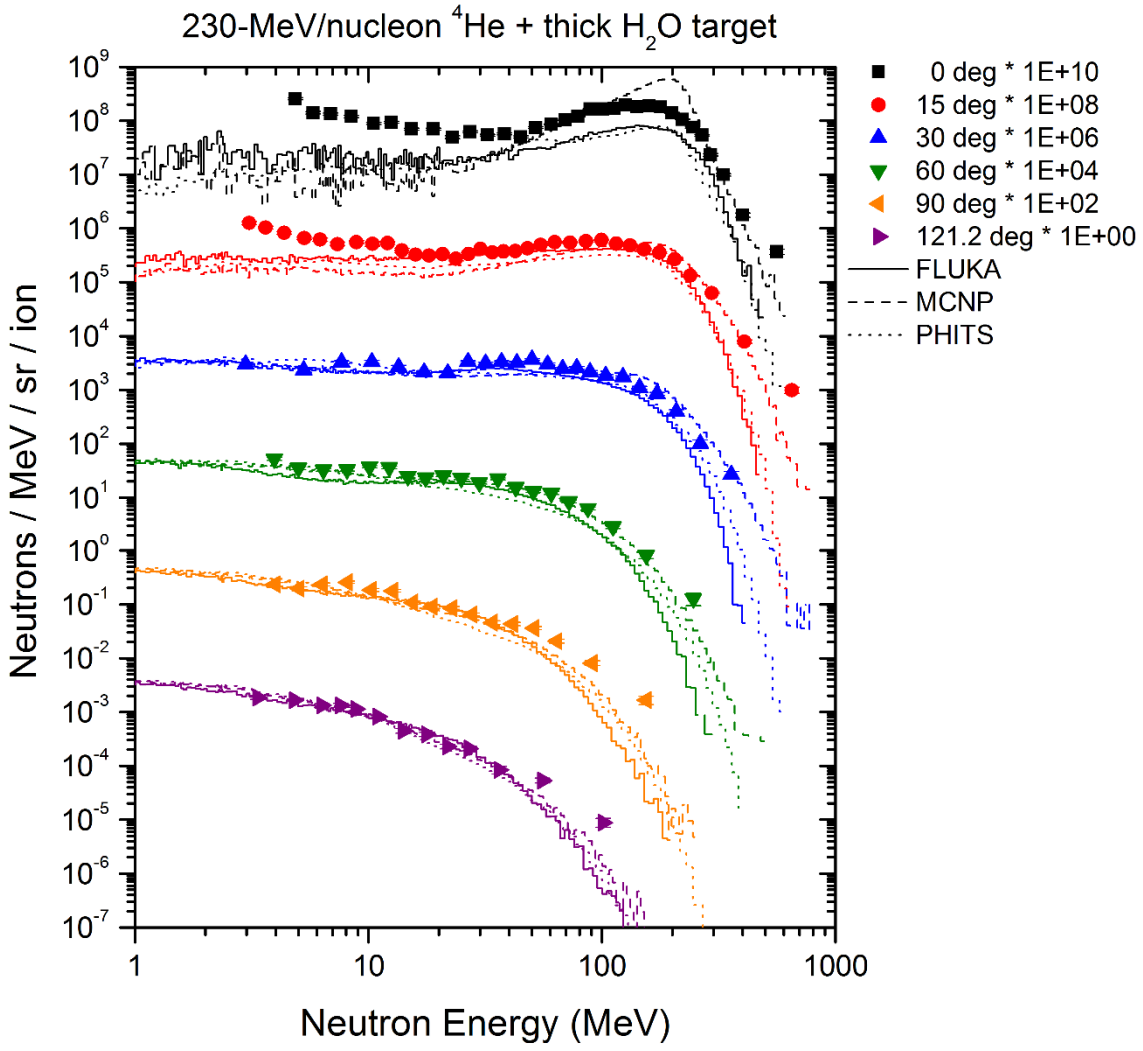

Figure 28. The double-differential thick-target neutron yields from 230 MeV/nucleon ^{4}He stopping in the water target.

shoulder in the spectra, and increased to 20-40% towards the highest energies of each spectrum at each angle.

The systematic uncertainties include the uncertainties from normalization (number of beam particles and solid angles) and uncertainties from the calculated detector efficiency.

The uncertainty in solid angle acceptance due to the target and detector size as well as the assumption of where the reaction occurred (target center) was estimated by 1) assuming different locations of where the reaction occurred in the target (at the front surface or at the primary ion range), and 2) assuming different locations of where the signal was created in the neutron detector (at the front surface or at the bottom). The results shown that the uncertainty in solid angle was less than 10%.

The statistical uncertainties for the number of beam particles can be neglected (< 0.01%). The uncertainty in the calculation of the neutron detector efficiency using SCINFUL-QMD was estimated to be about 10% based on the previous studies [15, 27].

The non-attenuated neutron fluence rates after passing through a certain distance and a thin plastic scintillator are shown in Figure 29. The corresponding attenuation correction factors have been applied to the measured data. Though the attenuation for neutron fluence are energy and distance dependent, the overall corrections were less than 10%.

The statistical errors of the simulation results were also energy and angle dependent. Figure 30 shows a represented plot for the relative statistical errors from FLUKA, MCNP, and PHITS calculations. The statistical errors were generally less than 1% in the energy range below the beam energy (MeV/nucleon), but the 0° errors were slightly higher due to the smaller solid angle of the ring detector setup in the simulations.

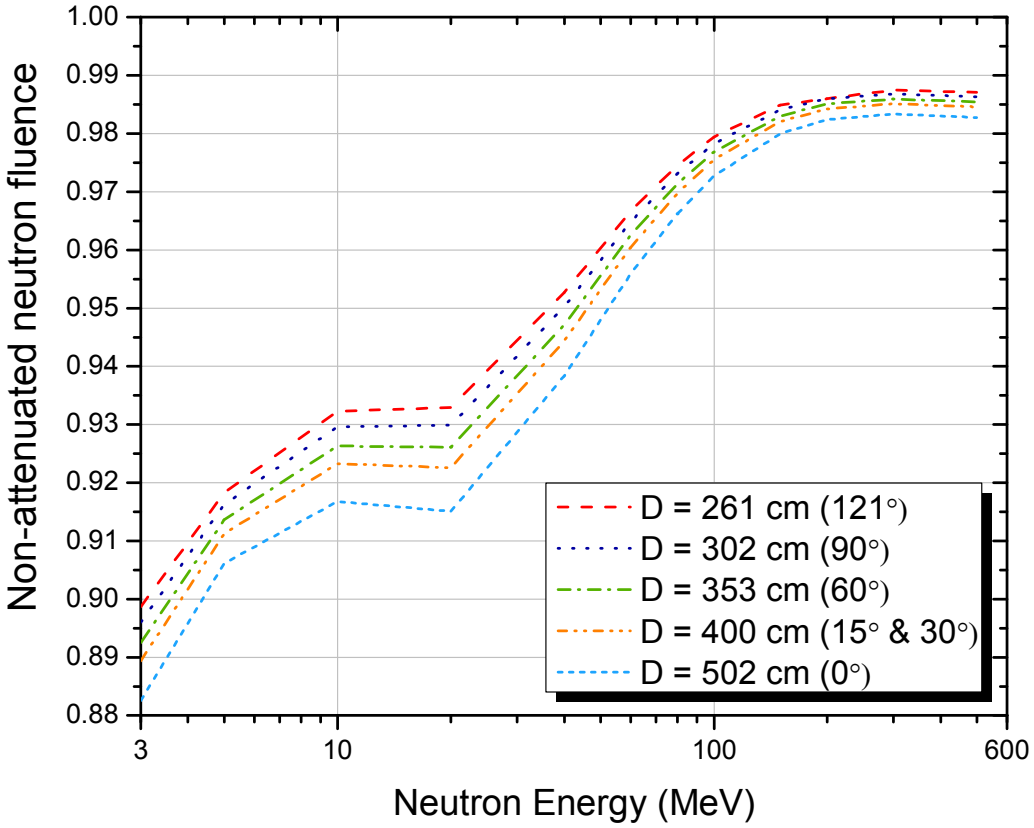

Figure 29. The energy- and distance- dependence attenuation corrections.

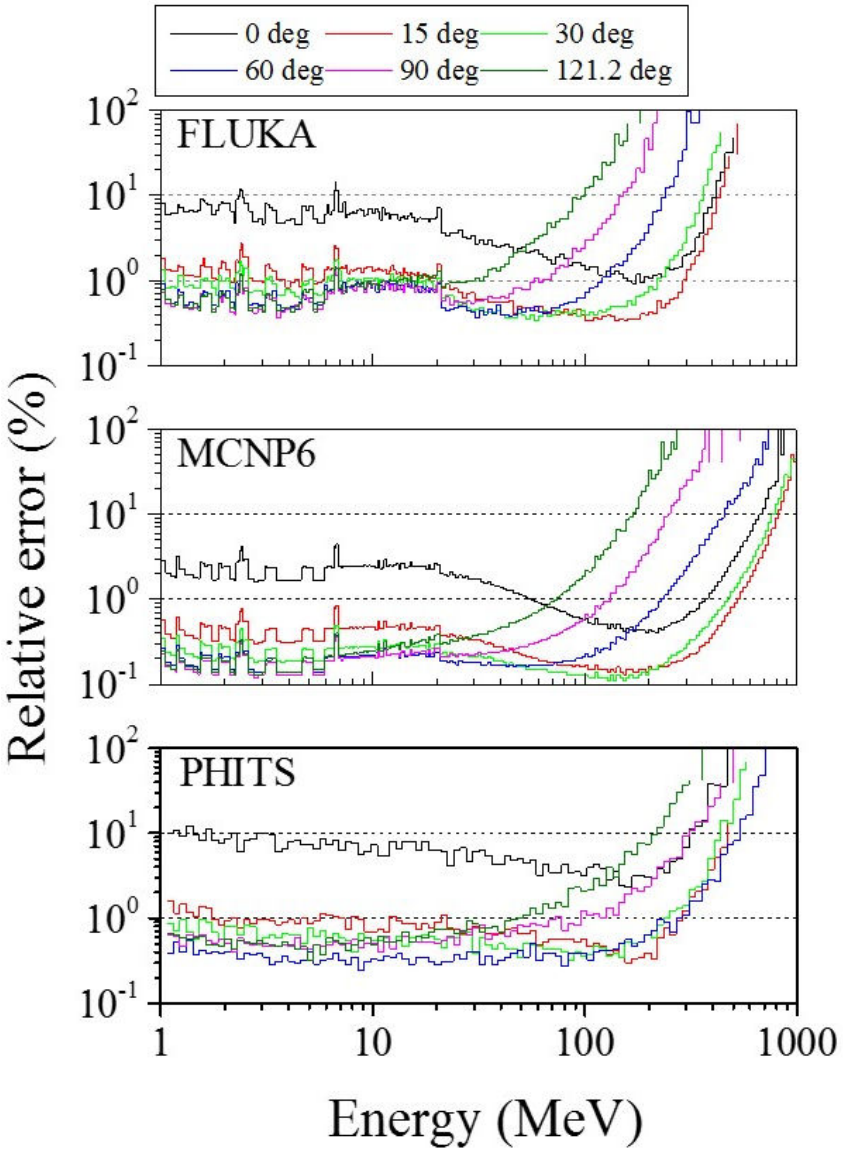

Figure 30. The relative statistical errors in the simulation results from FLUKA, MCNP, and PHITS for 230 MeV/nucleon ^{4}He stopping in the iron target.

In summary, the total systematic uncertainties due to the earlier-described factor were no more than 30%. Also, in the TTY spectra from Figure 23 through Figure 28, only the statistical errors of the measured data are shown in the plots to avoid dramatic drops along the log scale.

II.5.b Energy resolutions of the measurements

As mentioned in section II.2.b Measurement methods, the energy resolution $dT\ (in\ unit\ of\ MeV)$ of the measured spectra is dependent on the time resolution $dt\ (in\ unit\ of\ ns)$ of the time-of-flight measurement, if the uncertainty of the flight path is neglected. In addition, the time resolution dt is taken from the observed FWHM of the prompt gamma ray peak in the ToF spectra for each system. The centroids and the FWHMs of the measured prompt gamma ray peaks for each system are listed in Table 6 for 100 MeV/nucleon ^{4}He projectiles and in Table 7 for 230 MeV/nucleon ^{4}He projectiles.

Table 6. Centroids and FWHMs of the prompt γ ray peaks for each system with 100 MeV/nucleon He projectiles.

Detector (Angle)	Iron target		PMMA target		Water target		Average over the three targets	
	Centroid of the prompt γ ray peak	FWHM of the prompt γ ray peak	Centroid of the prompt γ ray peak	FWHM of the prompt γ ray peak	Centroid of the prompt γ ray peak	FWHM of the prompt γ ray peak	Centroid of the prompt γ ray peak	FWHM of the prompt γ ray peak
	Ch. No.	ns	Ch. No.	ns	Ch. No.	ns	Ch. No.	ns
N1 (0°)	1552.8	1.42	1553.1	1.88	1552.8	1.19	1552.9 ± 0.21	1.50 ± 0.35
N2 (15°)	1618.2	1.29	1617.8	0.86	1618.1	1.04	1618.0 ± 0.22	1.06 ± 0.22
N4 (60°)	1559.0	1.32	1559.2	1.08	1559.3	1.12	1559.2 ± 0.14	1.17 ± 0.13
N5 (90°)	1570.0	1.44	1570.2	1.27	1569.9	1.25	1570.0 ± 0.17	1.32 ± 0.11

Table 7. Centroids and FWHMs of the prompt γ ray peaks for each system with 230 MeV/nucleon He projectiles.

Detector (Angle)	Iron target		PMMA target		Water target		Average over the three targets	
	Centroid of the prompt γ ray peak	FWHM of the prompt γ ray peak	Centroid of the prompt γ ray peak	FWHM of the prompt γ ray peak	Centroid of the prompt γ ray peak	FWHM of the prompt γ ray peak	Centroid of the prompt γ ray peak	FWHM of the prompt γ ray peak
	Ch. No.	ns	Ch. No.	ns	Ch. No.	ns	Ch. No.	ns
N1 (0°)	1404.2	1.36	1405.7	1.43	1405.6	1.19	1405.2 ± 0.81	1.33 ± 0.12
N2 (15°)	1469.5	1.17	1469.7	1.52	1470.0	1.58	1469.7 ± 0.22	1.42 ± 0.22
N3 (30°)	1459.5	1.26	1459.1	1.64	1460.2	1.47	1459.6 ± 0.54	1.45 ± 0.19
N4 (60°)	1409.4	1.25	1409.5	1.25	1410.5	1.88	1409.8 ± 0.61	1.46 ± 0.36
N5 (90°)	1420.4	1.60	1420.7	2.09	1421.4	2.19	1420.8 ± 0.52	1.96 ± 0.31
N6 (121°)	1431.8	1.65	1431.3	2.54	1432.7	2.85	1431.9 ± 0.72	2.35 ± 0.62

The FWHMs of the prompt gamma ray peaks shown in Table 6 are between 0.86 ns and 1.88 ns for systems with 100 MeV/nucleon ^{4}He ions, and the FWHMs listed in Table 7 range from 1.17 ns to 2.85 ns for systems with 230 MeV/nucleon ^{4}He ions.

Also recalled that a better energy resolution can be achieved by longer flight path for the time-of-flight measurement. Figure 31 and Figure 32 show the absolute and relative energy resolutions respectively for two extreme conditions in the experiment. For Figure 31, the N1 (0°) detector had the longest flight path 501.9 cm among all detectors, and the time resolution is assumed the averaged time resolutions over the 230-MeV/nucleon ^{4}He data runs for three targets. In contrast, Figure 32 shows the absolute and relative energy resolutions of the N6 (121°) detector which had the shortest flight path, 261.1 cm, among all detectors, and the time resolution is also assumed the average number over the systems with 230-

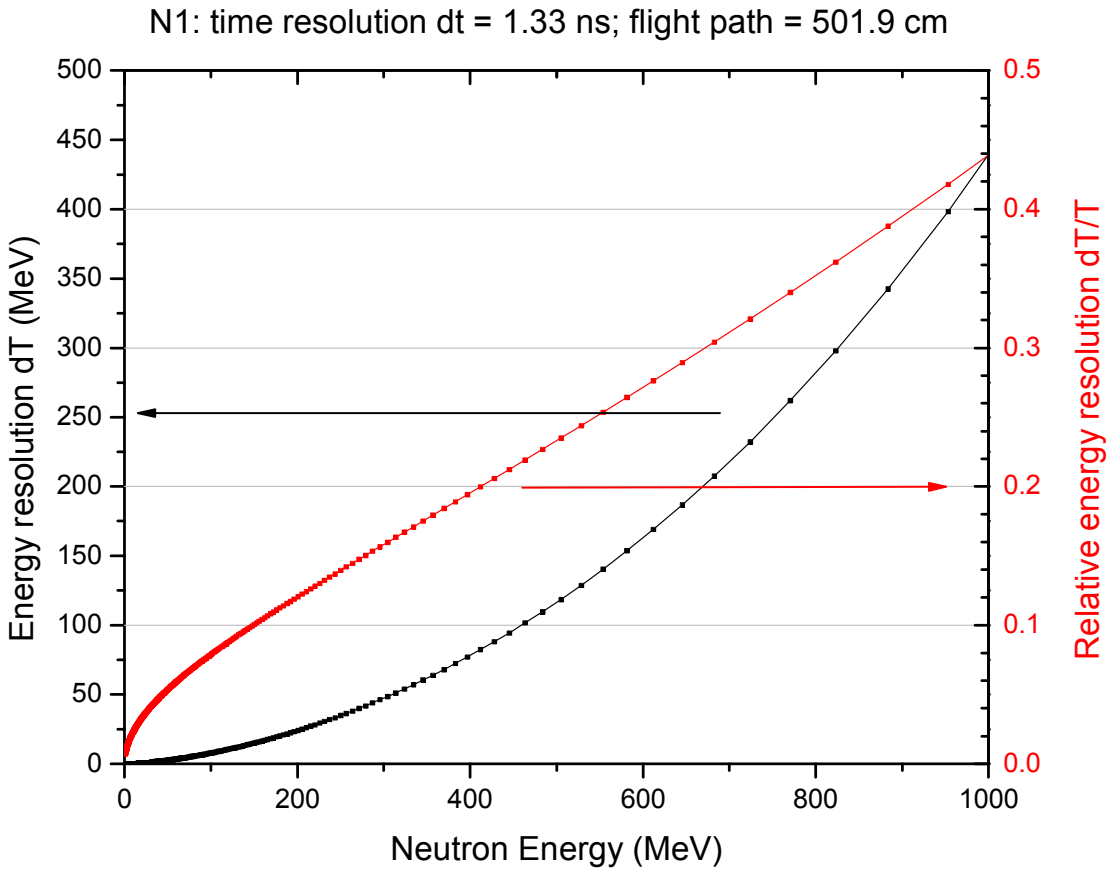

Figure 31. The absolute and relative energy resolution of the N1 (0°) detector with 230 MeV/nucleon ^{4}He ion beams.

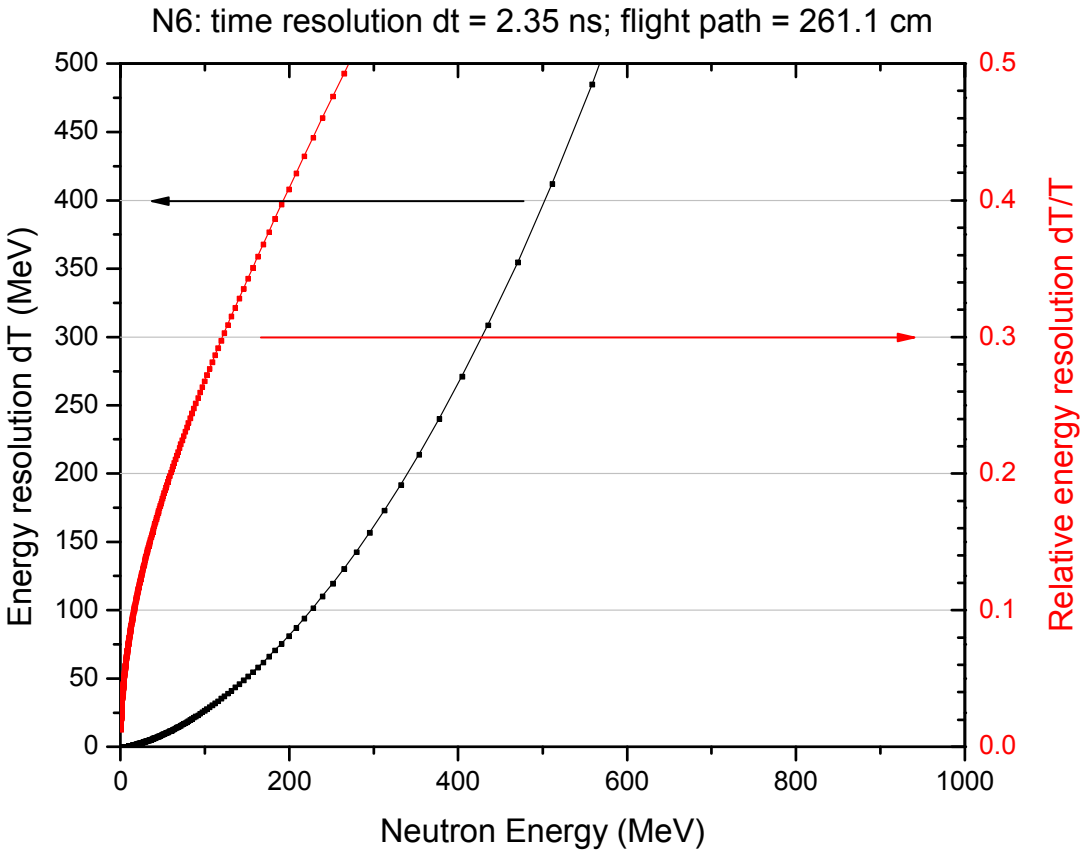

Figure 32. The absolute and relative energy resolution of the N6 (121°) detector with 230 MeV/nucleon ^{4}He ion beams.

MeV/nucleon ^{4}He beams and three target materials. It is clearly seen that the energy resolution becomes worse much quickly with increasing neutron energy for shorter flight path than for longer flight path.

II.5.c Double-differential spectra

Secondary neutrons created by heavy ion interactions can be schematically divided into three stages during a nuclear reaction: breakup of projectile-like fragment, decay of the composite system created by the fusion of two ions in the pre-equilibrium stage, and evaporation of target-like fragment. Those high-energy and forward-focused neutrons come from direct knock-on process and breakup of projectile-like fragments in nucleus-nucleus interactions. Neutrons with energies up to 2-3 times the incoming beam energy per nucleon can be produced by these interaction mechanisms. It is noted that the velocities of the neutrons corresponding to the broad peak at 0° are approximately 60-80% of the projectile velocity, and the peak is more prominent for lighter targets, e.g. PMMA or water targets in our case.

At intermediate energies (between 20 MeV and ~60% of beam energy per nucleon), the spectra are dominated by the pre-equilibrium de-excitation of the composite system created by the overlap of two ions, where a sizable number of nucleons from projectile as well as target mix. The thermalization process is proceeded via several nucleon-nucleon collisions and emissions into continuum single nucleons and clusters produced by nucleon coalescence.

At the end of the fast reaction stages, the excitation energy of the residual nucleus or the fragments in a nucleus-nucleus reaction is shared by a large number of nucleons, and such excitation energy is dissipated through evaporation or Fermi breakup. Neutrons created in this stage are essentially isotropic and are below 20 MeV since the target residue is moving slowly in the lab frame. It is noted that the relative contribution to the overall spectra from this mechanism increases for heavier targets (iron > PMMA, water in our case).

The overall TTY spectra in this measurement show a great consistency with the previous TTY measurement of ^{4}He projectiles bombarding other target materials at the same or close energies [17 - 19]. They all have the major components from three interaction mechanisms mentioned above (projectile breakup, target evaporation, and decay of the overlap region) in the TTY spectra.

II.5.d Comparison of experimental data and model calculations

From Figure 23 through Figure 28, it is seen that the simulation results from FLUKA, MCNP and PHITS generally agree with the experimental data, especially in the intermediate and low energy regions at angles at and above 30° for the 230-MeV/nucleon ^{4}He projectile systems. However, some disagreements exist not only between the experimental data and the simulations but also between different model calculations.

Considering the broad energy peak at 0° in the 100-MeV/nucleon ^{4}He systems, the MCNP calculations predict the peak location quite well for both light and heavy targets. However, the peak magnitude is about 3 times higher than the experiment data for light PMMA and water targets. The peak heights predicted by FLUKA are only about half of the measured data for all three targets, while the FLUKA simulations only slightly underestimate the peak energies by a few MeV. Though the peak heights predicted by PHITS calculations are about 10-40% higher than the measured data for water and PMMA targets, the peak energies are ~15 MeV lower than the experimental data for the light targets and there is no peak in the 0° for the iron target, indicating that PHITS underestimates the neutron contribution from projectile breakup.

As the projectile energy increases from 100 to 230 MeV/nucleon, all simulations underestimate the peak heights for three targets, except that MCNP still overestimates the peak heights for the water and the PMMA targets by a factor of 3 with both 100-and 230-MeV/nucleon ^{4}He ions. It is noted that for the heavier target (iron), MCNP's model calculation underestimates the peak height by a factor

of ~2.5. In addition, the peak energies predicted by MCNP's model are ~83% of the beam energy per nucleon (~191 MeV) for the water and PMMA targets, while the measured peak energies are at ~ 61% of the specific beam energy (~140 MeV). FLUKA's physics models show a consistent underestimation of high-energy neutrons contributed from projectile breakup mechanism for 230 MeV/nucleon ^{4}He projectiles: the peak locations agree with the measured data with the peak heights about half of the experimental data for all targets. If we look at the PHITS model calculations, there is no peak for the iron target with both 100- and 230-MeV/nucleon ^{4}He ions. However, in contrast of the overestimation of the peak height for the light targets bombarded by 100-MeV/nucleon ^{4}He ions, PHITS now underestimates the peak heights by a factor of ~2 as the projectile energy increases to 230 MeV/nucleon. It is also noted that compared to the measured data, in the 230-MeV/nucleon ^{4}He + water/PMMA systems, PHITS predictions have much narrower peaks, with a peak center at ~77% of the specific beam energy and a small hump at the lower-energy side of the peak.

Also, for both beam energies and for secondary neutrons at energies above the specific beam energy (MeV per nucleon), MCNP's physics model matches the data best for both projectile energies among all three codes for angles below 30° and starts to underestimate the neutron yields with increasing energies at larger angles. FLUKA and PHITS simulations both show a more rapid decrease than the measured data in this high energy region. In particular, FLUKA's model calculations almost fail to create such high-energy neutrons for the iron targets at both projectile energies.

There are also some differences among the data and the model calculations in the low energy range (< 20 MeV) in the 0° and 15° spectra for the light targets (water and PMMA). The inter-model differences are as large as an order of magnitude, such as the 0° calculations in the 100 MeV/nucleon ^{4}He + PMMA system. Though neutrons were able to be measured only above 5-8 MeV in the forward direction due to the limitation of the neutron/gamma discrimination and the

background contribution, the trend of the neutron spectra for the evaporation component still can be found from larger and backward angles since the secondary neutrons generated from evaporation of target-like fragments are emitted isotropically. As such, it can be inferred that all of the model calculations underestimate the low-energy neutron yields for 230-MeV/nucleon ^{4}He stopping in the light targets (PMMA and water).

II.5.e Angular distributions and total neutron yields

Figure 33 shows the angular distributions of all systems with 230-MeV/nucleon ^{4}He projectiles and of all systems with 100-MeV/nucleon ^{4}He projectiles. The angular yields (in unit of $neutrons \cdot sr^{-1} \cdot ion^{-1}$) were obtained by integrating the TTY spectra over the neutron energies above the threshold, which is 7 MeV for 100-MeV/nucleon ^{4}He projectiles and 5 MeV for 230-MeV/nucleon ^{4}He projectiles, for each emission angle.

Figure 34 shows the normalized angular distributions for all systems; in this figure, the normalized angular yields are 1.00 at 0° for all systems. It is noted that the angular yields for 100-MeV/nucleon ^{4}He projectiles were obtained by interpolation for 30° and by extrapolation for 120°.

It is seen in Figure 33 that the angular yields are higher for higher-energy projectiles. Also, lighter targets create more secondary neutrons in the forward direction owing to the higher probability of peripheral collisions and projectile breakup, whereas heavier target, such as iron, create more neutrons at large and backward angles because the contribution for evaporation of target-like fragments increases as target nuclei mass increases. It can be more clearly seen in the normalized angular distributions shown in Figure 34 that the forwardness of the angular distributions become stronger as the projectile energy increases and as target nuclei mass decreases.

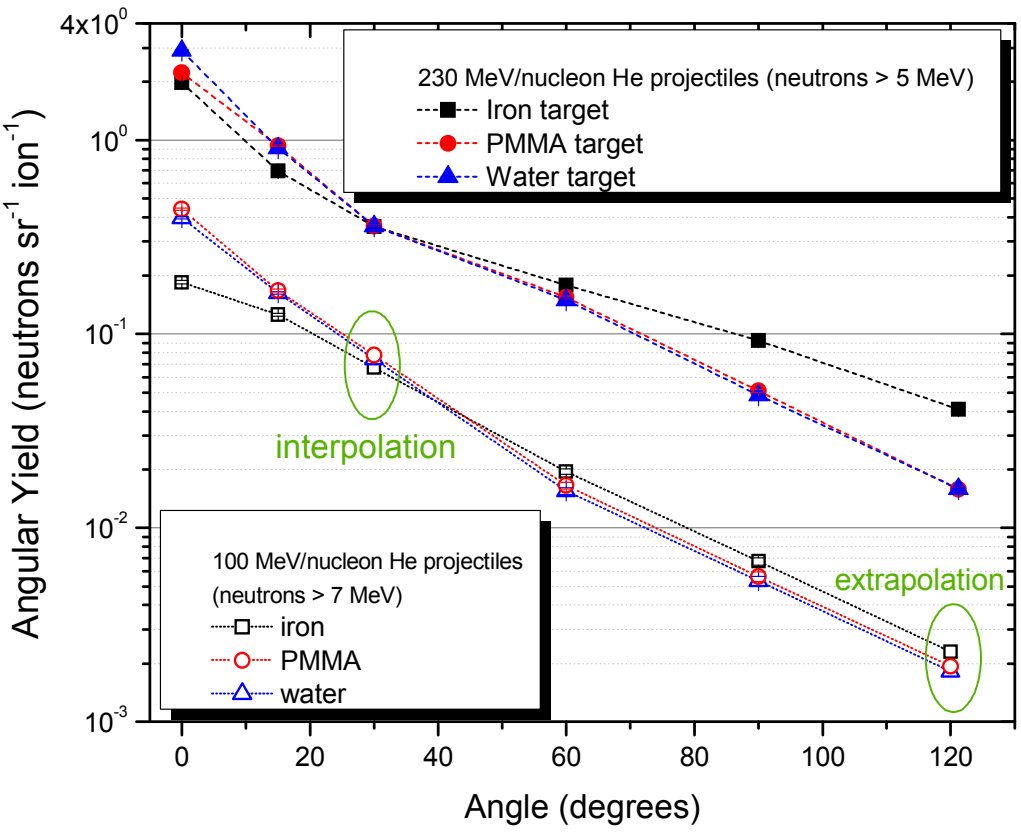

Figure 33. The angular yields of 230 MeV/nucleon ^{4}He + iron/PMMA/water for neutron energy above 5 MeV, and the angular yields of 100 MeV/nucleon ^{4}He + iron/PMMA/water for neutron energy above 7 MeV.

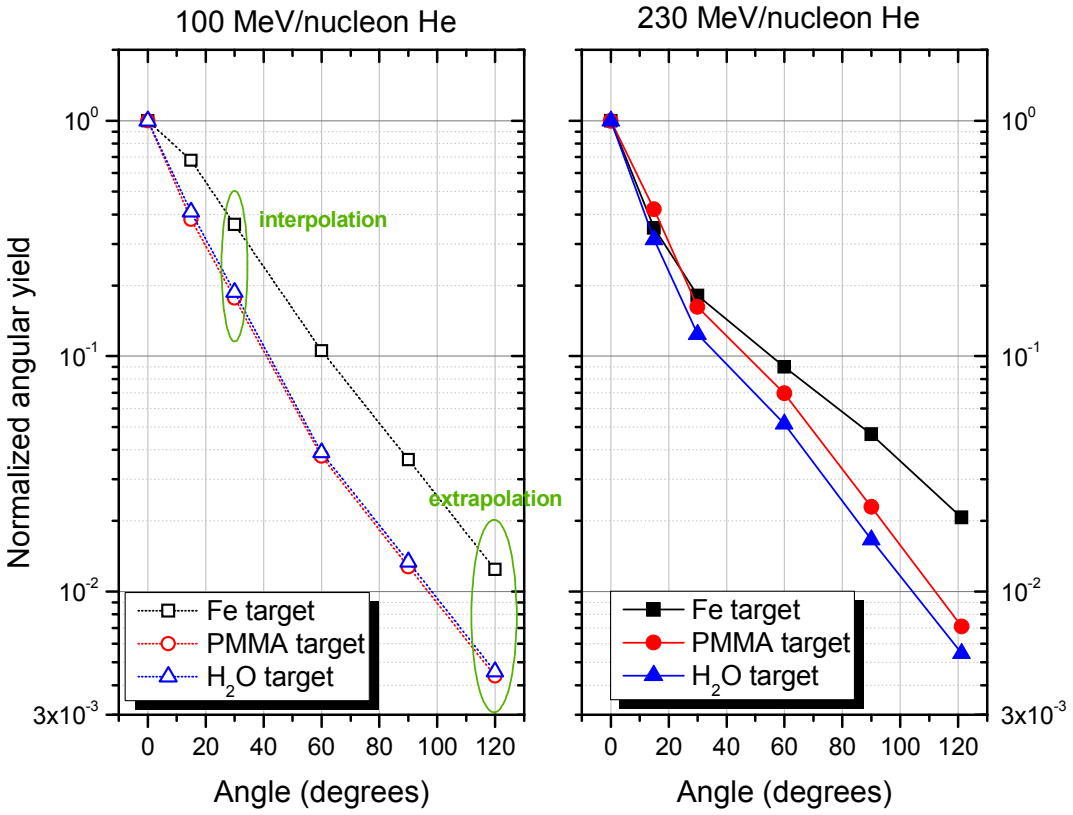

Figure 34. The normalized angular yields for all systems.

The neutron's angular yields were further integrated from 0° to 180° by the following equation:

$$Neutron\ yield\left(\frac{neutrons}{ion}\right) = \int_0^{180^\circ} \left(\frac{neutrons(\theta)}{\Delta\Omega(sr) \times (\#of\ He\ ions)}\right) sin\theta d\theta \int_0^{2\pi} d\phi \qquad \textbf{(7)}$$

where $neutrons(\theta)$ is the number of neutrons measured at a specific azimuthal angle θ,

$\Delta\Omega$ is the solid angle in sr,

θ is the azimuthal angle in a spherical coordinate system (emission angle), and

ϕ is the polar angle in a spherical coordinate system.

The cumulative angular yields over the azimuthal angle θ for all systems are shown in Figure 35, and the total neutron yields per ^{4}He ion along with the statistical errors are listed in Table 8. Both of Figure 35 and Table 8 show that the higher the projectile energy is, the more the total number of neutrons created by an incoming ^{4}He, whereas the neutron yield is somewhat independent of target materials for the thick target measurements. It can be observed in Figure 35 that about more than 90% of the secondary neutrons are emitted toward the forward-directional hemisphere (θ < 90°).

Table 8 also lists the neutron yields per ^{4}He ion measured with 100-MeV/nucleon ^{4}He + thick C and Cu targets with neutron energies above 5 MeV for angular distribution from 0° to 90° [16], as well as with 177.5-MeV/nucleon ^{4}He + thick H_2O and steel with neutron energies above 10 MeV for the entire sphere [19]. Although the integration cutoff energies or the angular ranges are not exactly the same as the values used for this measurement, the reported values of the neutron yield from 100-MeV/nucleon ^{4}He projectiles are still close to each other, and the reported value of 177.5-MeV/nucleon ^{4}He projectiles also agrees the trend that neutron yields are highly dependent on projectile energies.

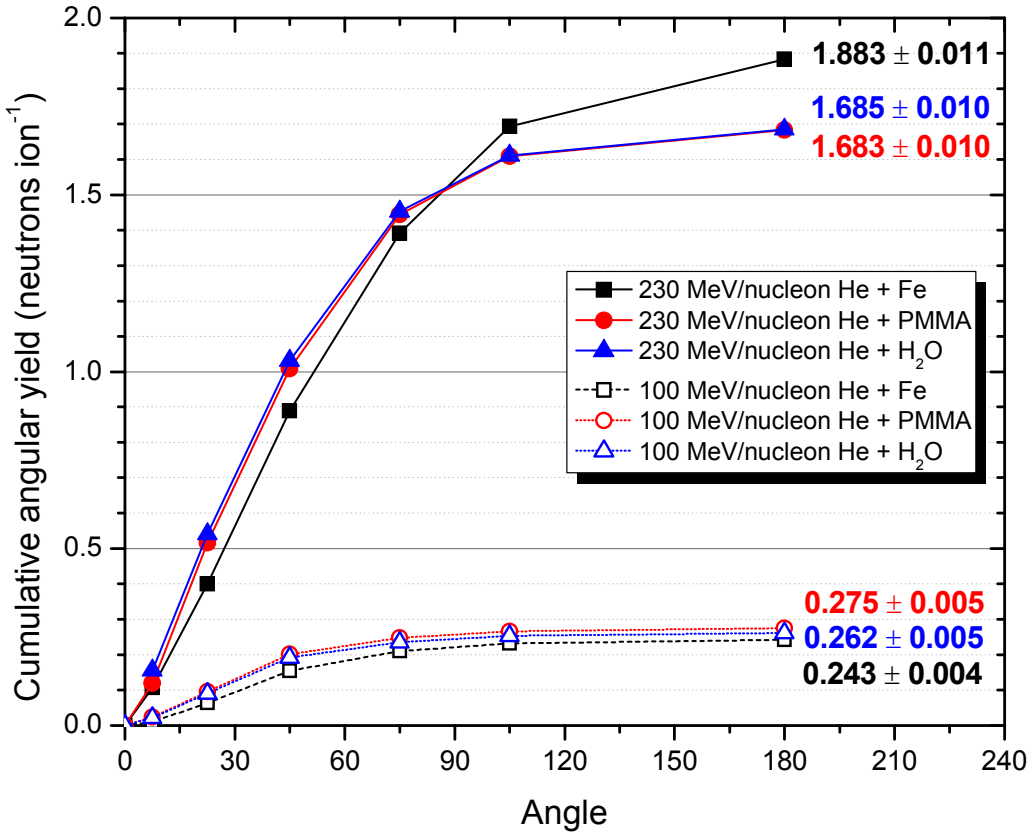

Figure 35. The cumulative angular yields of 230 MeV/nucleon ^{4}He + iron/PMMA/water for neutron energy above 5 MeV, and the cumulative angular yields of 100 MeV/nucleon ^{4}He + iron/PMMA/water for neutron energy above 7 MeV.

Table 8. Total neutron yields per ion for all the systems of this measurement.

System	Threshold	Angular range	Neutron yield (neutrons ion^{-1})
100 MeV/nucleon He + Fe	7 MeV	0° - 180°	0.243 ± 0.004 (1.6%)
100 MeV/nucleon He + PMMA	7 MeV	0° - 180°	0.275 ± 0.005 (1.7%)
100 MeV/nucleon He + H_2O	7 MeV	0° - 180°	0.262 ± 0.005 (1.8%)
100 MeV/nucleon He + C [16]	5 MeV	0° - 90°	0.26
100 MeV/nucleon He + Cu [16]	5 MeV	0° - 90°	0.28
177.5 MeV/nucleon He + H_2O [19]	10 MeV	0° - 180°	0.52
177.5 MeV/nucleon He + steel [19]	10 MeV	0° - 180°	0.51
230 MeV/nucleon He + Fe	5 MeV	0° - 180°	1.883 ± 0.011 (0.6%)
230 MeV/nucleon He + PMMA	5 MeV	0° - 180°	1.683 ± 0.010 (0.6%)
230 MeV/nucleon He + H_2O	5 MeV	0° - 180°	1.685 ± 0.010 (0.6%)

II.6 Summary and conclusions

The measurement of secondary neutron created by 100- and 230-MeV/nucleon ^{4}He ions, respectively, stopping in thick iron, PMMA and water targets was performed and the results including the double-differential thick target yields, angular distributions and total neutron yields per ion, were presented in this chapter. The measurement results are consistent with the previous thick target measurement data of ^{4}He ions in showing contributions from projectile breakup, emission from an overlap region, and from target evaporation.

Three Monte Carlo simulations codes – FLUKA, MCNP, and PHITS – were also employed with their default physics models to simulate the experimental results. From the comparison with experimental data, though the model calculations agree the experiment data very well at intermediate and large angles in intermediate and low energy ranges, the physics models implemented in these radiation transport codes need to be improved particularly in 1) the underestimation of neutrons created from the ^{4}He ion interactions at the high-energy end of the spectra at each angle for FLUKA's and PHITS's models, 2) the prediction of the high-energy peaks at 0˚ for all systems and all models, and 3) the underestimation of low-energy neutrons at small angles for 230-MeV/nucleon ^{4}He + light targets. More sophisticated physics models are needed to be capable of adequately describing the neutron production from ^{4}He projectile breakup.

CHAPTER III
Benchmark of secondary neutron production cross sections from heavy ion interactions

III.1 Introduction

Knowledge of high-energy heavy-ion induced nuclear reactions is critical in diverse fields including medicine, space exploration, and accelerator facilities for scientific research. For medical applications, ion beams with protons or heavier particles have become commonly used for cancer treatment. The accurate prediction of the radiation fields delivered from the beam line is necessary for dose assessment and optimization in treatment, and not only primary ions but also secondary particles must be considered. For space exploration, many mission scenarios, such as manned International Space Station (ISS) or lunar bases and missions to Mars, human and spacecraft-equipped devices will both face long-term exposures to Galactic Cosmic Rays (GCR) and Solar Energetic Particles (SEP), which are predominantly composed of ions from proton to iron. Adequate shielding will be required to reduce the receiving dose from the inherent radiation environment. Understanding the interaction of heavy ions with spacecraft materials and human body is critical for shielding design, dose assessment for astronauts, and evaluation of radiation damage to equipment. Regarding heavy-ion accelerator facilities for scientific research such as the Facility for Rare Isotope Beams (FRIB) at the Michigan State University and the Rare Isotope Beam Factory (RIBF) at the RIKEN (Institute of Physical and Chemical Research) Accelerator Research Facility (RARF), simulation and transport of heavy ions are relevant for facility design, including production targets, beam dumps, shielding, and estimates of component lifetimes.

Currently there are several Monte Carlo simulation codes that are capable of simulation and transport of heavy ions, such as PHITS [11], FLUKA [12], MCNP [13], MARS15 [34], and HETC-HEDS [35]. Many efforts have been made for

validation and verification of the double differential production cross sections of secondary neutrons in order to improve the physics models implemented in the radiation transport codes. Measurements of secondary neutron cross sections from heavy ion interactions was conducted by several groups [35 - 38]. Benchmark calculations by these Monte Carlo codes have also been performed [32, 33, 39 - 44]. However, most of the calculations benchmarked only a few experiments, and none of them have a systematic inter-comparison between the experimental data and several simulation codes and covers the ion species and target from light to heavy in a diverse energy range. As such, we initiated this inter-comparison study aiming to improve the physics models employed in the Monte Carlo codes. The double-differential neutron production cross sections (DDXs) instead of the thick target neutron yields (TTYs) were selected as the comparison observable. It was because that the DDXs data provide better tests of the secondary particle production mechanisms since they have very limited number of secondary interactions, whereas the final TTY spectra are contributed by primary, secondary and even tertiary interactions as well as transport and attenuation of particles. For these reasons, measured DDXs are chosen as a good benchmark for the physics models that used in secondary particle production. Regarding the radiation simulation and transport codes, we selected PHITS, FLUKA, and MCNP for benchmark calculation primarily because they are well established and in widespread use for particle and radiation transport calculations.

III.2 Experimental data

Fifteen experiments were selected for benchmark calculations. Detailed information about the experiments and corresponding references can be found in Table 9. One of the selected experiments, 135-MeV/nucleon Ne + ^{nat}Cu, was performed at the Institute of Physical and Chemical Research (RIKEN) in Wako, Japan, and the rest of them were conducted at the Heavy Ion Medical Accelerator

Table 9. Cases studied for the benchmark calculations.

No.	Beam species	Beam energy (MeV/nucleon)	Target	Z	Density (g/cm^3)	Thickness (g/cm^2)	Facility	Ref.
1	C-12	400	^{nat}Li	3	0.53	2.9904	HIMAC	Heilbronn‡
2	C-12	400	^{nat}C	6	1.80	9.00	HIMAC	[36]
3	C-12	400	^{nat}Al	13	2.70	3.9852	HIMAC	Heilbronn‡
4	C-12	400	^{nat}Cu	29	8.96	13.40	HIMAC	[36]
5	C-12	400	^{nat}Pb	82	11.34	9.08	HIMAC	[36]
6	Ne-20	135	^{nat}Cu	29	8.92	0.27	RIKEN	[37]
7	Ne-20	400	^{nat}Cu	29	8.96	4.47	HIMAC	[36]
8	Ne-20	600	^{nat}Cu	29	8.96	4.47	HIMAC	[36]
9	Ar-40	400	^{nat}Cu	29	8.96	1.34	HIMAC	[36]
10	Kr-84	400	^{nat}Li	3	0.53	0.47	HIMAC	[38]
11	Kr-84	400	^{nat}C	6	1.80	0.55	HIMAC	[38]
12	Kr-84	400	^{nat}Al	13	2.70	0.54	HIMAC	[38]
13	Kr-84	400	^{nat}Cu	29	8.96	0.90	HIMAC	[38]
14	Kr-84	400	^{nat}Pb	82	11.34	1.02	HIMAC	[38]
15	Xe-132	400	^{nat}Cu	29	8.96	0.45	HIMAC	[38]

‡ The data were obtained from private communication.

Center (HIMAC) of the National Institute of Radiological Sciences (NIRS) in Chiba, Japan.

The top view of the experimental setup at RIKEN is shown in Figure 36 [37]. The beam swinger (a dipole magnet) was used such that it was able to measure neutron spectra from 0°, 15°, 30°, 50°, 80° and up to 110° relative to the beam direction. The neutron spectra were measured with NE213 liquid scintillation detectors using the time of flight technique. The runs with shadow bars were not conducted due to the beam configuration, but the background was estimated by the blank target runs. More details can be found in Ref [15, 37].

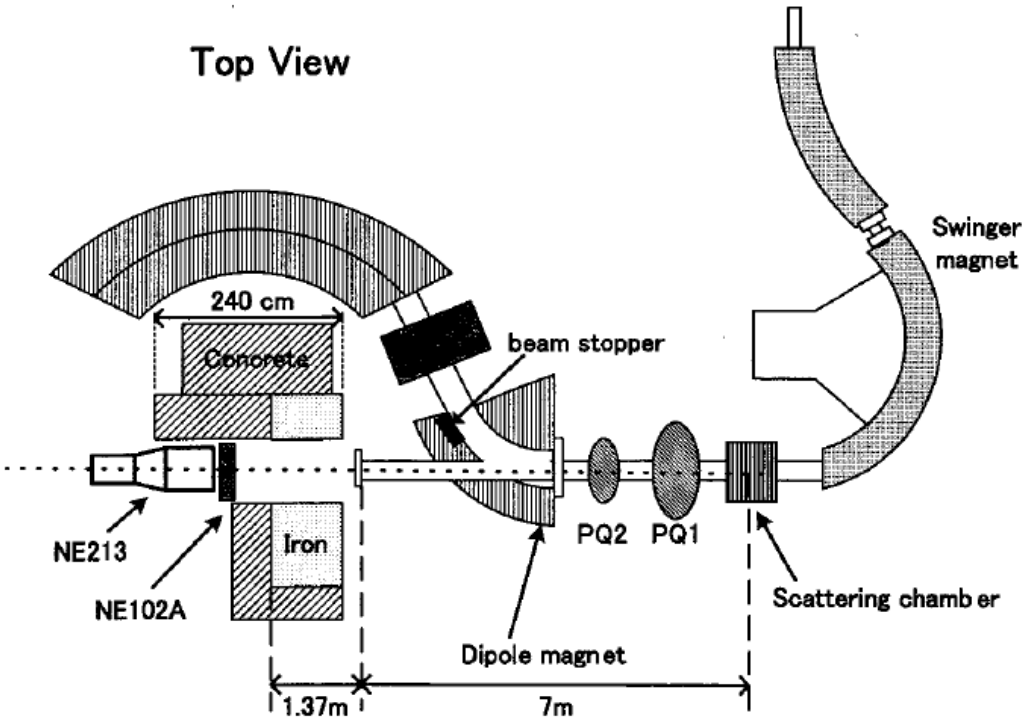

Figure 36. The experimental setup of the measurement done at RIKEN [37].

For the HIMAC experiments, the double differential neutron production cross sections were measured at seven angles (5˚, 10˚, 20˚, 30˚, 40˚, 60˚, 80˚), and the schematic diagram of the experimental setup is shown in Figure 37 [38]. The neutron spectra were also measured by the time of flight method with NE213 liquid scintillators and NE102A plastic scintillators, as in the RIKEN experiments. The background was subtracted from the blank target runs as well as the runs with iron shadow bars in front on the detector. More experimental details can be found in Ref [36, 38].

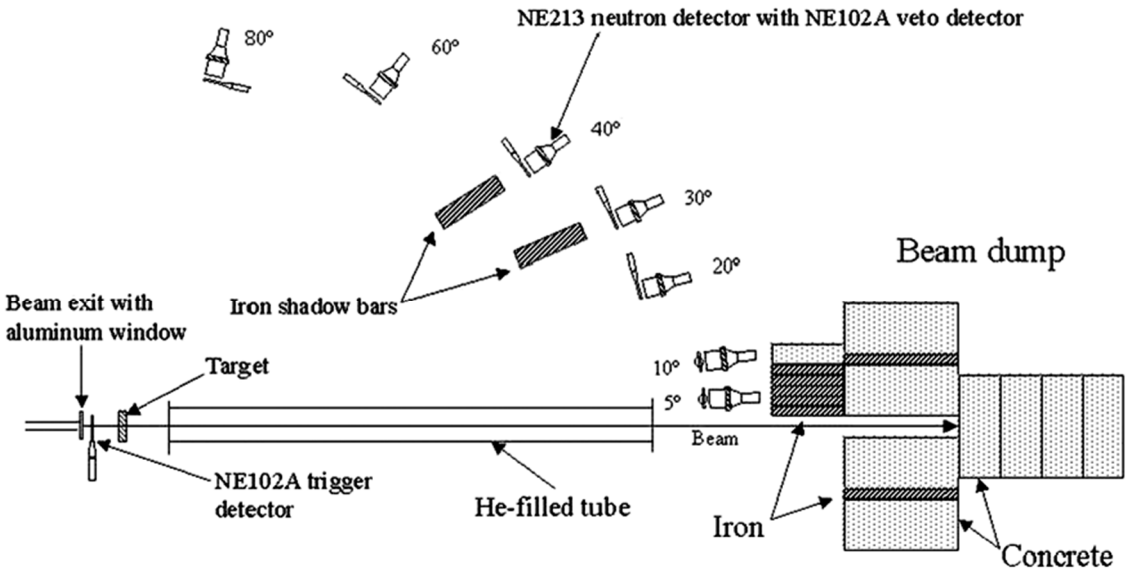

Figure 37. The experimental setup of the neutron cross section measurements done at HIMAC [38].

The experimental data used in this benchmark project (No. 2 and 4-15 in Table 9) are accessible from the CD-ROM accompanying a published handbook [15] in a tabulated form. Part of these data are also available in EXFOR. However, the experimental data of No. 1 and 3 listed in Table 9, which were measured by L. Heilbronn et al. in 2001 at HIMAC, were obtained from private communication and have not been published yet. Also, the data for experiment No. 2, 4-9 listed in Table 9, the detector efficiencies were calculated by CECIL [45], but the data for No. 10-15 in Table 9 were reevaluated by a revised efficiency calculation code SCINFUL-QMD [27] as was done in Ref. [39].

III.3 Monte Carlo simulations

Three Monte Carlo simulation codes including PHITS, FLUKA, and MCNP were employed for the benchmark calculations for their established and widespread use for particle transport calculations. The physics models employed in each code and the geometry setup are described in this section. The physics models used are quite similar to those described in section II.4. However, the ion species, target materials, and beam energies cover a wider range in this study than in the thick target measurement. Thus the major differences in the physics models will be pointed out below.

III.3.a Physics models in PHITS, FLUKA, and MCNP

PHITS

The PHITS code version 2.64 and 2.73 were the latest versions at the time when the calculations were performed. The cut-off energies of particle transport were 0.01 MeV for protons, 0.1 MeV for neutrons, electrons, positrons and photons, and 0.1 MeV/nucleon for nucleus equal or heavier than deuterons.

As seen in Figure 20 [29], PHITS uses the JAERI Quantum Molecular Dynamics (JQMD) model for nucleus-nucleus (A-A) collisions below 100 GeV/nucleon. Hadron-nucleus (h-A) interactions at energies between 3 to 200 GeV are treated with the Jet AA Microscopic Transport Model (JAM). At energies below 3 GeV, the Intra-Nuclear Cascade of Liège model version 4.6 (INCL 4.6) is used to simulate the dynamic stage of reactions induced by hadrons and light ions (up to alpha). The JQMD, JAM, and INCL4.6 are all followed by the Generalized Evaporation Model (GEM), in which stage evaporation and fission are in competition during the de-excitation of an excited nucleus. The neutron transport is based on the evaluated nuclear data library JENDL-4.0 for energies below 20 MeV and switched to physics models for energies above 20 MeV.

FLUKA

The FLUKA code version 2011.2c was used for the benchmark calculations. The PRECISIOn defaults declarations were chosen. For neutrons energies below 20 MeV, FLUKA uses its own group-wise neutron cross section data library which is based on the evaluated data such as ENDF/B, JEF, JENDL etc..

Hadron-nucleon inelastic collisions in FLUKA are modeled based on resonance production and decay below a few GeV. Hadron-nucleus (h-A) interactions below 5 GeV/nucleon are treated by the Pre-Equilibrium-Approach-to-NUclearThermalization (PEANUT) package which described a Generalized IntraNuclear Cascade (GINC) and a pre-equilibrium stage followed by equilibrium processes including evaporation, fission, Fermi break-up, and gamma de-excitation. FLUKA treats nucleus-nucleus (A-A) interactions with the Boltzmann Master Equation (BME) at energies below 125 MeV/nucleon, with the modified Relativistic Quantum Molecular Dynamics (RQMD) model for energies between 125 to 5000 MeV/nucleon, and with the Dual Parton Model (DPMJET-II or DPMJET-III) above 5000 MeV/nucleon, which is beyond the scope of this study.

MCNP

The version used for this study was MCNP6 version 1.0.

For transport of neutrons and protons with energies below 150 MeV, tabulated cross section data are used. MCNP6 uses the cascade-exciton model (CEM, version 03.03) to simulate interactions of nucleons, pions, and photons at energies below 940 MeV/nucleon, and switches to the Los Alamos version of the quark-gluon string model (LAQGSM, version 03.03) to treat nucleon- and nucleus-induced fragmentation reactions at energies up to 1 TeV/nucleon. Both CEM03.03 and LAQGSM03.03 consider all stages of a nuclear reaction: intranuclear cascade, coalescence, and pre-equilibrium decay, followed by the equilibrium evaporation/fission of the compound nuclei. If the atomic numbers A of the residual nuclei after the intranuclear cascade are less than 13, CEM03.03 uses the Fermi breakup model at any stage of a reaction.

After calculating the coalescence stage of a reaction, both of LAQGSM03.03 and CEM03.03 move to the last slow stages of the interaction (pre-equilibrium decay and evaporation/fission) described by the GEM2 model.

It is noted that the default numbers of types of particles to be considered at the evaporation stage in CEM03.03 and LAQGSM03.03 are both 66 in MCNP6, but are changed to 6 in this study, i.e. only fragments lighter than ^{4}He (n, p, d, t, ^{3}He, and ^{4}He) being considered, to save computing time.

III.3.b Geometry setup

The geometry setup for this study is very similar to the simulation geometry setup for benchmarking the thick target measurement. A geometry consisting 7 ring detectors for the HIMAC experiments or 6 for the RIKEN experiment was used, as illustrate in Figure 38.

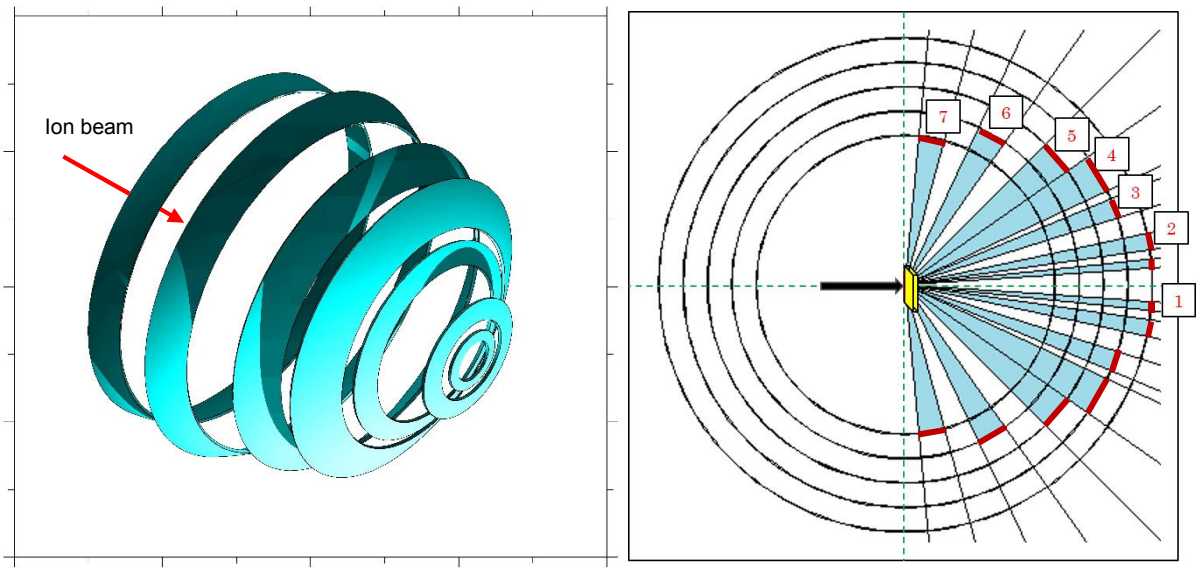

Figure 38. (left) Seven ring detectors used to score secondary neutrons produced from heavy ion experiments at HIMAC; (right) the calculation geometry; the scoring surfaces are labelled in red and the detector numbers can be referred to Table 10.

Table 10. Experimental and calculation parameters for the HIMAC experiments.

Detector No.	Angle (degrees)	Flight path (cm)	$\Delta\theta_{exp}$ (degrees)	$\Delta\theta_{calc}$ (degrees)	$\Delta\Omega_{calc}$ (sr)
1	5	506	0.72	1.0	0.019
2	10	506	0.72	2.5	0.076
3	20	456	0.80	2.5	0.187
4	30	456	0.80	5.0	0.548
5	40	406	0.90	5.0	0.704
6	60	356	1.0	5.0	0.948
7	80	306	1.2	5.0	1.079

A monoenergetic and monodirectional ion beam with 1 cm diameter impinged on the thin target located at the center of the sphere. Six ring-type detectors on a spherical surface, which have equivalent angles with the experimental setup, were setup to score secondary neutrons. The volume of the cavity delimited by the sphere was assumed to be void. Details of these calculation parameters for the HIMAC experiments can be found in Table 10.

Neutrons created from the target were scored when they passed through the spherical segments at each angle (each ring detector), and then the double differential neutron production cross sections in units of $barns\ /\ (MeV \cdot sr)$ were obtained using the following equation.

$$\frac{d^2\sigma}{dEd\Omega}\left(\frac{barn}{MeV \cdot sr}\right) = \frac{\phi(E,\ \theta)}{\Delta E(MeV) \times \Delta\Omega(sr) \times n \times t} \times a \quad \textbf{(8)}$$

where $\phi(E, \theta)$ is the number of neutrons per incoming beam ion across the spherical segment (ring detector) with a certain energy bin,

ΔE is the energy bin width in MeV,

$\Delta\Omega$ is the solid angle of the ring detector in sr,

n is the atomic density of the target material in $atoms/cm^3$,

t is the target thickness in cm, and

a is the conversion factor from cm^2 to barns.

III.4 Results and discussions

The results of this benchmark study will be discussed in three aspects, which are the dependence on 1) the target nuclei mass, 2) projectile mass, and 3) projectile energy. The plots presented in this chapter are organized by the three variables mentioned above. The enlarged comparison plots with three model

calculations along with the experimental data for individual beam/target configurations can be found in Appendix.1 Neutron double-differential cross sections.

III.4.a Target mass as a variable

To investigate the target-mass-dependent double differential neutron production cross sections (DDX), two sets of data were compared from 5° to 80°, one of which includes 400-MeV/nucleon ^{12}C ions (as the representative of light projectile) bombarding thin ^{nat}Li, ^{nat}C, ^{nat}Al, ^{nat}Cu, and ^{nat}Pb targets, and the other set contains 400 MeV/nucleon ^{84}Kr ions (as the representative of intermediate-mass projectile) impinging thin ^{nat}Li, ^{nat}C, ^{nat}Al, ^{nat}Cu, and ^{nat}Pb targets. The comparison results are respectively shown in Figure 39 (400-MeV/nucleon ^{12}C) and

Figure 40 (400 MeV/nucleon ^{84}Kr ions).

In general, all the physics models employed in each Monte Carlo code are able of reproduce the physical characteristics in the shape of double differential spectra, which contains 1) a high energy peak in the forward direction mainly contributed by the intranuclear cascade mechanism (and the breakup of projectile-like fragment in the pre-equilibrium stage for RQMD/BME model and CEM03.03/ LAQGSM03.03 model), 2) intermediate-energy (between 20 MeV and ~60% of beam energy per nucleon) neutrons dominated by the pre-equilibrium de-excitation of the composite system created by the fusion of projectile-fragment and target-fragment, and 3) low-energy neutrons created during the de-excitation of target-like fragments by evaporation. However, there are still some differences among the inter-model calculations and among experimental and calculated data.

It is seen in Figure 39 that MCNP (LAQGSM03.03 + GEM2) overestimates the peak magnitude almost by a factor of 10 and also overestimates the peak width for angles below 20° in the light projectile + very light target (^{nat}Li) system,

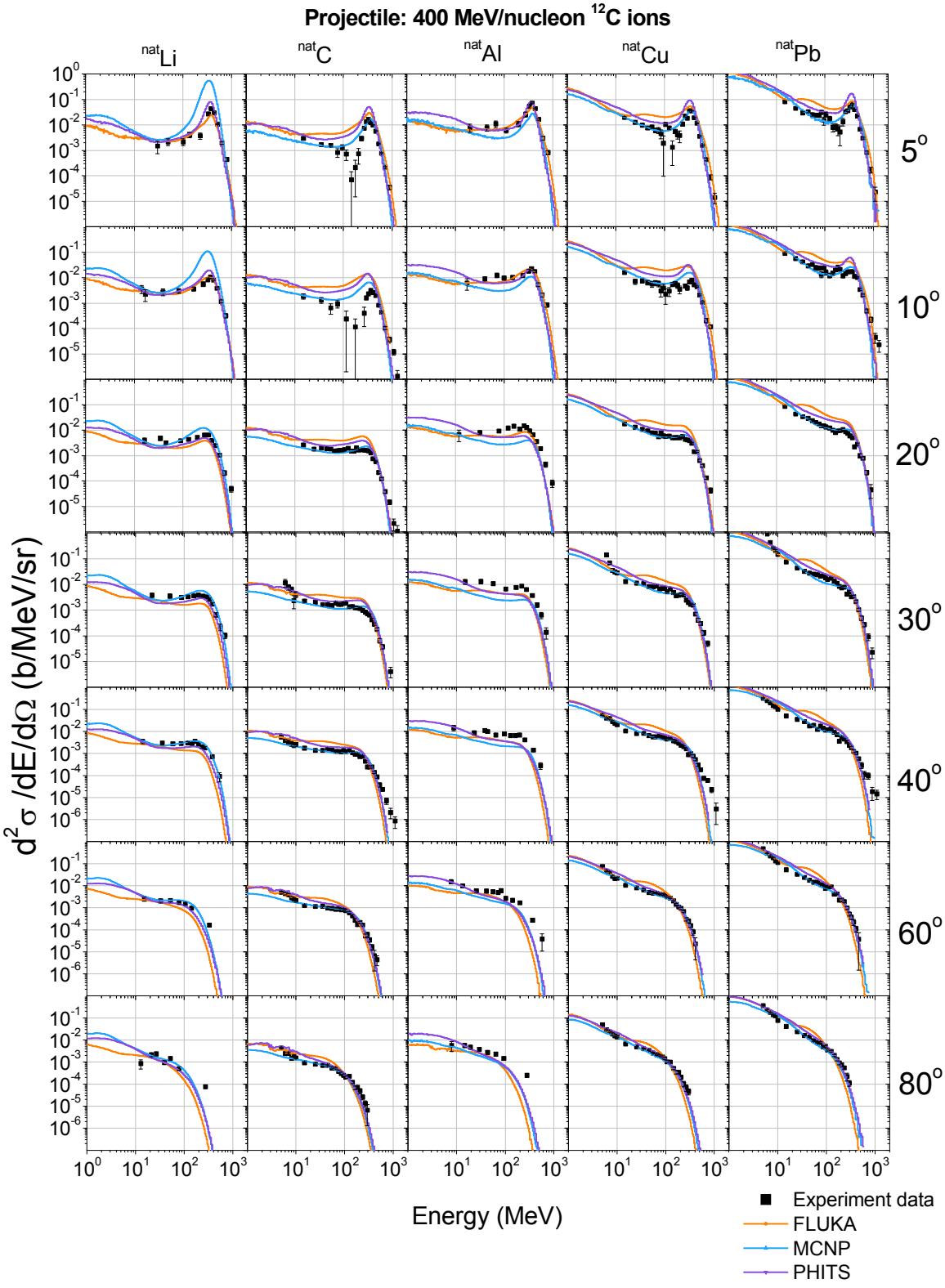

Figure 39. The target-mass-dependent DDX with 400-MeV/nucleon ^{12}C projectiles.

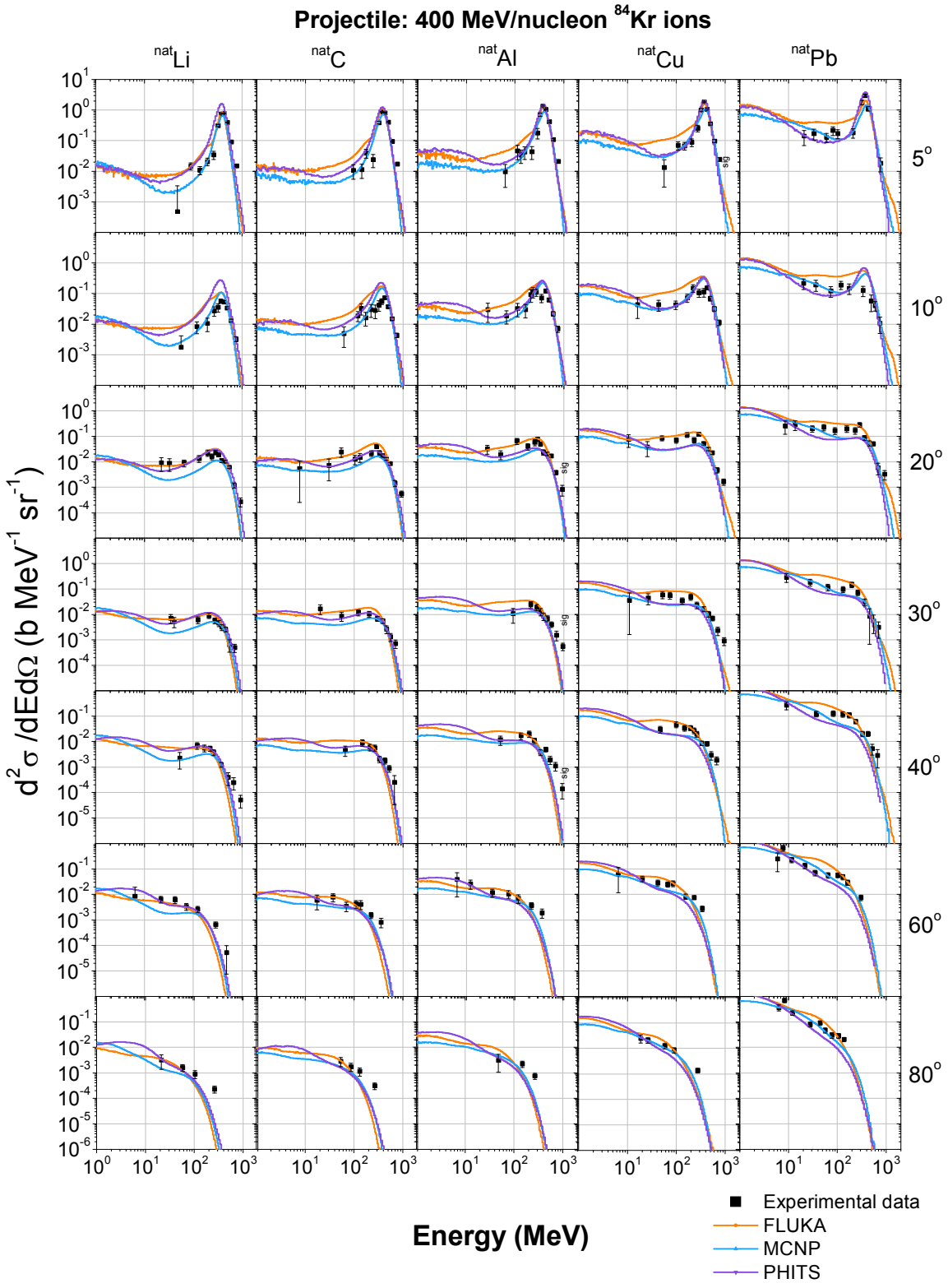

Figure 40. The target-mass-dependent DDX with 400-MeV/nucleon ^{84}Kr projectiles.

but the LAQGSM03.03 model predictions improve with heavier targets. Also, in nearly all systems except the one with ^{nat}Al targets, MCNP simulations agree with the experimental data very well over the entire energy range at angles larger than 20°; in the 400-MeV/nucleon ^{12}C + ^{nat}Al system, the MCNP model underestimates the secondary neutron yields at all angles, especially at intermediate energies and at angles from 10° to 40° degrees.

PHITS (JQMD + GEM) simulations predict the locations of the forward-direction high-energy peaks quite well in all systems, though the peak magnitudes are slightly overestimated for ^{nat}C, ^{nat}Cu, ^{nat}Pb targets. As for the intermediate and large angles, the PHITS simulation results are also in agreement with the experimental data in all systems except for an underestimation of intermediate-energy neutrons.

FLUKA (RQMD/BME) also predicts the 5°-peak location quite well; however, FLUKA evidently overestimates the neutron yields at intermediate energies at small to intermediate angles in the systems with ^{nat}C, ^{nat}Cu, ^{nat}Pb targets.

It is noted that differences exist among different models for neutron energies below 20 MeV with light targets (^{nat}Li, ^{nat}C, ^{nat}Al). Unfortunately, there are no experimental data available to validate the models, which is due in part to the limitation of the neutron/gamma separation capability of liquid scintillators in the cross section measurements, and in part to the background subtraction in the forward direction.

Figure 40 shows the inter-comparison results with the same target materials, but the projectile mass increases from ^{12}C ions to ^{84}Kr ions with same velocity. MCNP (LAQGSM03.03 + GEM2) no longer overestimates the high-energy peak in the forward direction in the system with very light targets. However, FLUKA (RQMD/BME) model calculations still show significant overestimation for intermediate-energy neutrons from ^{nat}Cu and ^{nat}Pb targets. As for PHITS (JQMD +

GEM), the model calculation cross sections are in-between the MCNP and FLUKA's values, in general.

III.4.b Projectile energy as a variable

The neutron production cross sections' dependence on the projectile energy was also investigated. A set of DDX experimental data along with the FLUKA, MCNP, and PHITS model calculations at various angles from 135-, 400-, and 600-MeV/nucleon ^{20}Ne ions interactions with ^{nat}Cu were compared and are presented in Figure 41. In general nearly all the models reproduce the experimental DDX quite well for intermediate-energy neutrons from intermediate to large angles. Most of the discrepancies occur in the forward direction and at energies beyond the beam energy per nucleon.

In the energy region beyond the beam energy per nucleon, Figure 41 shows that all of the three models underestimate the neutron cross sections at nearly all angles, and the model prediction values underestimate the experimental data more with increasing ^{20}Ne ion energies. The only exceptions are 1) MCNP6 (model LAQGSM03.03) at angles smaller than 30° in the 135-MeV/nucleon ^{20}Ne + ^{nat}Cu system, and 2) FLUKA (model RQMD) at 5° and 10° in the 400- and 600-MeV/nucleon ^{20}Ne + ^{nat}Cu systems.

If we consider the model predictions on the high-energy peaks at 0° or 5°, from the first row in Figure 41, it is found that MCNP predicts the peak centered at 95% - 101% of the specific beam energy, while the measured peaks were centered at about 90% - 92% of the specific beam energy. Moreover, MCNP underestimates the peak height for the 135-MeV/nucleon projectile data by 70% of the experimental data, and also underestimates the peak heights by ~55% of the measured data for 400 and 600 MeV/nucleon ^{20}Ne projectiles. The FLUKA's model prediction also slightly overestimates the peak centroid energy for 135 MeV/nucleon ^{20}Ne projectiles, which is similar to MCNP's simulation, whereas the peak energies agree with the experimental data quite well for higher-energy ^{20}Ne

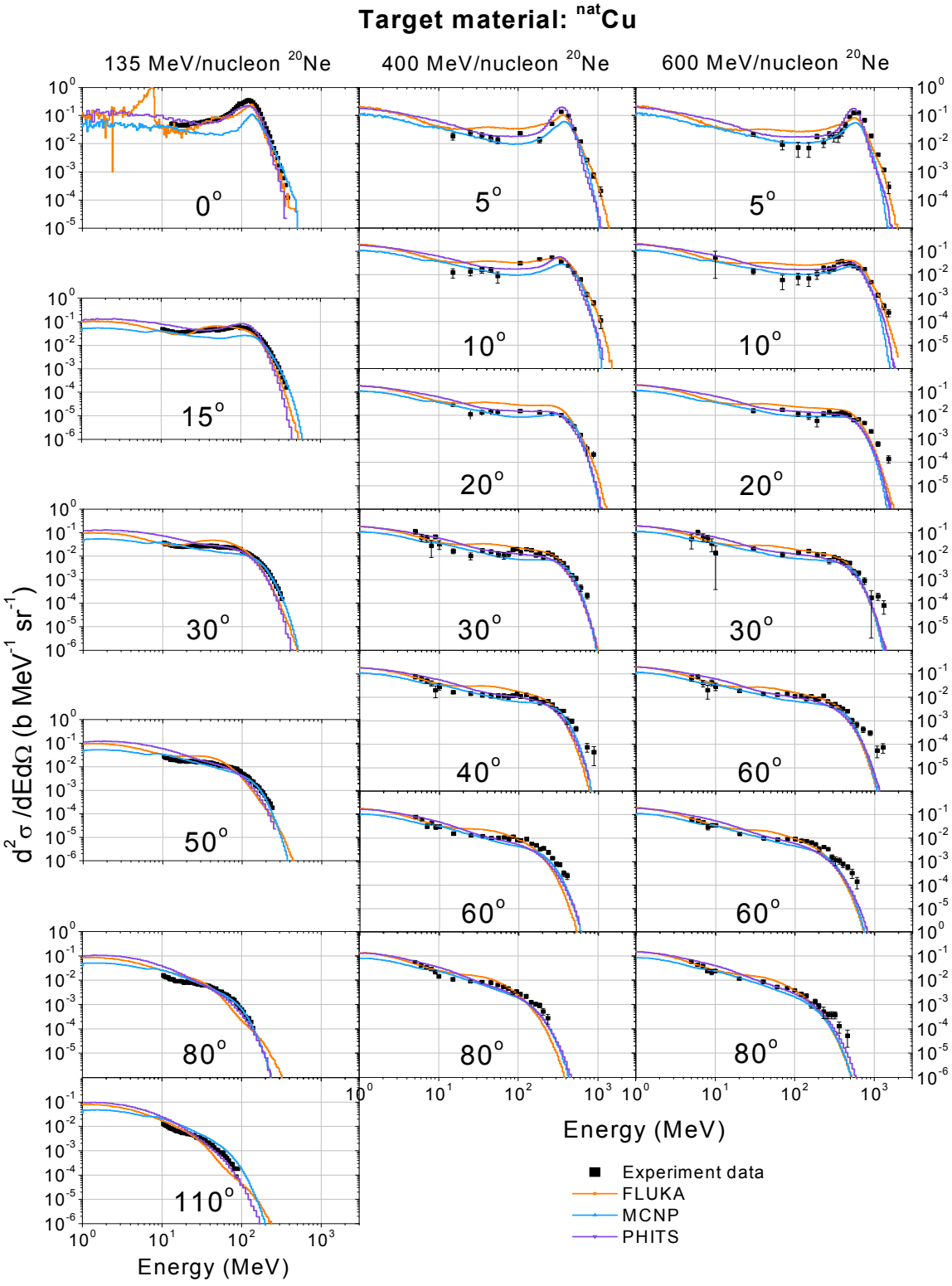

Figure 41. The projectile-energy-dependent DDX with ^{nat}Cu targets.

projectiles. Regarding the peak heights, FLUKA's models consistently underestimate the peak heights by 25% - 35% of the measured data for three energies of ^{20}Ne projectiles. However, PHITS models underestimate the peak height by ~35% for 135 MeV/nucleon ^{20}Ne projectiles but overestimate the peak heights by ~45% of the experimental data for 400 and 600 MeV/nucleon ^{20}Ne projectiles, though the peak centroid energies match the measured data quite well for all three energies.

Also note that the FLUKA's model calculation reveals a prominent increase (more than an order of magnitude) at energies between ~4 and 9 MeV in the 0° data, which is not physically reasonable in an evaporation mechanism. Further investigation showed that such increase only exists at angles smaller than 1°. We have contacted the FLUKA development group and confirmed that this phenomena is indeed an artifact due to an anomalous abundance of neutrons with zero energy in the center-of-mass system. In addition, FLUKA overestimates the neutron cross sections at intermediate energies, which is also found in Figure 39 and Figure 40.

It is worth noting that, for all systems shown in Figure 41 except the 0°-spectrum, all of the three models show a nearly parallel trend with low-energy neutrons, which are mainly contributed by the evaporation of target-like fragments during the de-excitation process. The model calculations are also consistent with the experimental data, indicating that the evaporation models work well across all ^{20}Ne projectile energies between 135 and 600 MeV/nucleon.

III.4.c Projectile mass as a variable

The investigation of the dependence of the neutron DDXs' on projectile mass is done by comparing ^{12}C, ^{20}Ne, ^{40}Ar, ^{84}Kr, and ^{132}Xe ions at the same specific energy of 400 MeV/nucleon impinging on a thin ^{nat}Cu target. The inter-comparison of three model calculations along with the experimental data are shown in Figure 42.

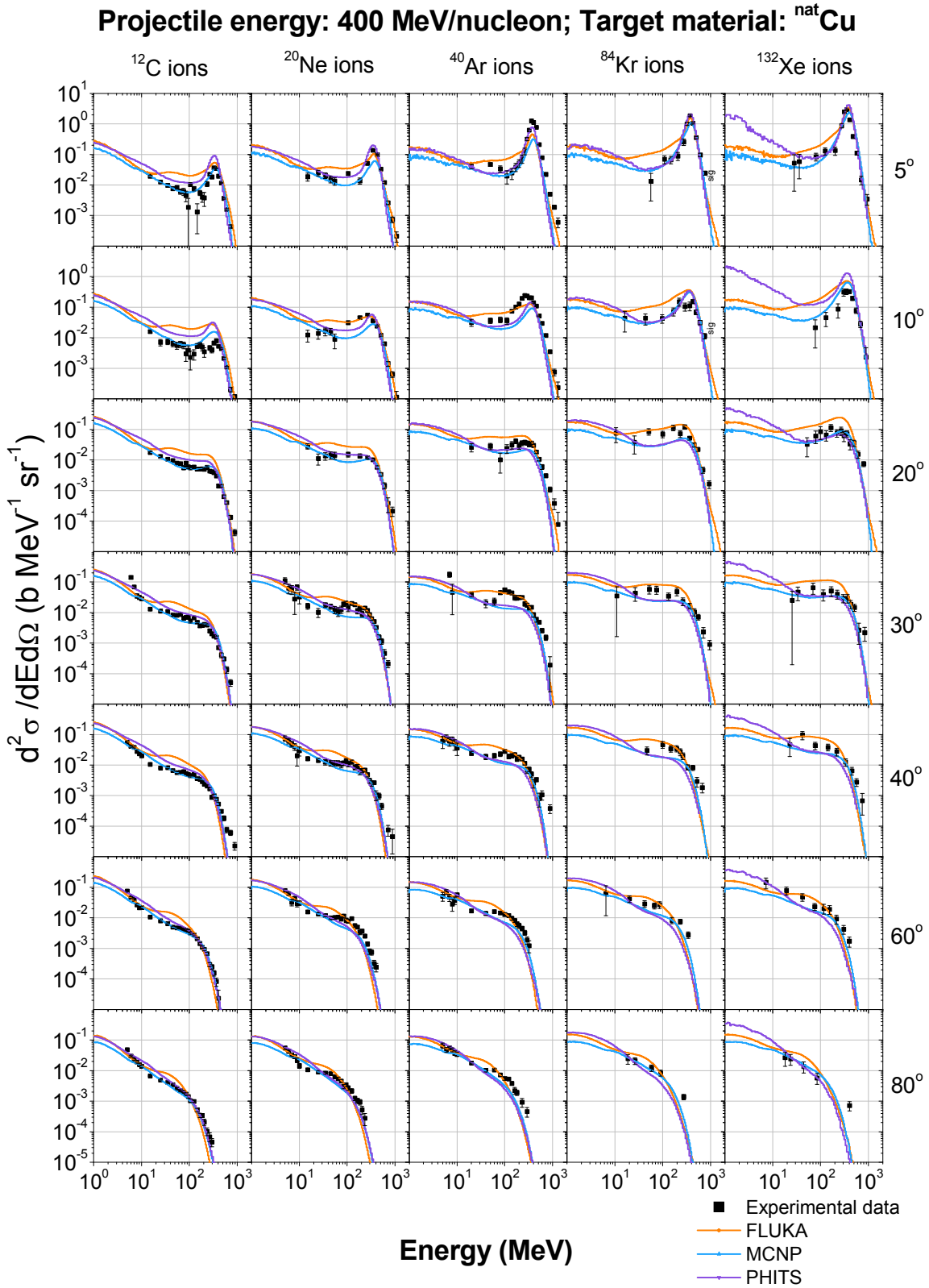

Figure 42. The projectile-mass-dependent DDX with ^{nat}Cu targets.

In general, simulations by three Monte Carlo codes agree with each other and consistent with the experimental data at angles greater than ~30° with lighter projectiles (^{12}C, ^{20}Ne, and ^{40}Ar). These physics models also predict the peak location at 5° quite well for these beam/target configurations, though PHITS slightly overestimates the peak magnitude for 400-MeV/nucleon ^{12}C + ^{nat}Cu and MCNP6 underestimates the peak heights for 400-MeV/nucleon ^{20}Ne/^{40}Ar + ^{nat}Cu.

The discrepancies among the models and the experimental data occurring at small angles are more significant for heavier projectiles. Figure 42 shows that the deviation for low-energy neutron DDXs predicted by models increases with the increasing projectile mass, particularly for spectra with ^{132}Xe projectiles in the forward direction. Though there was not only a lack of experimental data in that energy region but also a lack of measured data at backward angles, it can be inferred from spectra at larger angles (20° to 80°) that PHITS are likely to overestimate the low-energy neutron cross sections, since those low-energy neutrons are mainly contributed by isotropic evaporation from target-like fragments and should be the same order of magnitude at all angles.

Figure 42 also shows that the model-calculated DDXs do not reproduce the experimental data very well at angles between 10° to 30°, but it is hard to conclude which model preforms better with increasing projectile mass in this region. However, FLUKA's model generates more intermediate-energy neutrons than MCNP6 and PHITS, which is also seen in Figure 39 to Figure 41.

III.5 Summaries and recommendations

A series of measurement data for secondary neutrons created from heavy ion interactions was benchmarked by various Monte Carlo codes. The experimental data covered a wide range of projectile species (^{12}C, ^{20}Ne, ^{40}Ar, ^{84}Kr, and ^{132}Xe) and target materials (^{nat}Li, ^{nat}C, ^{nat}Al, ^{nat}Cu, and ^{nat}Pb) with projectile energies at several hundreds of MeV/nucleon. In order to validate the neutron

production mechanism in the physics models, a specific experiment observable, double differential cross section, was selected to compare with different model calculations, of which are default physics models implemented in three Monte Carlo codes – FLUKA, MCNP, and PHITS.

The comparison of neutron production data and calculations from heavy ion interactions was done and discussed in three respects: the dependences of target material, projectile species and beam energy. Generally all physics models are able to reproduce the major characteristics in the neutron double differential spectra, which includes 1) a high-energy peak in the forward direction centered roughly at the beam energy per nucleon, which is contributed from the intranuclear cascade and the breakup of projectile-like fragments in the pre-equilibrium stage, 2) intermediate-energy neutrons contributed by the pre-equilibrium de-excitation of the composite system created by the fusion of projectile-fragment and target-fragment, and 3) low-energy neutrons created during the final equilibrium stage that target-like fragments de-excite by evaporating nucleons.

However, some differences do appear not only among model calculations but also between measured data and calculations. In particular, CEM03.03/LAQGSM03.03 implemented in MCNP6 significantly overestimates the high-energy peak in the forward direction in the light + very light system with 400 MeV/nucleon. RQMD/BME implemented in FLUKA version 2011.2c overestimates the neutron cross sections at intermediate energies in nearly all systems expect the ones with lightest targets in our studies cases (^{nat}Li). FLUKA's physics model also generates an unnatural buildup at several MeV only in the 135-MeV/nucleon ^{20}Ne + ^{nat}Cu system; further investigation is required for this particular problem. Also note is that the greatest inter-model discrepancy on low-energy neutrons appear at small angles in the system with the heaviest projectile ^{132}Xe at 400 MeV/nucleon impinging on a thin ^{nat}Cu target. Though there is lack of relevant experimental data from that measurement, it can be inferred from other angles that

GEM implemented in PHITS version 2.73 over-predicts the amount of evaporating neutrons.

This study has provided a systematic benchmark and qualitative validation of neutron production cross sections from heavy ion interactions by default physics models implemented in FLUKA, MCNP, and PHITS. This information can provide critical information for model developers. To further quantitatively validate these physics models, a rating criteria is needed to be introduced and statistical analyzing method with various deviation factors, such as used in ref. [46 - 48] can be employed.

CHAPTER IV
Conclusions

Two major studies related to the secondary neutron production from heavy ion interactions were presented in this dissertation. One is the measurement of secondary neutrons produced from 100- and 230-MeV/nucleon ^{4}He ions respectively stopping in thick water, PMMA, and iron targets. The double differential thick target neutron yields (TTYs) were measured at 0°, 15°, 60°, and 90° for 100-MeV/nucleon ^{4}He projectiles, and at 0°, 15°, 30°, 60°, 90° and 121.2° for 230-MeV/nucleon ^{4}He projectiles. The measurement results were consistent with the previous thick target measurements with ^{4}He ion beams at similar energies or different target materials; they all had components from the three interaction mechanisms: projectile breakup, target evaporation, and decay of the overlap region.

The experimental observable, TTYs, was compared with model calculations fulfilled by the default physics models implemented in FLUKA, MCNP, and PHITS. Overall speaking, more sophisticated physics models are needed to be capable of adequately describing the neutron production from ^{4}He projectile breakup. The models show great differences at high-energy peak tails in forward direction and at energies above the high-energy shoulder at larger angles, which are mainly caused by inappropriate physics assumptions for the ^{4}He projectile breakup; the difference is greater for intermediate-mass targets (iron). Significant differences also appear at the 0°-high-energy peaks and the evaporation component at 0°. Nevertheless, at intermediate energies and at angles beyond 30°, the agreement between the model calculations and the experimental data is generally within 50% or better, which is quite satisfactory.

In the thick target measurement, physical observables, such as neutron TTYs, are the combined results of production from primary and secondary nuclear reactions as well as transport and attenuation within the thick targets. To further

investigate the neutron production from heavy ions and to validate the default physics models implemented in FLUKA, MCNP, and PHITS, a systematic benchmark of the existing experimental data for double differential neutron production cross sections (DDXs) from heavy ions was performed. The selected data set includes various combinations of projectile species (^{12}C, ^{20}Ne, ^{40}Ar, ^{84}Kr, and ^{132}Xe ions), projectile energy (135, 400, and 600 MeV/nucleon), and target mass (^{nat}Li, ^{nat}C, ^{nat}Al, ^{nat}Cu, and ^{nat}Pb). The inter-comparison with models and experimental data suggest an overall reasonable agreement especially at intermediate energies and from intermediate to large/backward angles. However, there are some discrepancies needing further investigation, such as the predictions of peak heights and peak energies for light projectiles for all models, FLUKA's overestimation of intermediate-energy neutrons, and PHITS's overestimation of low-energy neutrons for heavy + heavy systems. This benchmark study has provided qualitative and quantitative validation of the physics models for heavy ion interactions.

The results of these two studies presented in CHAPTER II and III of this dissertation provide critical information for model and radiation transport developers. The future improvements of these physics models will lead more accurate prediction in secondary neutrons from heavy ions, which can be applied to heavy ion therapy, radiation shielding in space, and shielding and target design for research accelerators.

LIST OF REFERENCES

[1] J. R. Castro *et al*., “15 years experience with helium ion radiotherapy for uveal melanoma.” *Int. J. Radiat. Oncol. Biol. Phys*., 39, 989 (1997).

[2] UT Southwestern to establish Center for Heavy Ion Radiation Therapy, Center Watch News Online, Feb. 12 (2015).
Available: http://www.centerwatch.com/news-online/article/7544/ut-southwestern-to-establish-center-for-heavy-ion-radiation-therapy#sthash.V0LIk7zn.dpbs.

[3] A project proposal by the Radiologische Universitätsklinik Heidelberg (project leader), the Deutsches Krebsforschungs-zentrum Heidelberg (DKFZ) and the Gesellschaft für Schwerionenforschung, Darmstadt (GSI) in cooperation with the Forschungszentrum Rossen-dorf (FZR), “Construction of a Clinical Therapy Facility for Cancer Treatment with Ion Beams,” submitted in 1998.
Available: https://www-alt.gsi.de/documents/DOC-2004-Feb-120-1.pdf.

[4] Summary report of the Joint DOE-NCI Workshop on Ion Beam Therapy, Bethesda, MD, USA (2013).
Available: http://science.energy.gov/~/media/hep/pdf/accelerator-rd-stewardship/Workshop_on_Ion_Beam_Therapy_Report_Final_R1.pdf.

[5] J. Kempe, I. Gudowska, and A. Brahme. "Depth absorbed dose and LET distributions of therapeutic H1, He4, Li7, and C12 beams." *Medical physics*, 34, 183 (2007).

[6] I. Pshenichnov, I. Mishustin and W. Greiner, "Comparative Study on Depth-Dose Distributions for Beams of Light and Heavy Nuclei in Tissue-like Media." *Nucl. Instr. Meth. Phys. Res. B*, 266, 1094 (2008).

[7] I. Kantemiris, *et al*., "Dose and dose averaged LET comparison of ^{1}H, ^{4}He, ^{6}Li, ^{8}Be, ^{10}B, ^{12}C, ^{14}N, and ^{16}O ion beams forming a spread-out Bragg peak." *Medical Physics*, 38, 6585 (2011).

[8] R. Grün, *et al*., "Assessment of potential advantages of relevant ions for particle therapy: A model based study." *Medical physics*, 42, 1037 (2015).

[9] J. A. Simpson, "Introduction to the Galactic Cosmic Radiation." *Composition and Origin of Cosmic Rays*, Dorcht, Nehterlands, Reidel Publishing, (1983).

[10] L. Heilbronn *et al*., "Neutron fluences and doses behind shielded environments in space." *2014 IEEE Aerospace Conference*, Big Sky, MT, USA, (2014).

[11] T. Sato *et al*., “Particle and Heavy Ion Transport Code System PHITS, Version 2.52.” *J. Nucl. Sci. Technol*., 50, 913 (2013).

[12] T. Böhlen *et al*., “The FLUKA Code: Developments and Challenges for High Energy and Medical Applications.” *Nucl. Data Sheets*, 120, 211 (2014).

[13] D. B. Pelowitz Ed., “MCNPX User’s Manual Version 2.7.0,” LA-CP-11-00438.” *Los Alamos National Laboratory report*, (2011).

[14] J. Allison *et al*., “Geant4 Developments and Applications.” *IEEE T. Nucl. Sci*., 53, 270 (2006).

[15] T. Nakamura and L. Heilbronn, “Handbook on Secondary Particle Production and Transport by High-Energy Heavy Ions.” Singapore, World Scientific Publishing Co. Pte. Ltd., (2006).

[16] T. Kurosawa *et al*., "A Spectral Measurements of Neutrons, Protons, Deuterons and Tritons Produced by 100 MeV/nucleon He bombardment." *Nucl. Instr. Meth. Phys. Res. A*, 430, 400 (1999).

[17] T. Kurosawa *et al*., “A. Fukumura and K. Murakami, "Neutrons Produced from Thick Targets Bombarded by High-Energy Helium and Carbon Ions." *Nuc. Sci. Eng*, 132, 30 (1999).

[18] L. Heilbronn *et al*., "Neutron Yields from 155 MeV/nucleon Carbon and Helium Stopping in Aluminum." *Nuc. Sci. Eng*., 132, 1 (1999).

[19] R. A. Cecil *et al*., "Neutron Angular and Energy Distribution from 710-MeV Alphas Stopping in Water, Carbon, Steel, and Lead, and 640-MeV alphas Stopping on Lead." *Phys. Rev. C*, 21, 2471 (1980).

[20] B. Braunn *et al*., "Nuclear reaction measurements of 95 MeV/u ^{12}C interactions on PMMA for hadrontherapy.” *Nucl. Instr. Meth. Phys. Res. B*, 269, 2676 (2011).

[21] K. Gunzert-Marx *et al*., "Secondary Beam Fragments Produced by 200 MeV/u ^{12}C Ions in Water and Their Dose Contributions in Carbon Ion Radiotherapy." *New J. Phys*., 10, 21 (2008).

[22] T. Armstrong *et al*., “SPAR, a FORTRAN Program for Computing Stopping Powers and Ranges for Muons, charged Pions, Protons and Heavy ions.” ORNL-4869, Oak Ridge National Laboratory, (1973). Available:http://www.iaea.org/inis/collection/NCLCollectionStore/_Public/05/096/5096094.pdf.

[23] A. Boudard *et al*., "New Potentialities of the Liege Intranuclear Cascade Model for Reactions Induced by Nucleons and Light Charged Particles.” *Phys. Rev. C*, 87, 014606 (2013).

[24] J. F. Ziegler, M. D. Ziegler and J. P. Biersack, "SRIM – The stopping and range of ions in matter (2010)." *Nucl. Instr. Meth. Phys. Res. B*, 268, 1818 (2010).

[25] M. J. Berger *et al*., "ESTAR, PSTAR, and ASTAR: Computer Programs for Calculating Stopping-Power and Range Tables for Electrons, Protons, and Helium Ions (version 1.2.3)." *National Institute of Standards and Technology*, Gaithersburg, MD, (2005).

[26] J. H. Heltsley *et al*., "Particle identification via pulse-shape discrimination with a charge-integrating ADC." *Nucl. Instr. Meth. Phys. Res. A*, 263, 441 (1988).

[27] D. Satoh *et al*., “SCINFUL-QMD: Monte Carlo based computer code to calculate response function and detection efficiency of a liquid organic scintillator for neutron energies up to 3 GeV.” *Japan Atomic Energy Agency*, 38, 38054863 (2006).

[28] D. Satoh, *et al*. "Measurement of Response Functions of a Liquid Organic Scintillator for Neutrons up to 800 MeV." *Journal of nuclear science and technology*, 43, 714 (2006).

[29] “Particle and Heavy Ion Transport Code System (PHITS),” Available: http://phits.jaea.go.jp/OvMapOfModels.html

[30] S. G. Mashnik and A. J. Sierk, “CEM03.03 User Manual.” *LANL Report LA-UR-12-01364*, Los Alamos, (2012).

[31] K. K. Gudima, S. G. Mashnik, and A. J. Sierk, “*Use Manual for the Code LAQGSM*.” LANL Report LA-UR-01-6804, Los Alamos, (2001).

[32] S. G. Mashnik and L. M. Kerby, “MCNP6 Fragmentation of Light Nuclei at Intermediate Energies.” *LANL Report LA-UR-14-22448*, Los Alamos, (2014).

[33] T. Kurosawa, *et al*., "Measurements of secondary neutrons produced from thick targets bombarded by high-energy helium and carbon ions." *Nuc. Sci. Eng.,* 132, 30 (1999).

[34] N. V. Mokhov and S. I. Striganov. "MARS15 overview." *AIP Conf. Proc.*, 896. No. FERMILAB-CONF-07-008-AD. (2007).

[35] L. W. Townsend, T. M. Miller, and T. A. Gabriel., "HETC radiation transport code development for cosmic ray shielding applications in space." *Radiat. Prot. Dosim.,* 116, 135 (2005).

[36] Y. Iwata *et al*., "Double-differential cross sections for the neutron production from heavy-ion reactions at energies E/A= 290–600 MeV." *Phys. Rev. C*, 64, 054609 (2001).

[37] H. Sato *et al*., "Measurements of double differential neutron production cross sections by 135 MeV/nucleon He, C, Ne and 95 MeV/nucleon Ar ions." *Phys. Rev. C*, 64, 034607 (2001).

[38] L. Heilbronn *et al*., "Secondary neutron-production cross sections from heavy-ion interactions between 230 and 600 MeV/nucleon." *Nuc. Sci. Eng*., 157, 142 (2007).

[39] D. Satoh *et al*., "Reevaluation of secondary neutron spectra from thick targets upon heavy-ion bombardment." *Nucl. Instr. Meth. Phys. Res. A*, 583, 507 (2007).

[40] “Status report on the Monte Carlo models actually available for hadron therapy calculations.” *Envision-WP6 Report n.1*, (2011). Available: https://cdsweb.cern.ch/record/1977918/files/ENVISION-MISC-2014-020.1.pdf.

[41] I. Remec, R. M. Ronningen, and L. Heilbronn. “Benchmarking of neutron production of heavy-ion transport codes.” No. INIS-US-13-ISRD-14-os4p-3. American Society for Testing and Materials-ASTM International, West Conshohocken, PA, 19428-2959 (United States); European Working Group on Reactor Dosimetry-EWGRD, SCK. CEN, Mol (Belgium), (2011).

[42] G. Bollen *et al*., “Final Report on Benchmarking Heavy Ion Transport Codes FLUKA, HETC-HEDS, MARS15, MCNPX, and PHITS.” DE-GF02-08ER41548 (2013).
Available: http://www.osti.gov/scitech/servlets/purl/1082753.

[43] S. G. Mashnik, “Validation and Verification of MCNP6 Against High-Energy Experimental Data and Calculations by other Codes. III. The MPI Testing Primer.” LANL Report LA-UR-13-26944, Los Alamos, (2013).

[44] Garzelli, M. V., et al. "A Monte Carlo approach to study neutron and fragment emission in heavy-ion reactions." *Adv. Space Res.,* 40, 1350 (2007).

[45] N. Nakao *et al*., "Measurements of response function of organic liquid scintillator for neutron energy range up to 135 MeV." *Nucl. Instr. Meth. Phys. Res. A,* 362, 454 (1995).

[46] A. Y. Konobeyev *et al*., "What Can We Expect from the Use of Nuclear Models Implemented in MCNPX at Projectile Energies Below 150 MeV? Detailed Comparison with Experimental Data." *J. Korean Phys. Soc*., 59, 927 (2011).

[47] S. Sharma (2015). “*VALIDATION OF SPALLATION MODELS*.” (Doctoral dissertation). Jagiellonian University, Poland.

[48] J.-C. David, "Spallation reactions. A successful interplay between modeling and applications." arXiv preprint arXiv:1505.03282 (2015).

APPENDIX

Appendix.1 Neutron double-differential cross sections

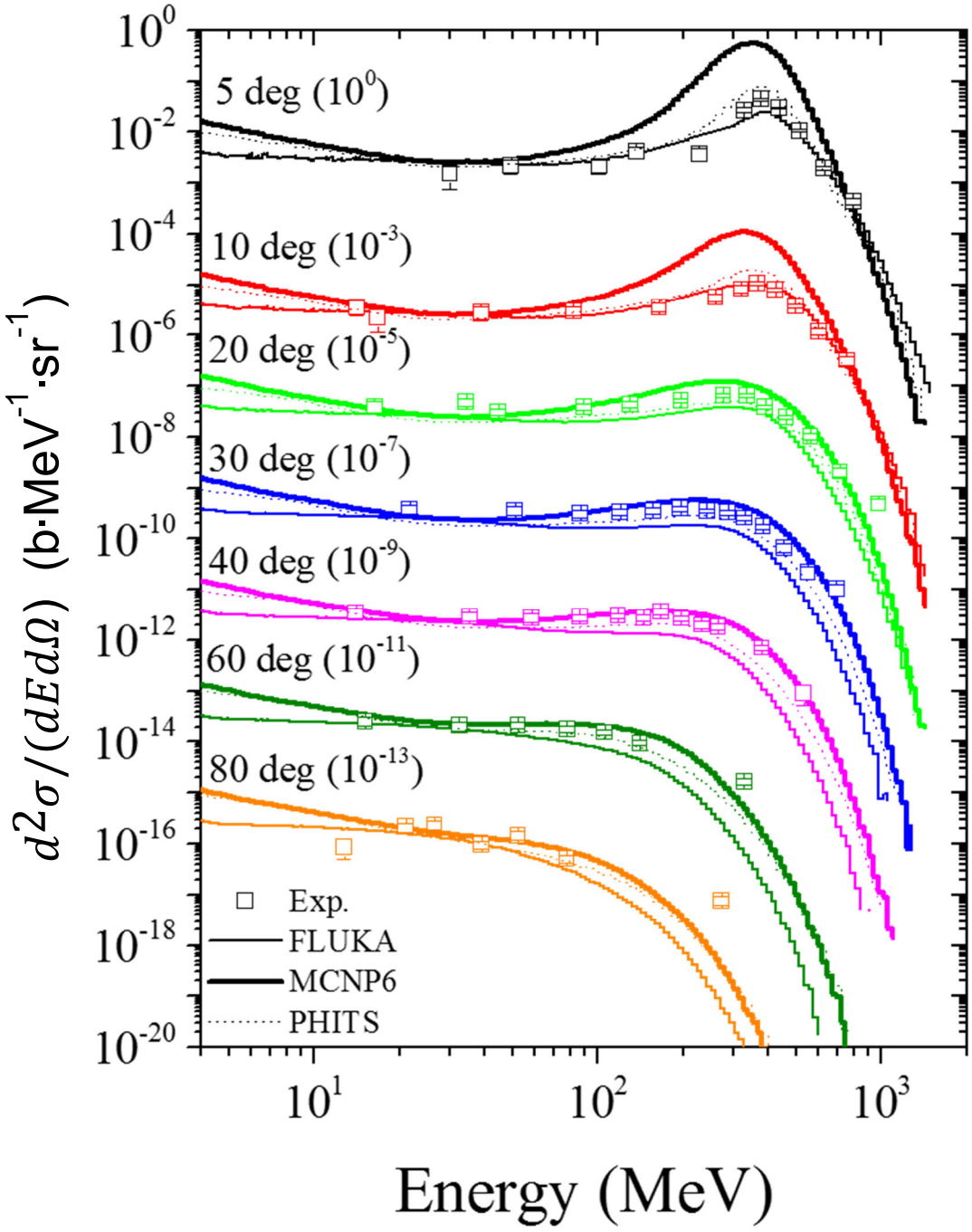

Figure 43. The neutron DDX with 400-MeV/nucleon ^{12}C + ^{nat}Li target.

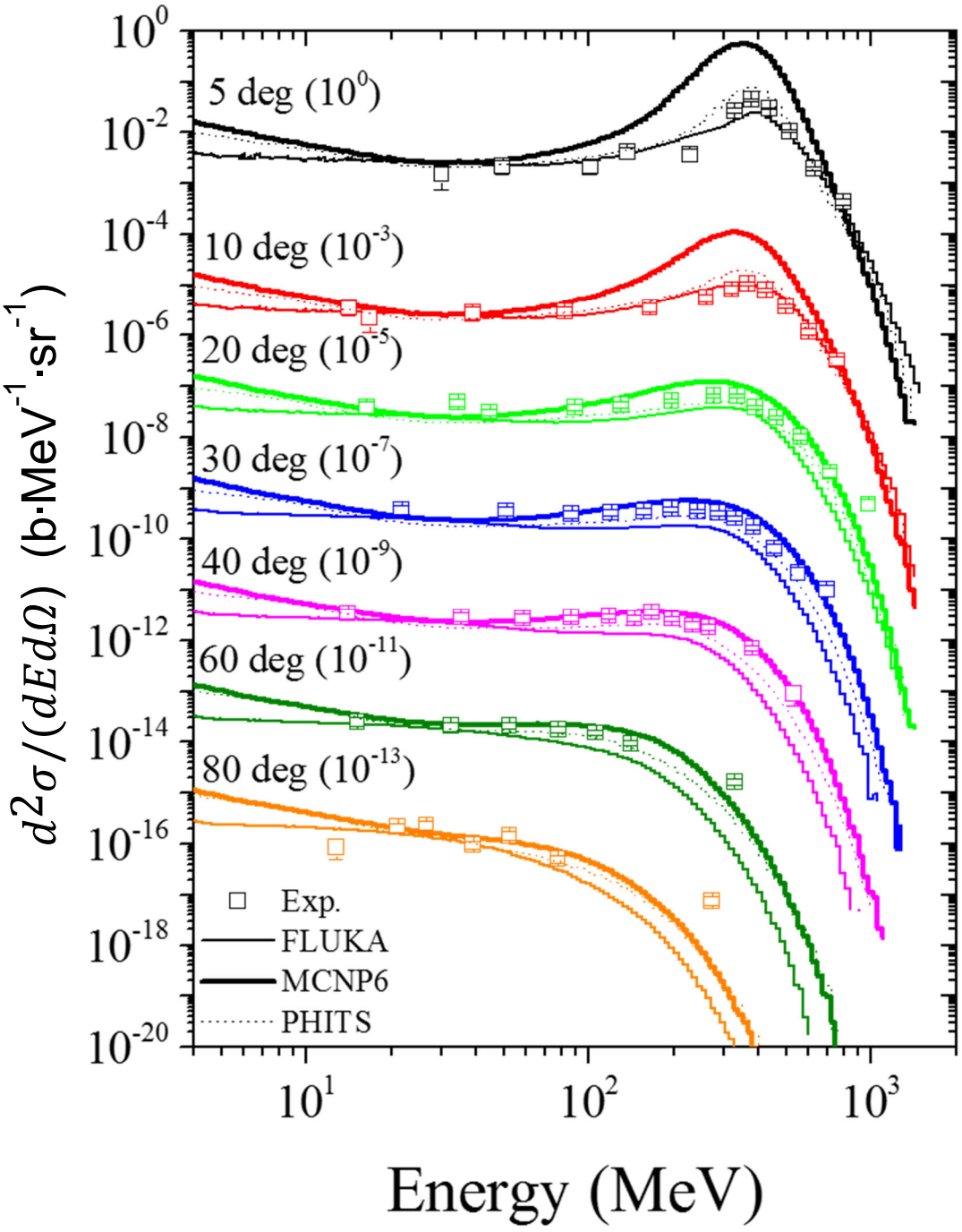

Figure 44. The neutron DDX with 400-MeV/nucleon ^{12}C + ^{nat}C target.

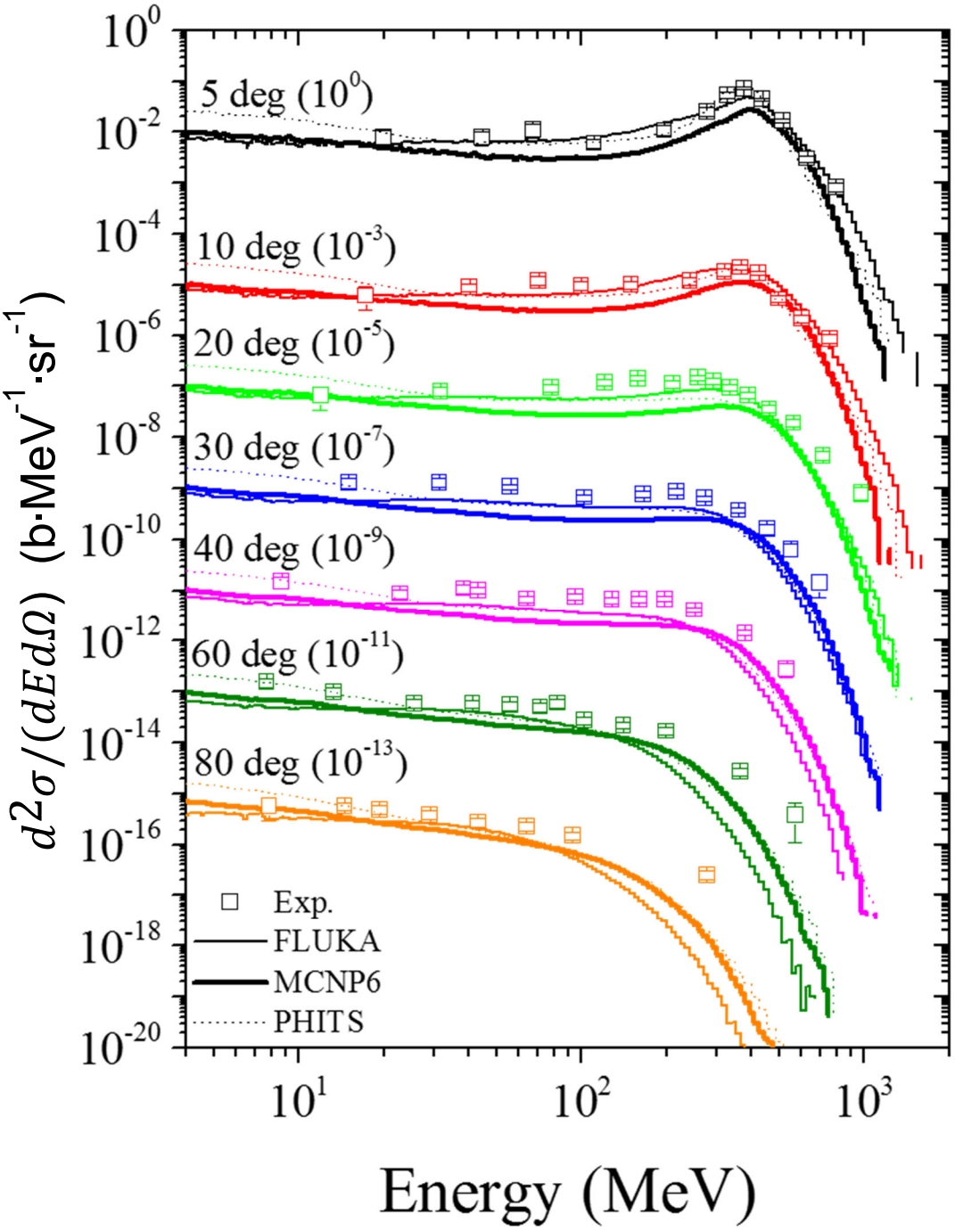

Figure 45. The neutron DDX with 400-MeV/nucleon ^{12}C + ^{nat}Al target.

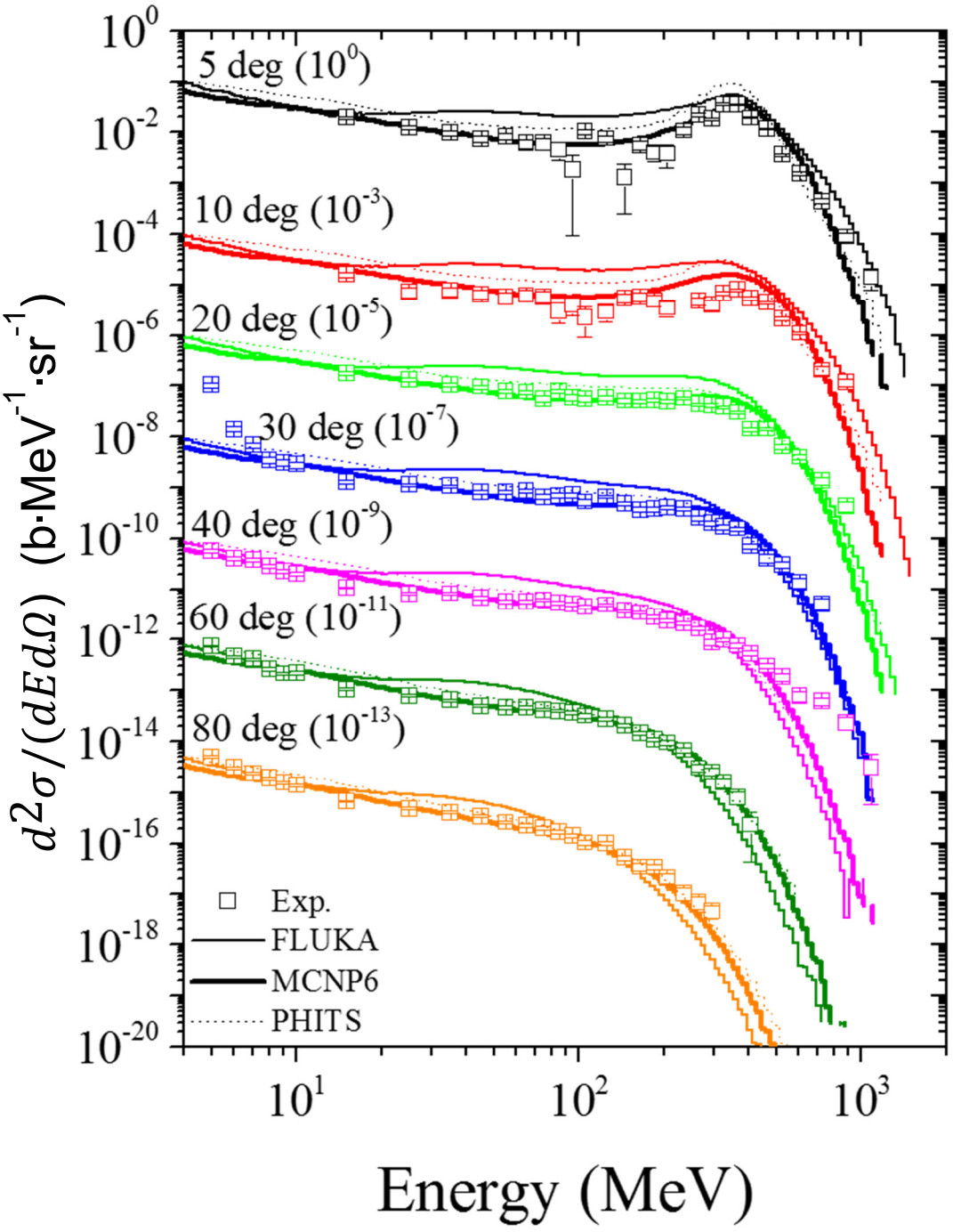

Figure 46. The neutron DDX with 400-MeV/nucleon ^{12}C + ^{nat}Cu target.

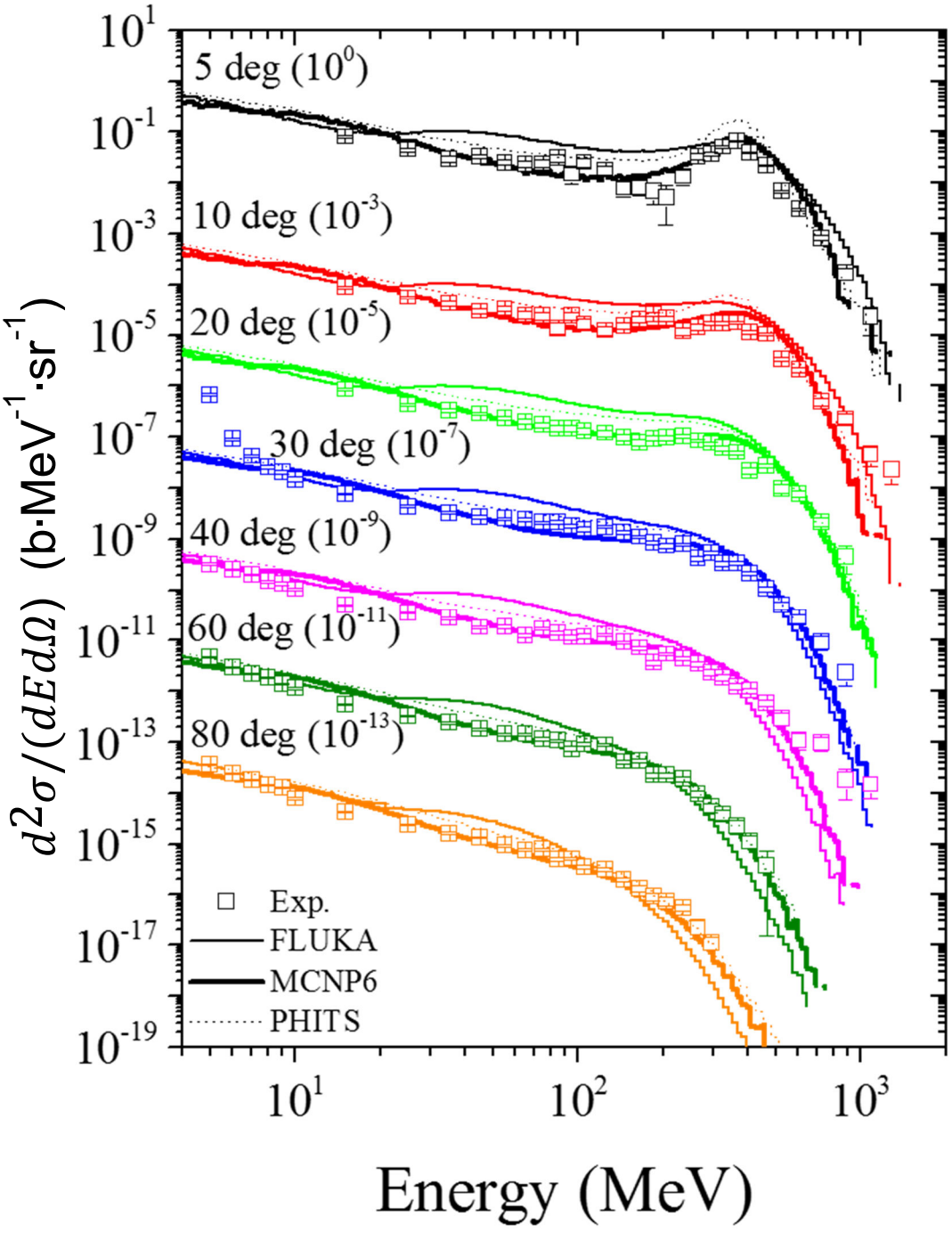

Figure 47. The neutron DDX with 400-MeV/nucleon ^{12}C + ^{nat}Pb target.

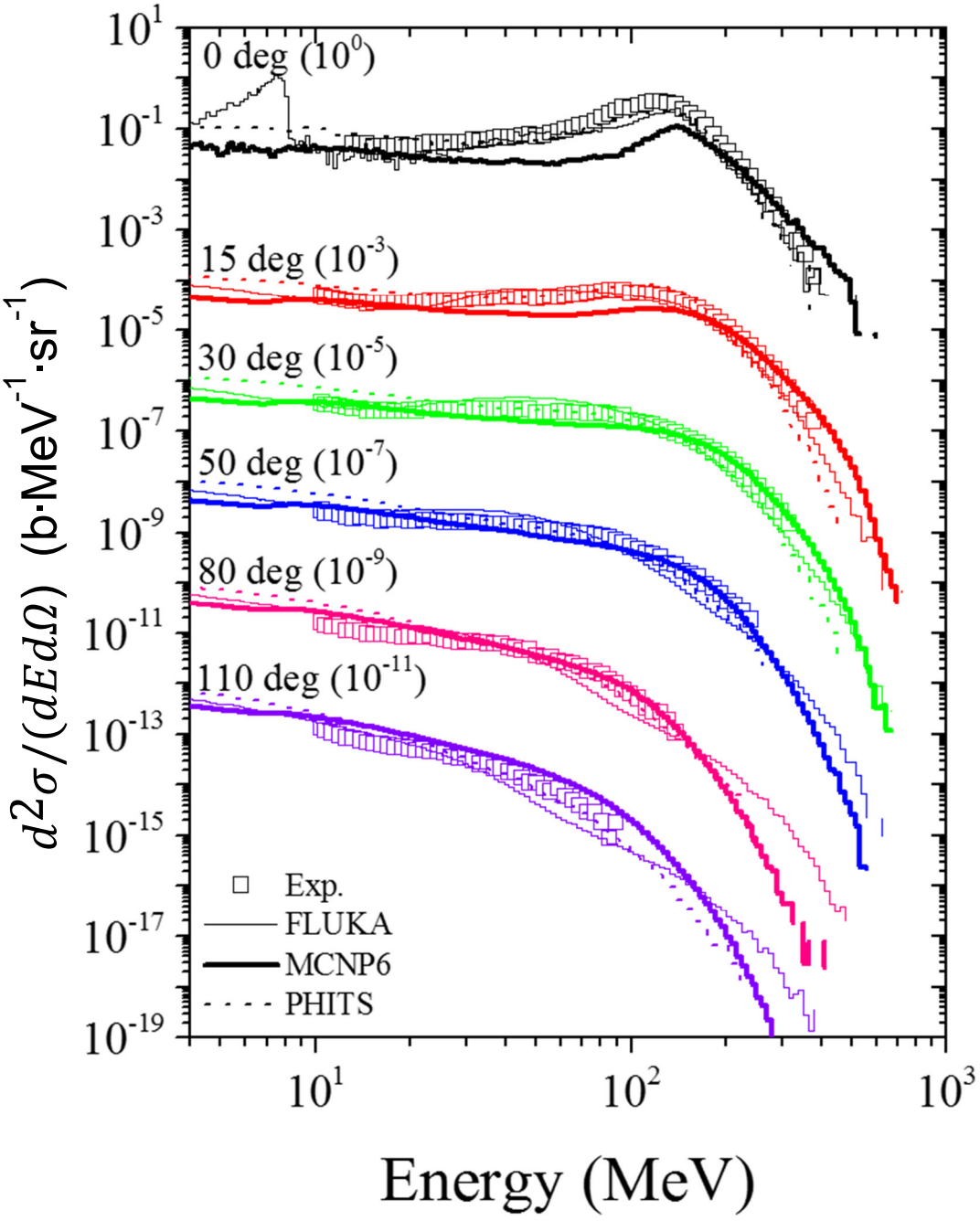

Figure 48. The neutron DDX with 135-MeV/nucleon ^{20}Ne + ^{nat}Cu target.

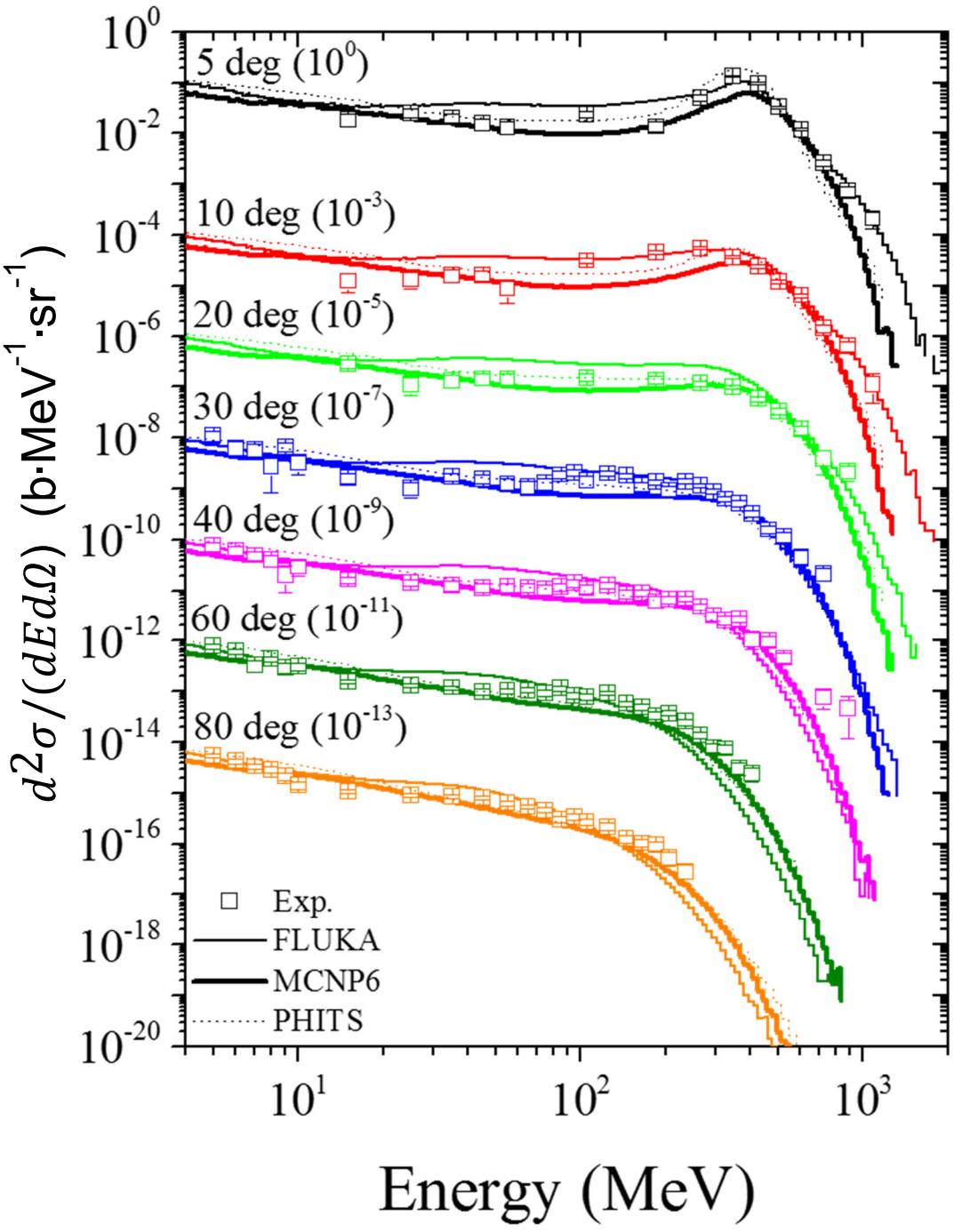

Figure 49. The neutron DDX with 400-MeV/nucleon ^{20}Ne + ^{nat}Cu target.

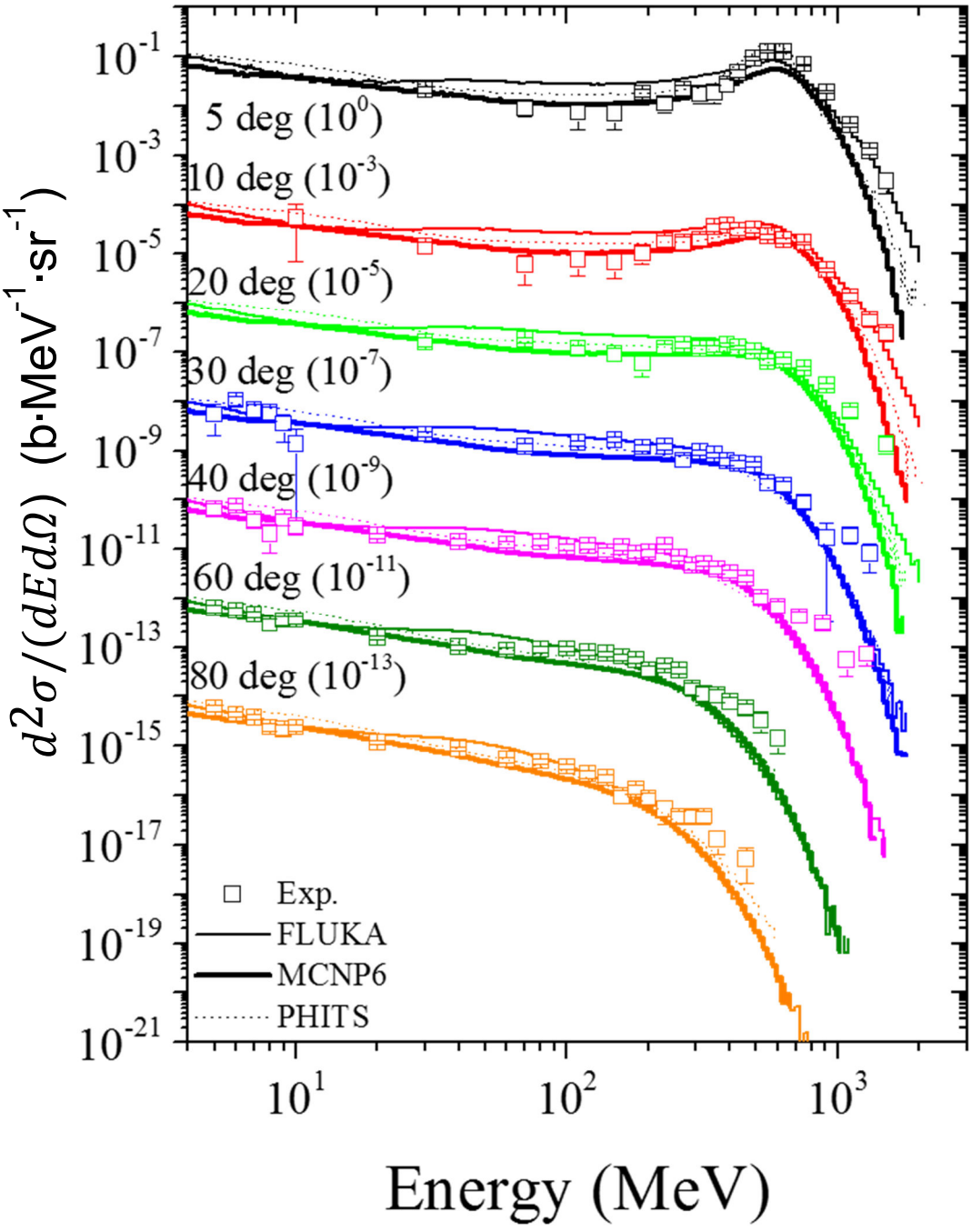

Figure 50. The neutron DDX with 600-MeV/nucleon ^{20}Ne + ^{nat}Cu target.

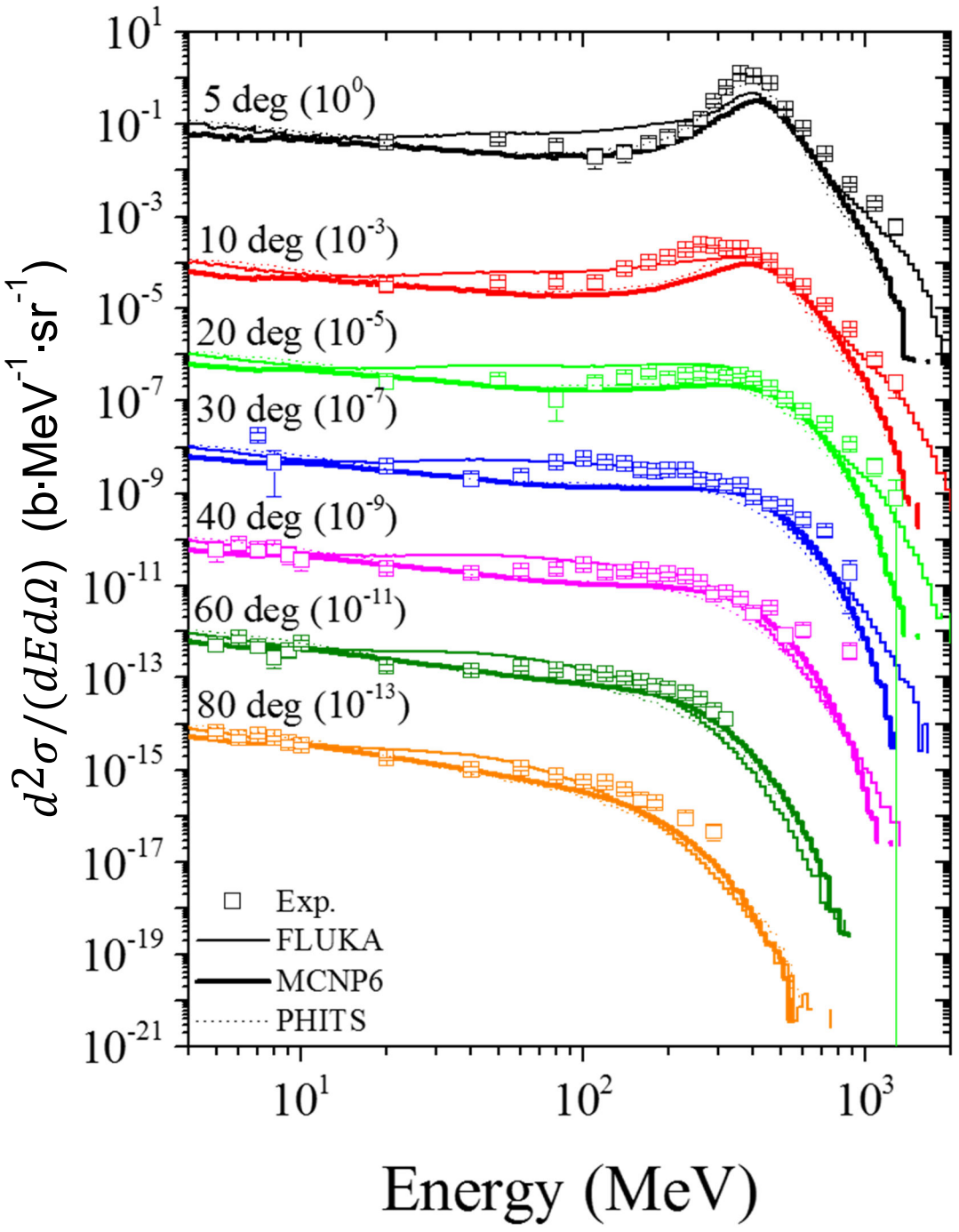

Figure 51. The neutron DDX with 400-MeV/nucleon ^{40}Ar + ^{nat}Cu target.

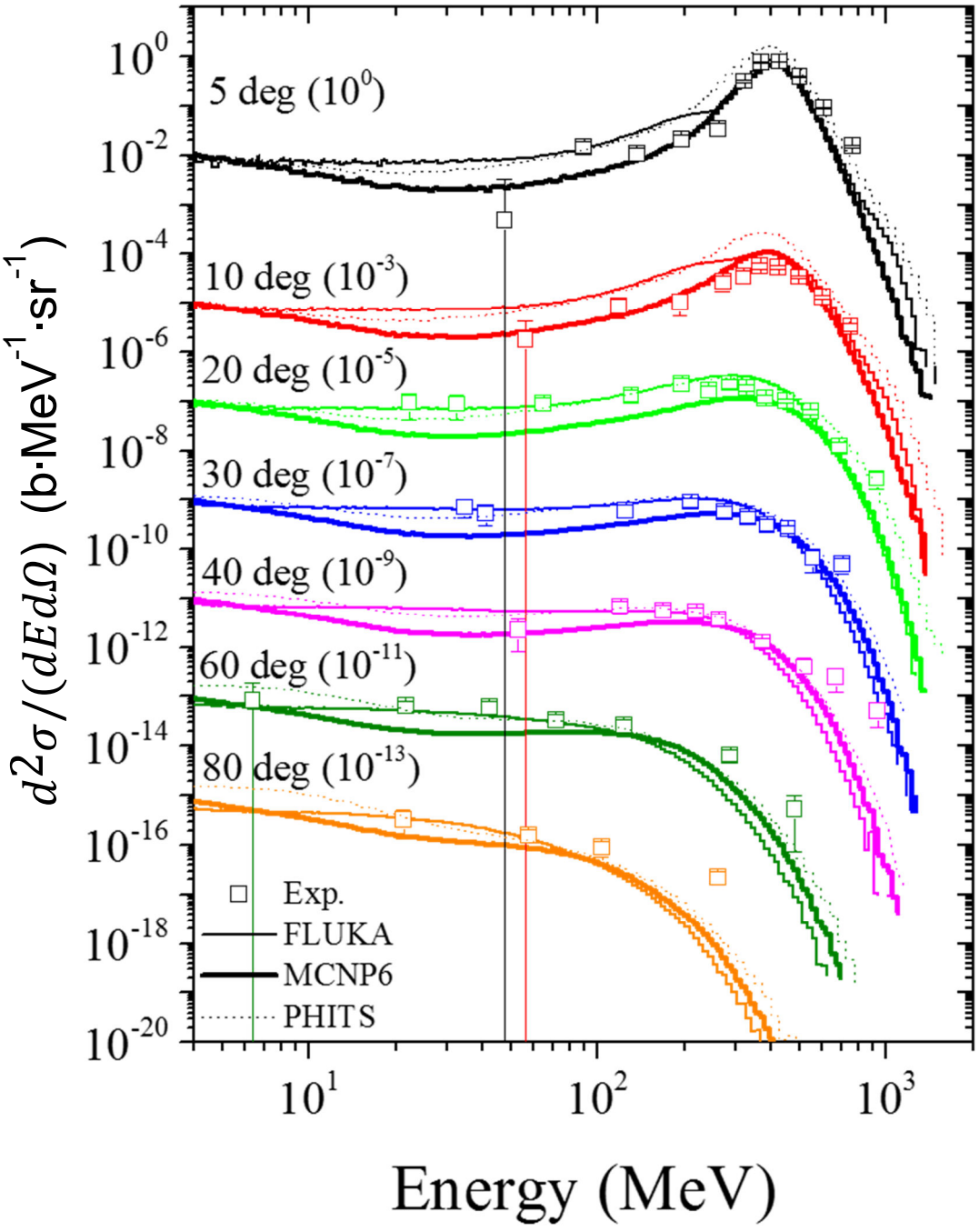

Figure 52. The neutron DDX with 400-MeV/nucleon ^{84}Kr + ^{nat}Li target.

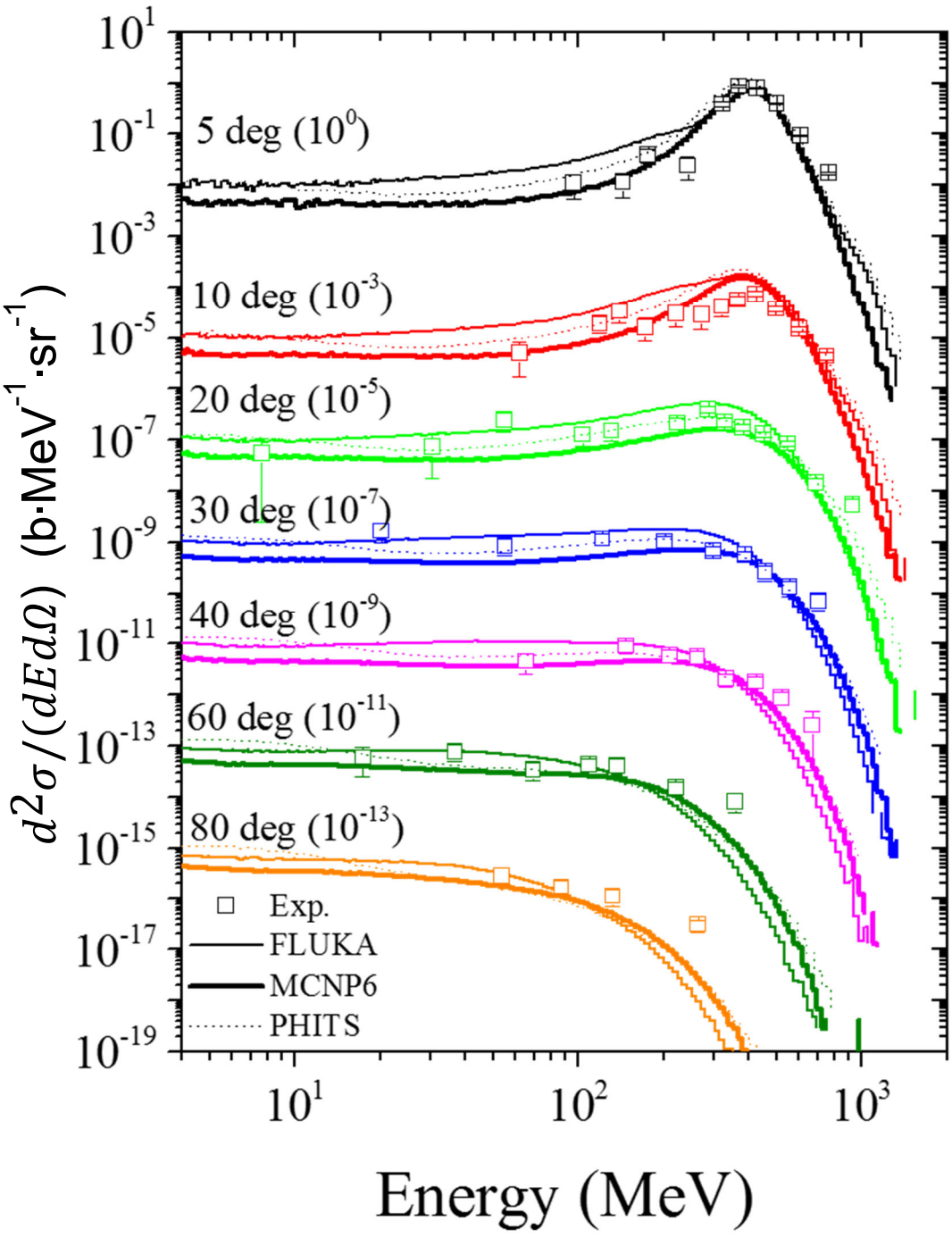

Figure 53. The neutron DDX with 400-MeV/nucleon ^{84}Kr + ^{nat}C target.

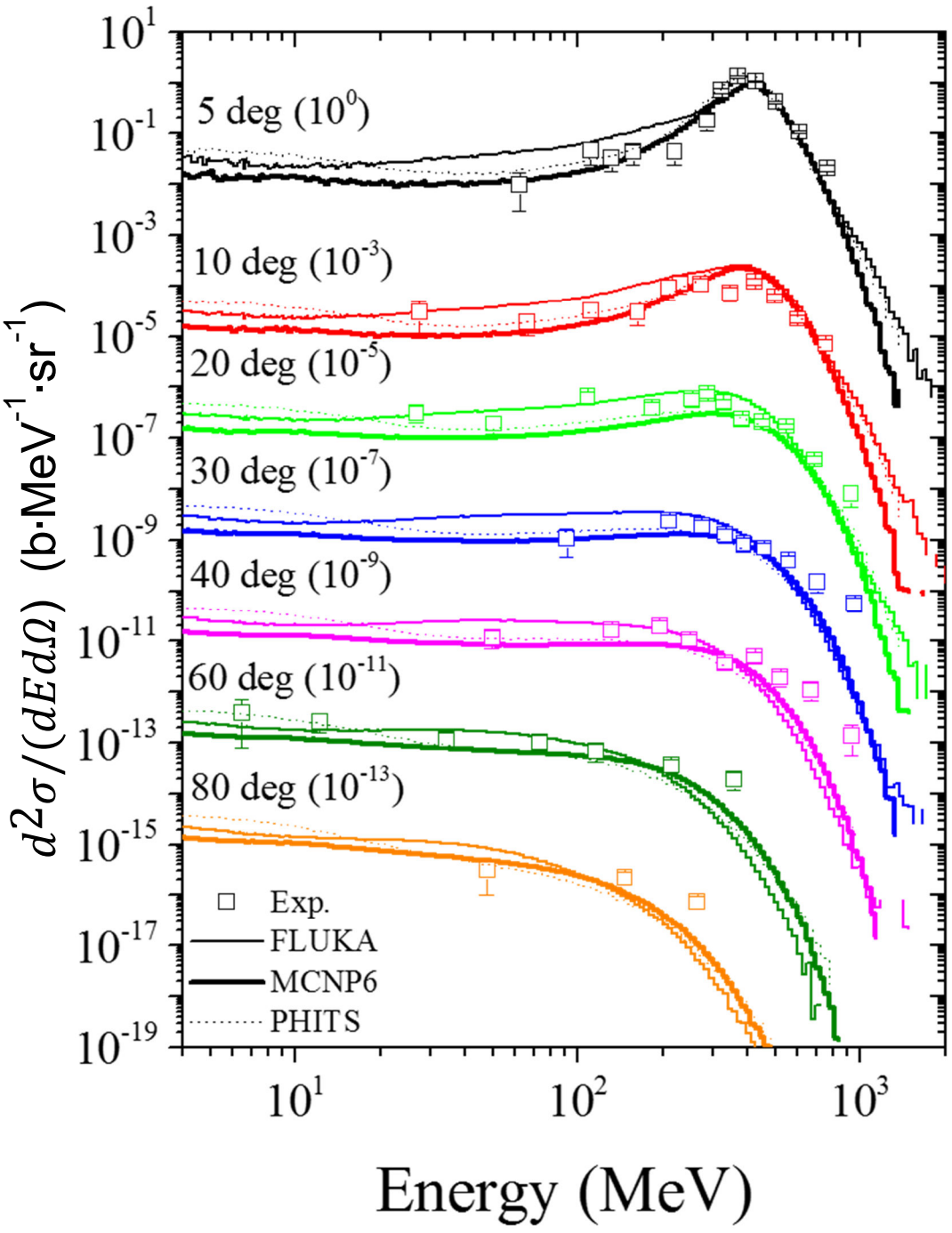

Figure 54. The neutron DDX with 400-MeV/nucleon ^{84}Kr + ^{nat}Al target.

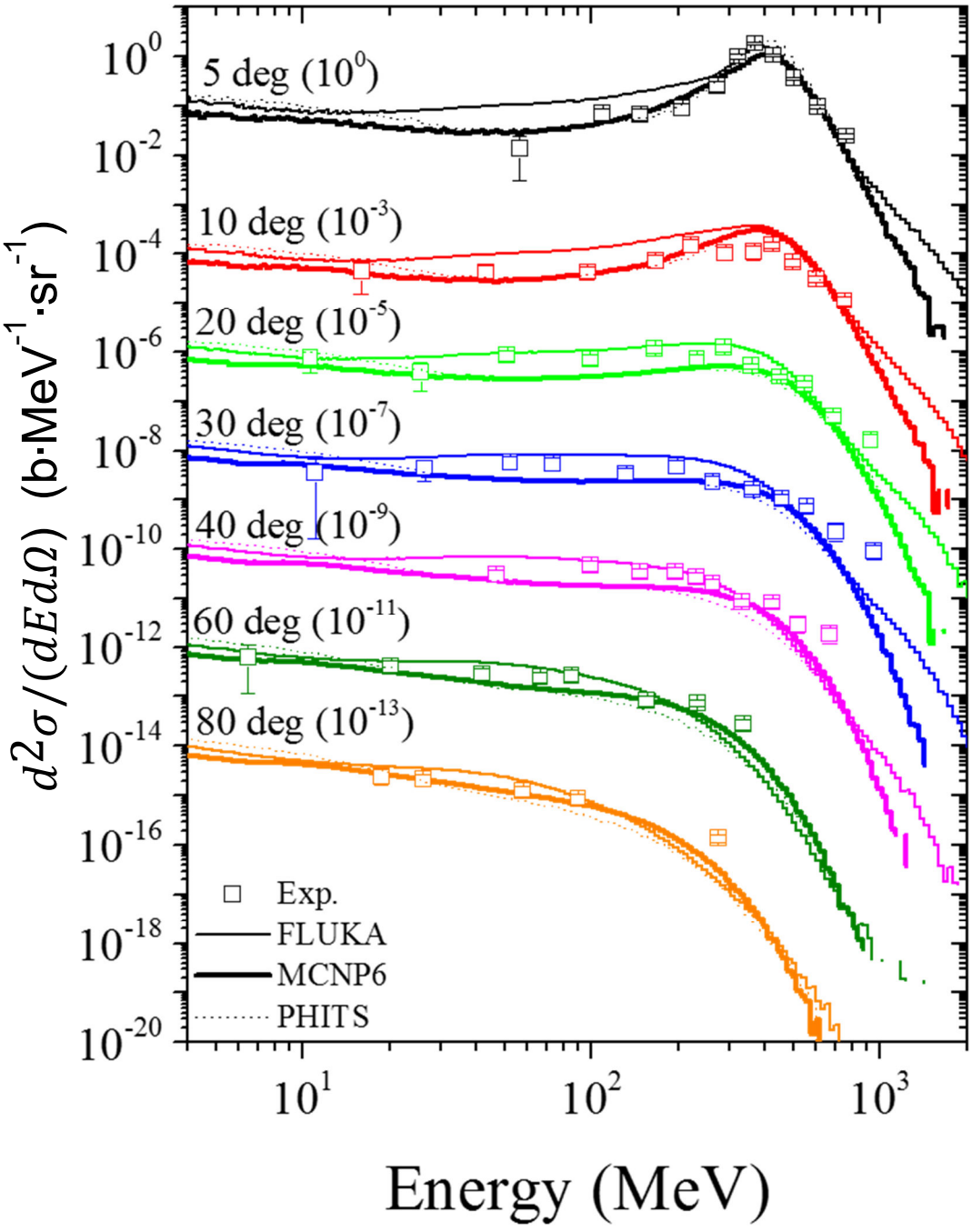

Figure 55. The neutron DDX with 400-MeV/nucleon ^{84}Kr + ^{nat}Cu target.

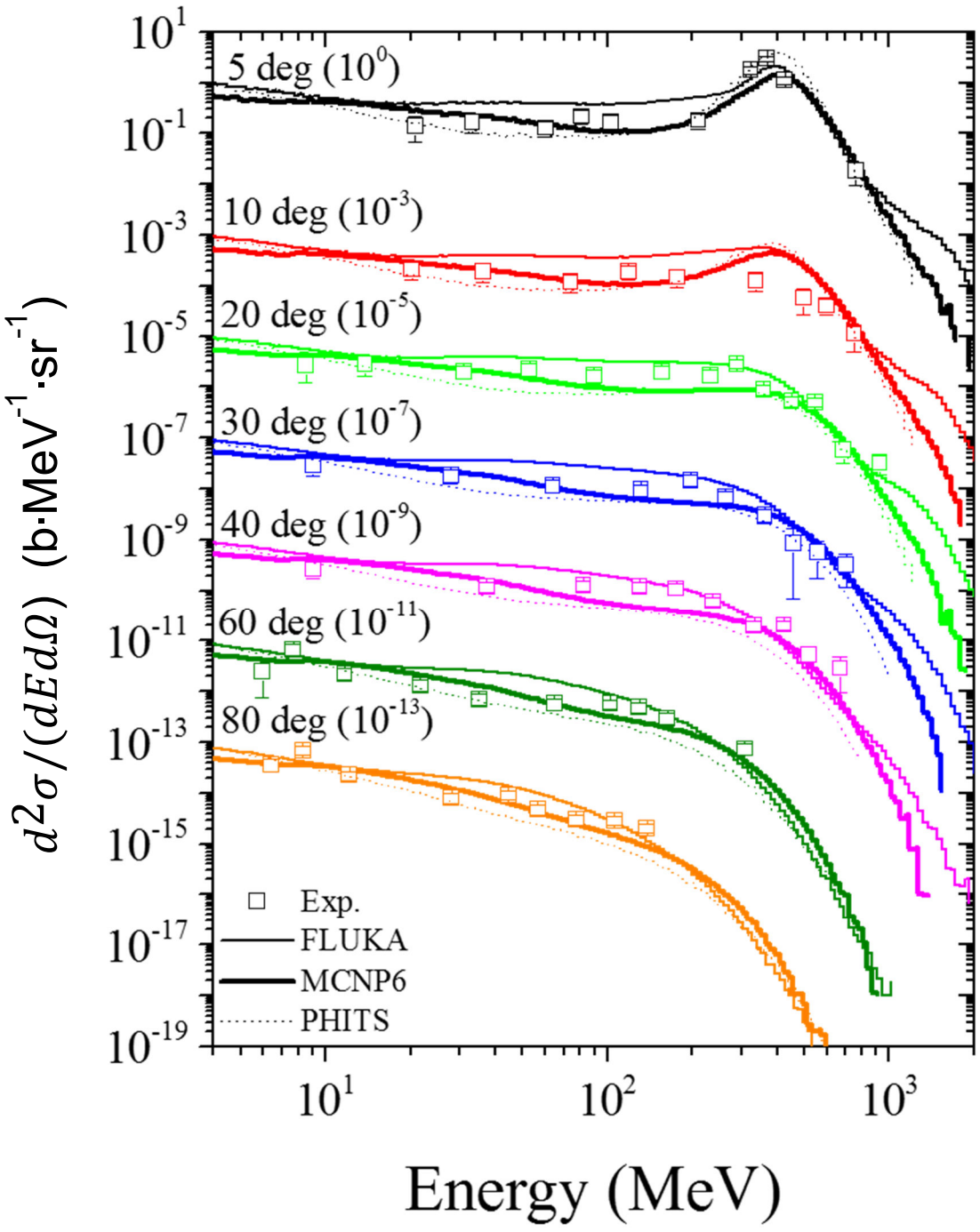

Figure 56. The neutron DDX with 400-MeV/nucleon ^{84}Kr + ^{nat}Pb target.

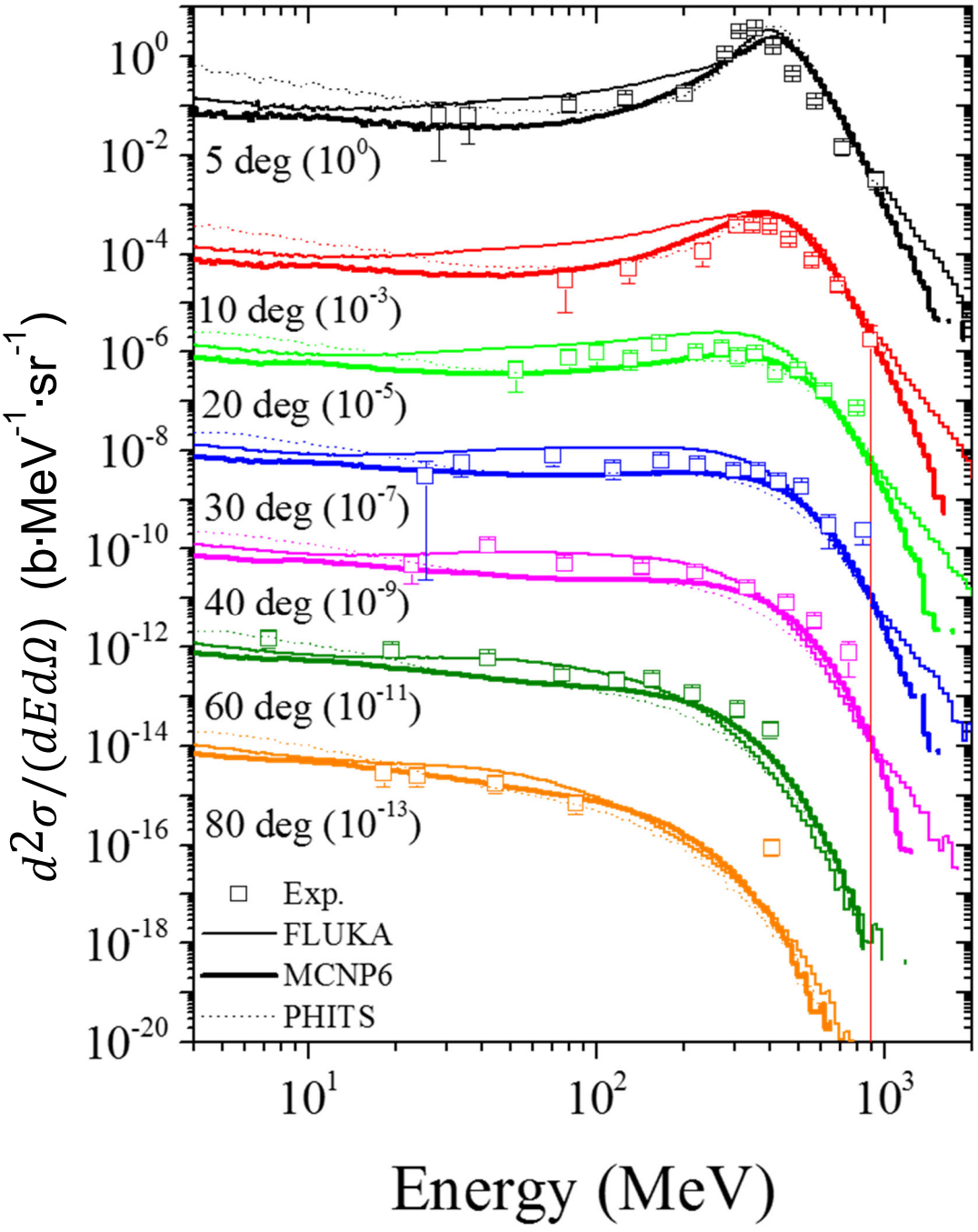

Figure 57. The neutron DDX with 400-MeV/nucleon ^{132}Xe + ^{nat}Cu target.

VITA

Pi-En Tsai received her M.S. degree in nuclear engineering in 2009 from National Tsing Hua University, Taiwan, and has been at the University of Tennessee since 2010. She conducts research on the measurement and Monte Carlo simulation of secondary neutrons from heavy ion interactions relevant to both shielding in space and heavy ion radiotherapy. She is also conducting research on methods for the calibration of liquid scintillator neutron detectors over a broad range of pulse heights.